



# Politecnico di Torino

Civil Engineering-Geotechnics  
A.a. 2023/2024  
Graduation period: October 2024

## Numerical study on the failure mechanisms of rock cliffs subjected to basal erosion

Relatori:

Prof. Monica Barbero  
Eng. Maria Lia Napoli

Candidato:

Su Hongyuan(s302312)

# Contents

Abstract.....	1
1. Introduction .....	2
2. Erosion of cliffs in coastal areas.....	3
3. The Study area .....	6
4. Numerical analyses of cliffs .....	9
4.1 Material of cliff .....	9
4.2 FEM analyses of cliffs.....	9
4.2.1 Homogeneous vertical cliff without joint .....	12
4.2.2 Homogeneous inclined cliff without joint .....	12
4.2.3 Homogeneous vertical cliff with joint.....	13
4.3 FDEM analyses of cliffs .....	14
4.3.1 Homogeneous vertical cliff without joint .....	14
4.3.2 Homogeneous vertical cliff with joint.....	18
5. Results.....	20
5.1 FEM analyses .....	20
5.1.1 Homogeneous vertical cliff without joint .....	20
5.1.2 Homogeneous inclined cliff without joint .....	34
5.1.3 Homogeneous vertical cliff with joint.....	36
5.2 FDEM Numerical analyses .....	42
5.2.1 Homogeneous vertical cliff without joint .....	42
5.2.2 Homogeneous vertical cliff with joint.....	47
6. Discussion .....	51
7. Conclusion .....	54
8. References .....	55
9. Appendices .....	57
9.1 Appendix A: Numerical Results of Homogeneous Vertical Cliffs Without Joint .....	57
9.1.1 A1 : Maximum shear strain of homogeneous vertical cliffs with notch depth of 5m. ....	57
9.2 Appendix B: Numerical Results of Homogeneous Inclination Cliffs without Joint. ....	60
9.2.1 B1 : Maximum shear strain of homogeneous inclination cliffs with notch depths of 3m, 5m, 7m, and 10m. ....	60

9.3 Appendix C: Numerical Results of Homogeneous Vertical Cliffs with joint.....	62
9.3.1 C1 : Maximum shear strain of homogeneous vertical cliffs with notch depth of 5m .	62
9.4 Appendix D: The modeling process in the Irazu software .....	74
9.4.1 Homogeneous vertical cliff without joint .....	74
9.4.2 Homogeneous cliff with joint .....	84

# List of Tables

Table 1 Physical mechanical parameters of the lithotypes. From Calista et al. (2019). .....	9
Table 2 Critical SRF of homogeneous cliffs with 16 different heights at a notch depth of 5 m. ...	20
Table 3 Results of the maximum shear strain at high cliffs ( $H_c \geq 10$ m) with 5 m notch depth..	23
Table 4 Results of the maximum shear strain at low cliffs ( $H_c < 10$ meters) with 5 meters notch depth.....	25
Table 5 Critical SRF of homogeneous cliffs with 15 different heights at a notch depth of 3 meters. ....	27
Table 6 Comparison the Inkate's (2023) results with this study's results of maximum shear strain band for high cliffs with a notch depth of 3 meters.....	29
Table 7 Comparison the Inkate's (2023) results with this study's results of maximum shear strain band for low cliffs with a notch depth of 3 meters.....	30
Table 8 Slenderness and critical SRF of homogeneous cliffs with notch depth of 10 meters, 7 meters, 3 meters (from Povanat Inkate 2023) and 5 meters (This study) .....	33
Table 9 Comparison of critical SRF for vertical cliffs and inclination cliffs.....	34
Table 10 Comparison of the maximum shear strain band for vertical and inclined cliffs. ....	35
Table 11 The strength parameters of joint .....	36
Table 12 The strength parameters of the joint considering a joint persistence of 62.40% for the length of 23.75 meters. ....	36
Table 13 Influence of horizontal location of joints with the joint length of 23.75 meters and notch depth of 7 meters.....	37
Table 14 Results of parametric analysis of 25 m high homogeneous cliff with 18.75 m long joint, and a notch depth of 7 m.....	38
Table 15 The strength parameters of the joint considering joint persistence =63.32% for the length of 18.75 meters. ....	38
Table 16 Influence of horizontal location of joints with the joint length of 18.75 meters and notch depth of 7 meters.....	39
Table 17 Material properties and parameters required by Irazu software. ....	42
Table 18 The 13.75 meters joint properties and parameters required by Irazu software. ....	47
Table 19 The 23.75 meters joint properties and parameters required by Irazu software. ....	49

# List of Figures

Figure 1 Three major morphologies on rocky coasts: (a) Type-A shore platform (sloping type), (b) Type-B shore platform (horizontal or sub-horizontal type) and (c) plunging cliff. From Sunamura (2015). .....	3
Figure 2 Basic notch shapes. HT: high tide, LT: low tide, R point: retreating point, R zone: retreating zone. From Wziatek et al. (2011). ....	4
Figure 3 (a) The main physiographic domains of the Abruzzo region (according to the morphotectonic landscape classification, D'Alessandro et al. 2003). The black polygon indicates the study area. (b) The lithological scheme of the study area and location of the cliff sites (modified from Miccadei et al. 2019). ....	6
Figure 4 (a) Location of the studied areas; (b) schematic geomorphological map of the Ortona coastal sector (modified from Miccadei et al. 2019). Legend: PF: Punta Ferruccio cliff. ....	7
Figure 5 The Punta Ferruccio cliff. Aerial images from (a) 2004, (b) 2006, and (c) 2014; cliff image and The Punta Ferruccio cliff. Aerial images from (a) 2004, (b) 2006, and (c) 2014; cliff image and geomorphological sections from (d) 2004, (e) 2005, and (f) 2014 outlining the rockfall that occurred in 2004–2005 (L1) and the topple that occurred in 2014 (L2), controlled by the main joints and notch. Legend: 1. Gravel, 2. Sand, 3. Landslide deposits, 4. Conglomerate, 5. Sandy Clay, 6. Sandstone, 7. Clay, 8. Sand, 9. Main joint, and 10. Landslide scarp. L1, 2004–2005 rockfall; and L2, 2014 topple. From Calista et al. (2019). ....	8
Figure 6 Geometry of the homogeneous vertical cliff without joint. ....	10
Figure 7 Simplified numerical model of the Punta Ferruccio in RS2 ....	11
Figure 8 The model of a homogeneous inclined cliff without a joint. ....	12
Figure 9 Coordinates defining the homogeneous vertical cliff without joint and excavation stages geometry. ....	15
Figure 10 Final finite element mesh generated for the homogeneous vertical cliff without joint and excavation stages model. ....	15
Figure 11 Coordinates defining the homogeneous vertical cliff without joint, with 2-notch excavation stages geometry. ....	16
Figure 12 Final finite element mesh generated for the homogeneous vertical cliff without joint, with 2-notch excavation stages model. ....	16
Figure 13 Coordinates defining the homogeneous vertical cliff without joint, with 4-notch excavation stages geometry. ....	17
Figure 14 Final finite element mesh generated for the homogeneous vertical cliff without joint, with 4-notch excavation stages model. ....	17
Figure 15 Coordinates defining the homogeneous vertical cliff without joint, with 10 vertical and 4-notch excavation stages geometry. ....	18
Figure 16 Final finite element mesh generated for the homogeneous vertical cliff without joint, with 10 vertical and 4-notch excavation stages model. ....	18
Figure 17 Final geometry of the cliff model with a 13.75m joint. ....	19
Figure 18 Final geometry of the cliff model with a 23.75m joint. ....	19
Figure 19 Correlation between the critical SRF and cliff height of homogeneous cliffs with a notch depth of 5 m. ....	21

Figure 20 Failure mechanisms for high cliffs ( $H_c \geq 10$ m) with notch depth of 5 m: Maximum shear strain in a homogeneous cliff with a height of 22.5 m. ....	22
Figure 21 Correlation between the inclination of the maximum shear strain band and cliff height of the high cliffs ( $H_c \geq 10$ m) with 5 m notch depth. ....	23
Figure 22 Failure mechanisms for low cliffs ( $H_c < 10$ meters) with notch depth of 5 meters: Maximum shear strain in a homogeneous cliff with height 5 meters. ....	24
Figure 23 Correlation between L1 and cliff heights of low cliffs with 5 meters notch depth. ....	25
Figure 24 Correlation between L2 and cliff heights of low cliffs with 5 meters notch depth. ....	26
Figure 25 Correlation between L3 and cliff heights of low cliffs with 5 meters notch depth. ....	26
Figure 26 Correlation between m, n, and cliff heights of low cliffs with 5 meters notch depth...	27
Figure 27 Comparison of the Inkate's (2023) results with this study's results: correlation between the critical SRF and cliff height of homogeneous cliffs with a notch depth of 3 meters. ....	28
Figure 28 Comparison of the Inkate (2023) results with this study's results of correlation between the inclination of maximum shear strain band and cliff with notch depth of 3 meters: High cliffs. ....	29
Figure 29 Comparison the Inkate's (2023) results with this study's results of correlation between L1 and cliff heights of low cliffs with 3 meters notch depth. ....	30
Figure 30 Comparison the Inkate's (2023) results with this study's results of correlation between L2 and cliff heights of low cliffs with 3 meters notch depth. ....	31
Figure 31 Comparison the Inkate's (2023) results with this study's results of correlation between L3 and cliff heights of low cliffs with 3 meters notch depth. ....	31
Figure 32 Comparison the Inkate's (2023) results with this study's results of correlation between m and cliff heights of low cliffs with 3 meters notch depth. ....	32
Figure 33 Comparison of Inkate's (2023) results with this study's correlation between n and cliff heights of low cliffs with 3 meters notch depth. ....	32
Figure 34 Correlation between critical SRF and slenderness ratio of cliffs with notch depth of 10 meters, 7 meters, 5 meters, and 3 meters. ....	33
Figure 35 Correlation between critical SRF and notch depth for vertical and inclined cliffs. ....	34
Figure 36 Correlation between Inclination of the shear band and notch depth for vertical and inclination cliffs. ....	35
Figure 37 Comparison the Inkate's (2023) results with this study's results of the influence of horizontal joint location on the cliff stability ( $L_{\text{joint}}=23.75$ meters) and notch depth of 7 meters.....	37
Figure 38 In the background: the cliff model with a notch depth of 7 meters without joint (SRF 2.02), and superimpose the joint at different horizontal locations. ....	40
Figure 39 The influence of horizontal joint location on the cliff stability ( $L_{\text{joint}}=18.75$ meters) and notch depth of 7 meters. ....	40
Figure 40 Simulated evolution of vertical stress contour and fracture pattern after (a) 0-time step, (b) 970,000-time step, (c) 1,000,000-time step, and (d) 1,150,000-time step. ....	42
Figure 41 Simulated evolution of vertical stress contour and fracture pattern after (a) 0-time step, (b) 250,000-time step, (c) 500,000-time step, (d) 1,060,000-time step, (e) 1,100,000-time step, and (f) 1,250,000-time step. ....	43

Figure 42 Simulated evolution of vertical stress contour and fracture pattern after (a) 0-time step, (b) 250,000-time step, (c) 500,000-time step, (d) 750,000-time step, (e) 1,000,000-time step, (f) 1,640,000-time step, (g) 1,700,000-time step, and (h) 2,000,000-time step. ....	45
Figure 43 Simulated evolution of vertical stress contour and fracture pattern after (a) 0-time step, (b) 520,000-time step, (c) 600,000-time step, (d) 850,000-time step, (e) 1,100,000-time step, (f) 1,350,000-time step, (g) 1,900,000-time step, (h) 2,010,000-time step, and (i) 2,200,000-time step. .	46
Figure 44 The results of the homogeneous vertical cliff without joint (a) Irazu (b) RS2, from Inkate 2023.....	47
Figure 45 Simulated evolution of vertical stress contour and fracture pattern after (a) 1,000-time step, (b) 5,000-time step, (c) 54,000-time step, and (d) 115,000-time step. ....	48
Figure 46 Simulated evolution of vertical stress contour and fracture pattern after (a) 0-time step, (b) 4,000-time step, (c) 20,000-time step, and (d) 60,000-time step. ....	49
Figure 47 The results of the homogeneous vertical cliff with 13.75 meters joint (a) Irazu (b) RS2, from Inkate 2023; The results of the homogeneous vertical cliff with 23.75 meters joint (c) Irazu (d) RS2, from Inkate 2023. ....	50
Figure 48 Maximum shear strain and distribution of yielded stresses of homogeneous vertical cliffs with 5 meters notch depth – Cliff height of 25 meters. ....	57
Figure 49 Maximum shear strain and distribution of yielded stresses of homogeneous vertical cliffs with 5 meters notch depth – Cliff height of 20 meters. ....	57
Figure 50 Maximum shear strain and distribution of yielded stresses of homogeneous vertical cliffs with 5 meters notch depth – Cliff height of 15 meters. ....	58
Figure 51 Maximum shear strain and distribution of yielded stresses of homogeneous vertical cliffs with 5 meters notch depth – Cliff height of 10 meters. ....	58
Figure 52 Maximum shear strain and distribution of yielded stresses of homogeneous vertical cliffs with 5 meters notch depth – Cliff height of 8.5 meters. ....	58
Figure 53 Maximum shear strain and distribution of yielded stresses of homogeneous vertical cliffs with 5 meters notch depth – Cliff height of 7.5 meters. ....	59
Figure 54 Maximum shear strain and distribution of yielded stresses of homogeneous vertical cliffs with 5 meters notch depth – Cliff height of 5 meters. ....	59
Figure 55 Maximum shear strain and distribution of yielded stresses of homogeneous vertical cliffs with 5 meters notch depth – Cliff height of 3 meters. ....	59
Figure 56 Maximum shear strain and distribution of yielded stresses of homogeneous inclination cliffs with 3 meters notch depth – Cliff height of 25 meters. ....	60
Figure 57 Maximum shear strain and distribution of yielded stresses of homogeneous inclination cliffs with 5 meters notch depth – Cliff height of 25 meters. ....	60
Figure 58 Maximum shear strain and distribution of yielded stresses of homogeneous inclination cliffs with 7 meters notch depth – Cliff height of 25 meters. ....	61
Figure 59 Maximum shear strain and distribution of yielded stresses of homogeneous inclination cliffs with 10 meters notch depth – Cliff height of 25 meters. ....	61
Figure 60 The joints 18.75 meters deep are located at varying horizontal distances from the cliff edge. The height of the cliff is 25 meters and the depth of the notch is 7 meters: a1-b1) maximum shear strain contours of the horizontal distance for the vertical joint at a distance d=4 meters from the	

cliff face are at SRF 2.02, and 2.03 respectively; c1-d1) distribution of yielded elements for the vertical joint at a distance  $d=4$  meters from the cliff face are at SRF 2.02, and 2.03. .... 62

Figure 61 The joints 18.75 meters deep are located at varying horizontal distances from the cliff edge. The height of the cliff is 25 meters and the depth of the notch is 7 meters: a2-b2) maximum shear strain contours of the horizontal distance for the vertical joint at a distance  $d=5$  meters from the cliff face are at SRF 1.95, and 1.96 respectively; c2-d2) distribution of yielded elements for the vertical joint at a distance  $d=5$  meters from the cliff face are at SRF 1.95, and 1.96. .... 63

Figure 62 The joints 18.75 meters deep are located at varying horizontal distances from the cliff edge. The height of the cliff is 25 meters and the depth of the notch is 7 meters: a3-b3) maximum shear strain contours of the horizontal distance for the vertical joint at a distance  $d=6$  meters from the cliff face are at SRF 1.36, and 1.75 respectively; c3-d3) distribution of yielded elements for the vertical joint at a distance  $d=6$  meters from the cliff face are at SRF 1.36, and 1.75. .... 64

Figure 63 The joints 18.75 meters deep are located at varying horizontal distances from the cliff edge. The height of the cliff is 25 meters and the depth of the notch is 7 meters: a4-b4) maximum shear strain contours of the horizontal distance for the vertical joint at a distance  $d=7$  meters from the cliff face are at SRF 1.01, and 1.75 respectively; c4-d4) distribution of yielded elements for the vertical joint at a distance  $d=7$  meters from the cliff face are at SRF 1.01, and 1.75. .... 65

Figure 64 The joints 18.75 meters deep are located at varying horizontal distances from the cliff edge. The height of the cliff is 25 meters and the depth of the notch is 7 meters: a5-b5) maximum shear strain contours of the horizontal distance for the vertical joint at a distance  $d= 8$  meters from the cliff face are at SRF 1.55, and 1.56 respectively; c5-d5) distribution of yielded elements for the vertical joint at a distance  $d= 8$  meters from the cliff face are at SRF 1.55, and 1.56. .... 66

Figure 65 The joints 18.75 meters deep are located at varying horizontal distances from the cliff edge. The height of the cliff is 25 meters and the depth of the notch is 7 meters: a6-b6) maximum shear strain contours of the horizontal distance for the vertical joint at a distance  $d= 9$  meters from the cliff face are at SRF 1.82, and 1.83 respectively; c6-d6) distribution of yielded elements for the vertical joint at a distance  $d= 9$  meters from the cliff face are at SRF 1.82, and 1.83. .... 67

Figure 66 The joints 18.75 meters deep are located at varying horizontal distances from the cliff edge. The height of the cliff is 25 meters and the depth of the notch is 7 meters: a7-b7) maximum shear strain contours of the horizontal distance for the vertical joint at a distance  $d= 10$  meters from the cliff face are at SRF 1.91, and 1.92 respectively; c7-d7) distribution of yielded elements for the vertical joint at a distance  $d= 10$  meters from the cliff face are at SRF 1.91, and 1.92. .... 68

Figure 67 The joints 18.75 meters deep are located at varying horizontal distances from the cliff edge. The height of the cliff is 25 meters and the depth of the notch is 7 meters: a8-b8) maximum shear strain contours of the horizontal distance for the vertical joint at a distance  $d= 11$  meters from the cliff face are at SRF 0.01, and 0.99 respectively; c8-d8) distribution of yielded elements for the vertical joint at a distance  $d= 11$  meters from the cliff face are at SRF 0.01, and 0.99. .... 69

Figure 68 The joints 18.75 meters deep are located at varying horizontal distances from the cliff edge. The height of the cliff is 25 meters and the depth of the notch is 7 meters: a9-b9) maximum shear strain contours of the horizontal distance for the vertical joint at a distance  $d= 12$  meters from the cliff face are at SRF 0.61, and 0.62 respectively; c9-d9) distribution of yielded elements for the vertical joint at a distance  $d= 12$  meters from the cliff face are at SRF 0.61, and 0.62. .... 70



Figure 69 The joints 18.75 meters deep are located at varying horizontal distances from the cliff edge. The height of the cliff is 25 meters and the depth of the notch is 7 meters: a10-b10) maximum shear strain contours of the horizontal distance for the vertical joint at a distance  $d= 13$  meters from the cliff face are at SRF 0.85, and 0.86; c10-d10) distribution of yielded elements for the vertical joint at a distance  $d= 13$  meters from the cliff face are at SRF 0.85, and 0.86. .... 71

Figure 70 The joints 18.75 meters deep are located at varying horizontal distances from the cliff edge. The height of the cliff is 25 meters and the depth of the notch is 7 meters: a11-b11) maximum shear strain contours of the horizontal distance for the vertical joint at a distance  $d= 14$  meters from the cliff face are at SRF 1.04, and 1.05; c11-d11) distribution of yielded elements for the vertical joint at a distance  $d= 14$  meters from the cliff face are at SRF 1.04, and 1.05. .... 72

Figure 71 The joints 18.75 meters are located at varying horizontal distances from the cliff edge. The height of the cliff is 25 meters and the depth of the notch is 7 meters: a12-b12) maximum shear strain contours of the horizontal distance for the vertical joint at a distance  $d= 15$  meters from the cliff face are at SRF 1.11, and 1.12; c12-d12) distribution of yielded elements for the vertical joint at a distance  $d= 15$  meters from the cliff face are at SRF 1.11, and 1.12. .... 73

Figure 72 The joints 18.75 meters are located at varying horizontal distances from the cliff edge. The height of the cliff is 25 meters and the depth of the notch is 7 meters: a13-b13) maximum shear strain contours of the horizontal distance for the vertical joint at a distance  $d= 16$  meters from the cliff face are at SRF 1.30, and 1.31; c13-d13) distribution of yielded elements for the vertical joint at a distance  $d= 16$  meters from the cliff face are at SRF 1.30, and 1.31. .... 74

Figure 73 Setting the DXF import Options..... 75

Figure 74 Setting the Gird Size to 10 and enabling the Snap to Gird function..... 75

Figure 75 Geometry of the cliff model after importing the DXF file. .... 75

Figure 76 Setting the surface element size..... 75

Figure 77 Setting the Mesh Refinement Field. .... 76

Figure 78 Final finite element mesh generated for the cliff model..... 76

Figure 79 Specification of Project Options. .... 77

Figure 80 Setting run options in the Irazu User Interface. .... 77

Figure 81 Materials tab in the Irazu User Interface..... 78

Figure 82 Elastic properties. .... 78

Figure 83 Setting strength properties: (a) Strength properties (b) Estimate of Strength Parameters. .... 79

Figure 84 Setting the time variation of the strength parameters. .... 80

Figure 85 Setting the Advanced Properties. .... 81

Figure 86 Completed Materials assignment for the rock cliff model. .... 81

Figure 87 Definition of Boundary Conditions in the Irazu User Interface. .... 82

Figure 88 Complete assignment of Boundary Condition for the cliff model..... 82

Figure 89 Definition of In-situ Stresses in the Irazu User Interface..... 83

Figure 90 Creating a copy of a Run ..... 83

Figure 91 Setting the excavation for subsequent Run..... 84

Figure 92 Setting the DFN Generator..... 84

Figure 93 Modifying the properties..... 85

Figure 94 Coordinate the extreme nodes joint. ....	85
Figure 95 Final geometry of the cliff model. ....	85
Figure 96 Specification of Project Options. ....	86
Figure 97 Setting run options in the Irazu User Interface. ....	86
Figure 98 Setting the time variation of the strength parameters. ....	87
Figure 99 Definition of In-situ stresses in the Irazu User Interface. ....	88
Figure 100 Definition of Discrete Fracture Network in Irazu User Interface. ....	88
Figure 101 Setting the Discrete Fracture Network properties. ....	88
Figure 102 Completed Discrete Fracture Network assignment for the model. ....	89

# Abstract

This study aims to investigate the failure mechanisms and factors influencing cliff stability of soft rock cliffs, specially focusing on a clastic coastal area of the mid-western Adriatic Sea of the Abruzzo region, in Central Italy. The Punta Ferruccio cliff, characterized by conglomerate with notches, stands at a height of 25m, notch depth of 7m, and width of 4m, and serves as the focal point for the analysis. The research explores the impact of notches induced by basal erosion at the cliff and discontinuities, such as joints, on cliff stability. The numerical models of the cliffs are categorized into homogeneous material (without joints) and homogeneous material with joints. The Finite Element Method (FEM) is employed to analyze the progression of notch excavation and its influence on cliff stability using RS2 software. The Finite-Discrete Element Method is used to simulate two cliff types using Irazu 2D software, providing a more accurate depiction of the actual cliff collapse process and enabling comparison with RS2 software results. The Shear Strength Reduction (SSR) method is utilized in the FEM analyses of slope stability, presenting results in terms of the global critical Shear Reduction Factor (SRF) as an indicator of cliff stability. In the case of homogeneous vertical cliffs, varying heights ranging from 25 m to 2.5 m are analyzed, while maintaining constant notch depths of 5 m, 3 m and notch height of 4 m. Additionally, the stability of a homogeneous 25 m high cliff with a slope angle of  $70^\circ$  and varying notch depths (3 m, 5 m, 7 m, and 10 m) is compared to that of a vertical cliff. For homogeneous cliffs with joints, a parametric analysis is carried out and the discontinuities are introduced into the models by adjusting parameters such as joint length and horizontal locations of joint placement relative to the cliff face. This helps in understanding the influence of joints on failure mechanisms and cliff stability. Furthermore, a back analysis of the Punta Ferruccio cliff was conducted to assess the impact of varying joint persistence factors on cliff properties upon failure. The numerical results of the cliff models reveal that an increase in notch depth leads to cliff instability in homogeneous cliffs. Homogeneous cliffs with joint exhibit increased instability with the length and horizontal locations of joints, specially, the position of the joint is close to the notch end. These findings hold significance for further stability assessments and hazard analyses for soft rock coastal areas.

# 1. Introduction

The stability of cliff is a significant concern worldwide due to numerous instances of cliff collapses along coastlines, leading to loss of life, infrastructure, and environmental heritage. The Mediterranean region, in particular, grapples with this issue, prompting numerous studies to predict coast retreat and understand the impact of wave circulation and ocean spray erosion on cliffs. This paper contributes to this scientific discourse.

As highlighted by Miccadei et al. (2019) and Calista et al. (2019), studies in the Mediterranean primarily focus on hard rock coasts, examining geomorphic processes and cliff stability. However, there's a dearth of research on coastal cliffs and slope landforms composed of soft clastic rocks. Soft rock coasts present unique challenges, with decay rates often surpassing those of hard rock cliffs by a hundredfold, ranging from 0.01 to 10 meters per year. Although subject to rapid and localized erosion over short periods, these cliffs exhibit a trend toward consistent and stable decay patterns, with erosional cycles encompassing toe erosion, cliff instability, mass movement, talus deposition, and beach formation and erosion.

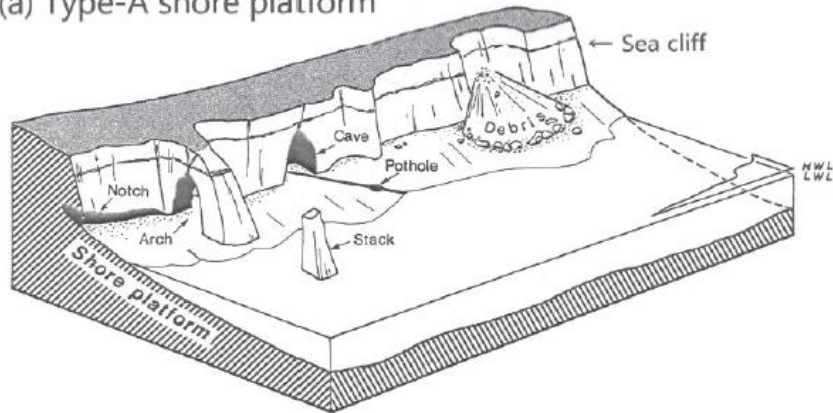
This thesis concentrates on analyzing the cliffs in the Adriatic Sea, in central Italy. It specifically investigates the impact of erosional processes at the cliff base, excluding considerations of wave action, cliff-face weathering, or lithological changes. Utilizing numerical simulations conducted according to the Finite Element Method with RS2 (Program for Two-dimensional Analysis of Rocks and Soils) and the Combined Finite Discrete Element Method implemented in Irazu 2D, the study explores the effects of notch formation on the progression of cliff stability. RS2, a finite element analysis program, simulates incision excavation from basement erosion, providing insights into failure mechanisms and notch depth influence. Additionally, the analysis incorporates discontinuities such as joints. Irazu, a finite discrete element analysis program, addresses large deformations, fracturing, and stability in rock masses. Both software utilizes the shear strength reduction (SSR) method to determine safety factors for assessing stability.

A well-documented rockfall event in Punta Ferruccio in 2014 was back-analyzed by varying the persistence of seams at the notches until the actual configuration was attained. The resulting model was validated and used in subsequent parametric analyses. Specifically, the thesis examines the impact of different joint lengths at various locations on the cliff surface on cliff stability.

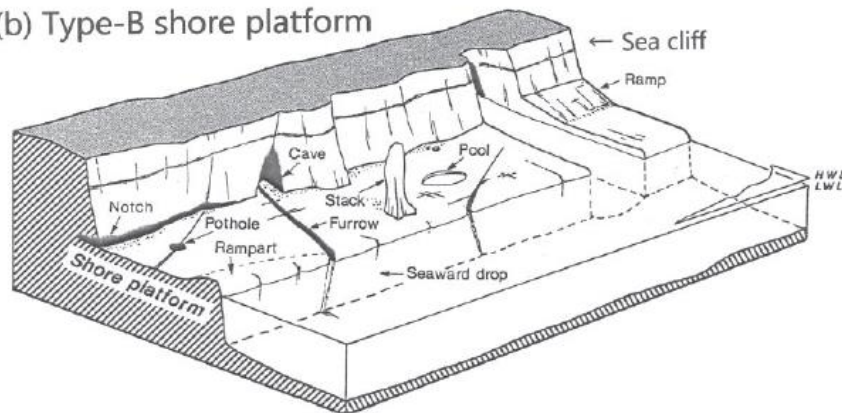
## 2. Erosion of cliffs in coastal areas

Sunamura (2015) studied the rocky coastal processes of soft rock cliffs, categorizing them into two main types: shore platforms and plunging cliffs. Shore platforms are further subdivided into two categories: Type A (sloping) and Type B (horizontal). The A-type platform features a gently sloping erosional surface extending from the base of the sea cliff to below sea level, without significant topographic breaks (Figure 1a). On the other hand, the B-type platform exhibits an almost horizontal erosion surface, situated in front of the sea cliff and terminating in a distinct cliff (Figure 1b). In regions lacking these platforms, plunging cliffs are present, characterized by steep slopes extending well below sea level, forming vertical or semi-vertical faces (Figure 1c).

(a) Type-A shore platform



(b) Type-B shore platform



(c) Plunging cliff

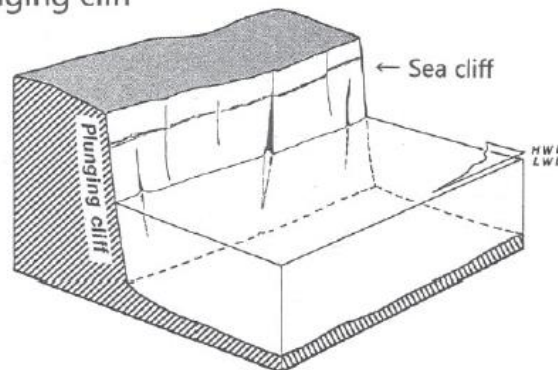


Figure 1 Three major morphologies on rocky coasts: (a) Type-A shore platform (sloping type), (b) Type-B shore platform (horizontal or sub-horizontal type) and (c) plunging cliff. From Sunamura (2015).

The evolution of rocky coasts is closely linked to cliff recession, influenced by various factors including water level, cliff front beach, cliff base platform, nearshore bottom topography, and cliff toe talus. Water levels, the first major factor, significantly impact coastal erosion by affecting wave energy levels and tides at cliff bases. Global sea level changes, seasonal fluctuations, and storm surges all influence erosion processes. The fronting beach, as the second major factor, plays a pivotal role in erosion, particularly in soft cliff areas where wave impact and water level fluctuations directly drive erosion. Wider beaches generally correlate with lower erosion rates. Wave strength at the cliff base, the third factor, can be influenced by shore platform geometry and size. Nearshore bottom topography, the fourth factor, affects wave action on cliffs through refraction or energy attenuation, weakening wave impact. Lastly, the talus at the cliff foot controls erosion by shielding it against waves until it is eventually washed away.

Moreover, cliff stability is influenced by additional factors beyond those mentioned above. Rainfall and groundwater are primary drivers of cliff collapse, causing gully erosion and collapse. Frost action, occurring mainly at mid-to-high latitudes, promotes material movement on cliff faces. Earthquakes in tectonically active regions and tree root growth within joints can also trigger cliff failures.

Antonioli et al. (2015) investigated carbonate coastal tidal notches across 73 locations in Italy, France, Croatia, Montenegro, Greece, Malta, and Spain. They identified four main processes—biological agents, wet-dry cycles, salt weathering, hyperkarst processes, and mechanical erosion—responsible for notch formation. Tidal gaps analyzed averaged 45-70 cm wide and 40-100 cm deep. Notch width consistently exceeded the mean tidal range but fell short of maximum and minimum tidal ranges. Notch depth increased in exposed areas compared to protected ones, suggesting wave action and tidal range influence notch formation differently.

Terefenko and Terefenko (2014) studied a 28 km coastal stretch in Portugal, observing 242 notches categorized into U-shaped (54.13%), V-shaped (44.21%), and Ripple (1.65%). Notch shape varied with coastal exposure, with V-shaped prevalent in highly exposed areas and U-shaped in less exposed ones. Wave forces and chemical resistance shape exposed cliff notches, influenced by tides, sea level changes, and neotectonic movements. ( [Figure 2](#) )

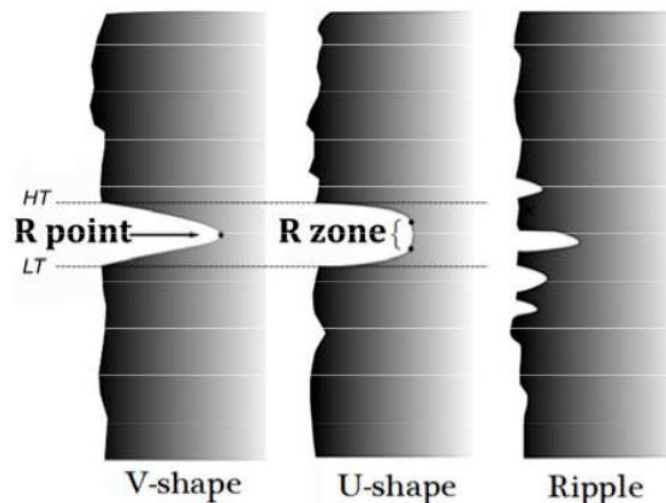


Figure 2 Basic notch shapes. HT: high tide, LT: low tide, R point: retreating point, R zone: retreating zone. From Wziatek et al. (2011).

Kogure et al. (2006) delved into the effects of notch and pull-out development on limestone coastal cliff instability in the Ryukyu Islands, Japan. Their study offers a comprehensive explanation of toppling failure attributed to notch and tensile crack development, drawing from actual sampling, model assumptions, theoretical reasoning, and experiments.

Kogure and Matsukura (2011) investigated coastal cliff collapses at Kuro-Shima, Okinawa, Japan, establishing a correlation between the geographical distribution of cliff collapse shapes and joint development.

Lollino et al. (2018) utilized advanced computational techniques to simulate post-failure rock fragmentation processes resulting from material brittleness. Their study, employing a coupled finite/discrete element code, captured post-peak stress-strain behavior under mode I and mode II failure mechanisms, while also considering the impact of sea-level erosion and rock degradation, enhancing the realism of the simulated failure process.

Miscevié and Vastelica (2014) discussed the significance of slope instability due to weathering of soft rock masses, highlighting its repercussions across various weathering fields. In addition to material degradation on slope surfaces, there's a reduction in shear strength within the slope. The dry-wet, heating-cooling, and freeze-thaw cycle processes profoundly influence weathering development. They propose two types of protective measures: avoiding the removal of degrading materials from slope surfaces and installing surface protection such as geosynthetics, vegetation cover, and shotcrete.

### 3. The Study area

Mikady et al. (2019) and Calista et al. (2019) investigated the study area located on the Adriatic coast, which lies between the Piedmont terrain of the Apennine orogen on the northeastern edge and the Adriatic continental shelf (Figure 3). The Piedmont coastal region contains the central Apennine fold-thrust belt buried under the clastic marine transitional continent (Late Miocene Pleistocene).

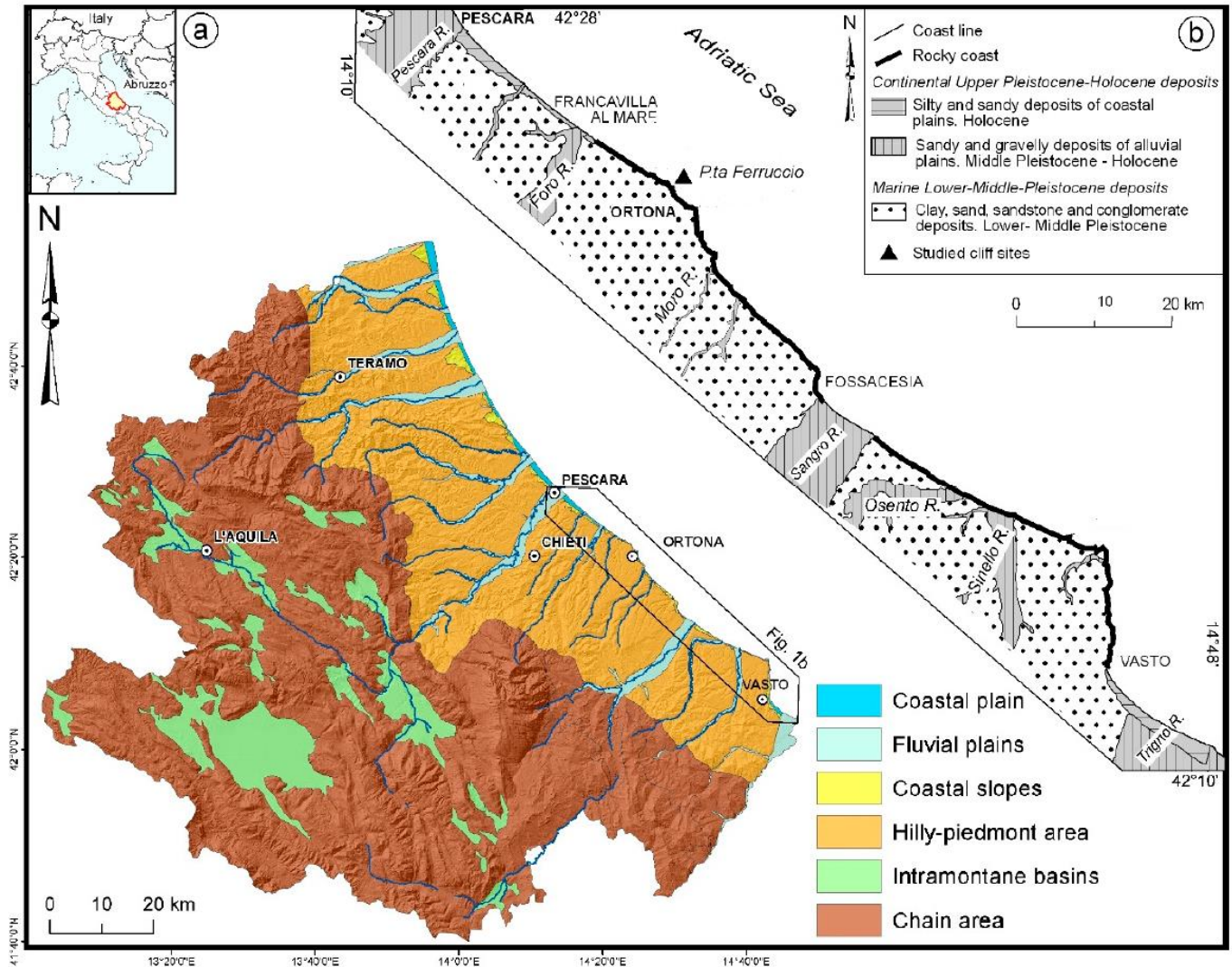


Figure 3 (a) The main physiographic domains of the Abruzzo region (according to the morphotectonic landscape classification, D'Alessandro et al. 2003). The black polygon indicates the study area. (b) The lithological scheme of the study area and location of the cliff sites (modified from Miccadei et al. 2019).

The rocky coastal areas of the central Adriatic Sea are highly variable in morphology. The formation of the rocky coast is based on an uplifted clay-sandy-grainy marine sequence (Early Pleistocene-Middle Pleistocene) that was overlain by continental sediments (Late Pleistocene-Holocene). Competing coastal erosion and landslides can damage cliffs, while large rotational and translational landslides can affect coastal slopes.



Coastal slopes and cliffs are classified as 1) sandstone cliffs, 2) conglomerate cliffs, 3) ancient landslide deposits coastal slopes, and 4) late Quaternary slopes continental sediment cliffs because they form from different bedrock types and changes between the upper toes and top. More than 15% of the area is covered by conglomerate cliffs that characterize the study area of Punta Ferruccio promontory (Figure 4).

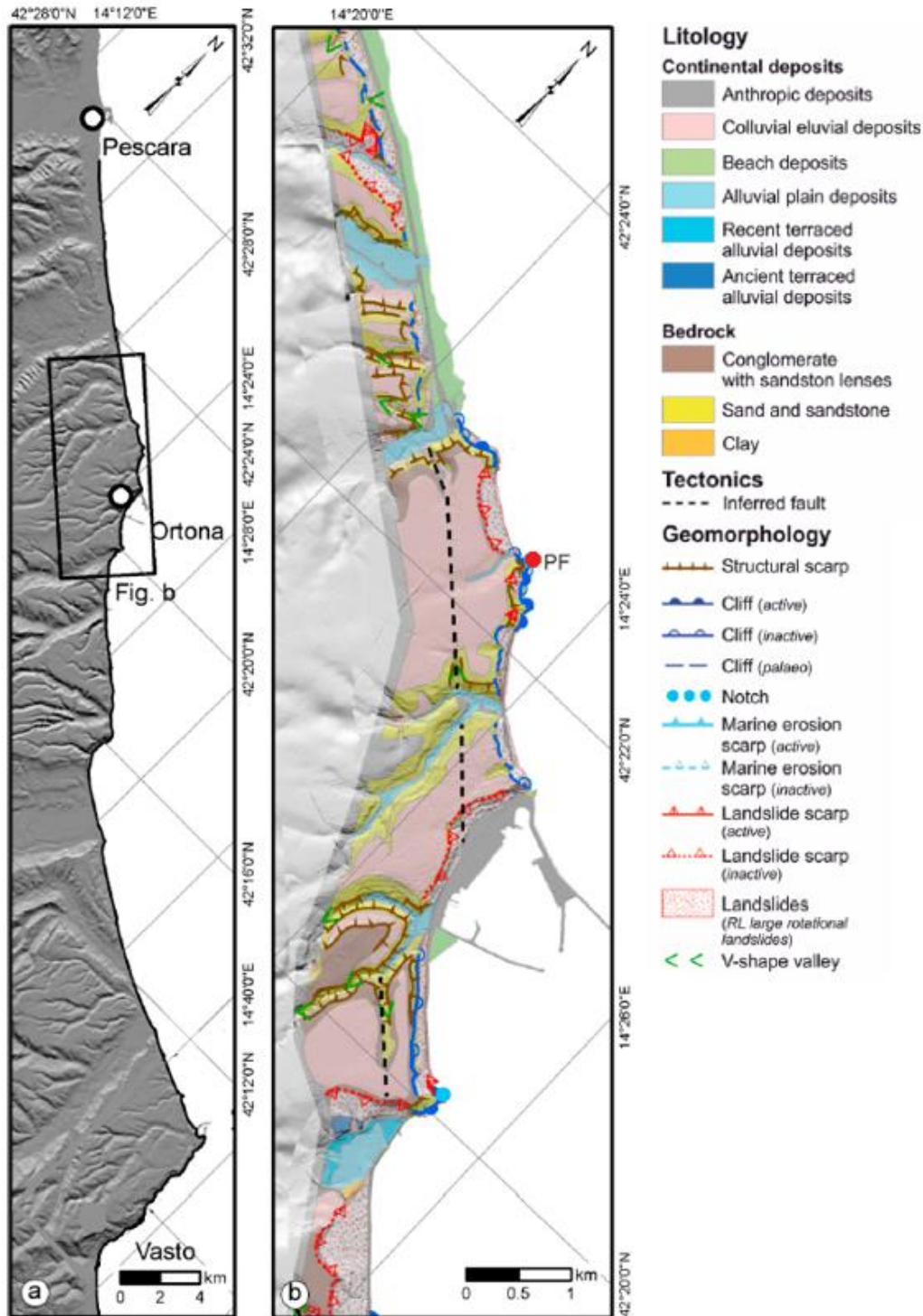


Figure 4 (a) Location of the studied areas; (b) schematic geomorphological map of the Ortona coastal sector (modified from Miccadei et al. 2019). Legend: PF: Punta Ferruccio cliff.

The Punta Ferruccio study area features vertical cliffs reaching heights of around 25 m. Notches, developed in poorly cemented clay-sandstone interbeds at the cliff bases, extend inward and upward to depths of 7m and heights of 4m. Geomorphological surveys indicate major landslides between 2004 and 2005, affecting the cliff edge with similar structural conditions, leading to cliff collapse (L1 in Figure 5b, e). Subsequent field investigations in 2014 (L2 in Figure 5c, f) identified a large collapsed landslide impacting a substantial rock wedge at the cliff's edge (Miccadei et al. 2019; Calista et al. 2019). Consequently, Punta Ferruccio is deemed an active cliff, varying in height from 5 to over 25 m. Active decay is rapid but intermittent, occurring over short periods. Changes in the notch and cliff failure processes were observed over several decades, with estimated retreat rates reaching as high as 0.85 meters per year.

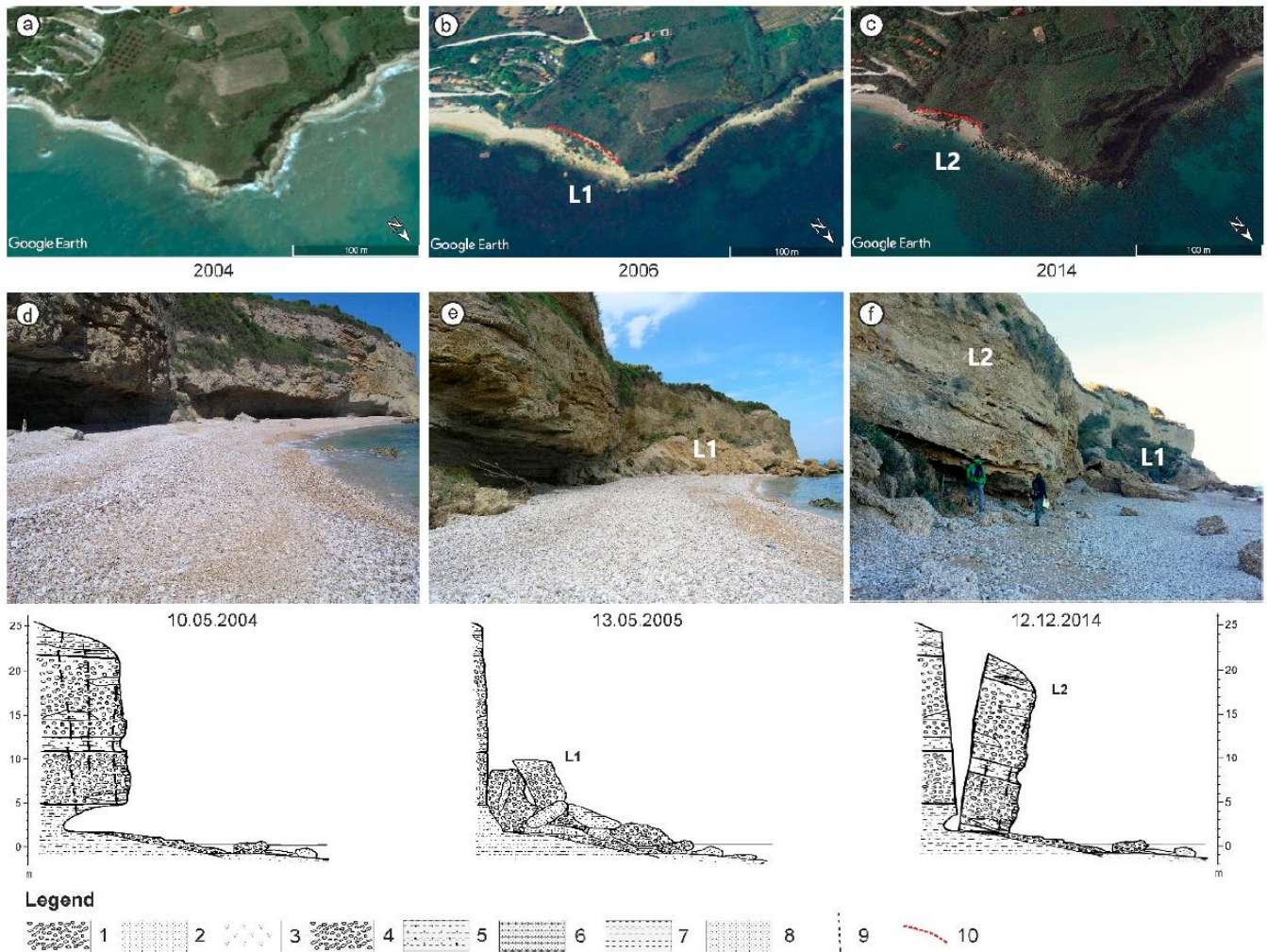


Figure 5 The Punta Ferruccio cliff. Aerial images from (a) 2004, (b) 2006, and (c) 2014; cliff image and The Punta Ferruccio cliff. Aerial images from (a) 2004, (b) 2006, and (c) 2014; cliff image and geomorphological sections from (d) 2004, (e) 2005, and (f) 2014 outlining the rockfall that occurred in 2004–2005 (L1) and the topple that occurred in 2014 (L2), controlled by the main joints and notch. Legend: 1. Gravel, 2. Sand, 3. Landslide deposits, 4. Conglomerate, 5. Sandy Clay, 6. Sandstone, 7. Clay, 8. Sand, 9. Main joint, and 10. Landslide scarp. L1, 2004–2005 rockfall; and L2, 2014 topple. From Calista et al. (2019).

According to the erosion cycle, the main factors controlling cliff evolution are cliff height, notch depth, rock strength, and the location of the tensile stresses. Notches can be cut up to 7-10 meters before the cliff becomes unstable (resulting in toppling and falling failures).

## 4. Numerical analyses of cliffs

### 4.1 Material of cliff

Punta Ferruccio features vertical cliffs exceeding 25m in height. Notches at the cliff base are situated within poorly cemented clay sandstone interlayers within the conglomerate, reaching depths of up to 7m and heights of up to 4m. The primary geological bedrock of Punta Ferruccio consists of a tens-meter-long conglomerate laying over a sandy clay layer. For the sake of simplicity and also for having results of general validity, the simplified model used for numerical simulation excludes the overlying layers, which include eluvial and colluvial deposits, as well as active and dormant landslides ( the superficial deposits less than 3 meters in thickness: Calista et al. 2019).

The properties of conglomerates and joints can be obtained from previous studies. Materials with uniaxial compressive strength less than 5 MPa can also be considered soft materials (Sunamura, 2015). The input parameters remained unchanged throughout the analysis, as shown in [Table 1](#).

*Table 1 Physical mechanical parameters of the lithotypes. From Calista et al. (2019).*

Strength parameter for rock mass	Value and physical units	Strength parameter for joint	Value and physical units
Unit weight ( $\gamma$ )	2100kg/m <sup>3</sup>	Cohesion ( $j_c'$ )	1.00E+04 Pa
Bulk modulus (K)	2.00E+08 Pa	Friction angle ( $j_{\phi}'$ )	30°
Shear modulus (G)	1.20E+08 Pa	Normal stiffness ( $j_{k_n}$ )	1.20E+08 Pa/m
Tensile strength ( $\sigma_{tm}$ )	3.80E+05 Pa	Shear stiffness ( $j_{k_s}$ )	1.20E+08 Pa/m
Friction angle ( $\phi'$ )	45°		
Cohesion ( $c'$ )	3.80E+05 Pa		

### 4.2 FEM analyses of cliffs.

The geometry of the Punta Ferruccio cliff is simplified with a height of 25 meters, a notch depth of 7 meters, and a width of 4 meters, assuming the cliff face is perfectly vertical for the horizontal axis. Additionally, the coastal platform at the cliff base is mainly characterized by a sandy seafloor with a slope of approximately 2%, as reported by Miccadei et al. (2019). In this study, notch height denotes the elevation difference between the roof and floor of the notch, while notch depth refers to the horizontal distance from the tip (deepest part of the notch) to the vertical plane where the height is measured, as defined by Trenhaile (2016). Cliff height represents the vertical distance from the center of the notch to the top of the cliff, as illustrated in [Figure 6](#).

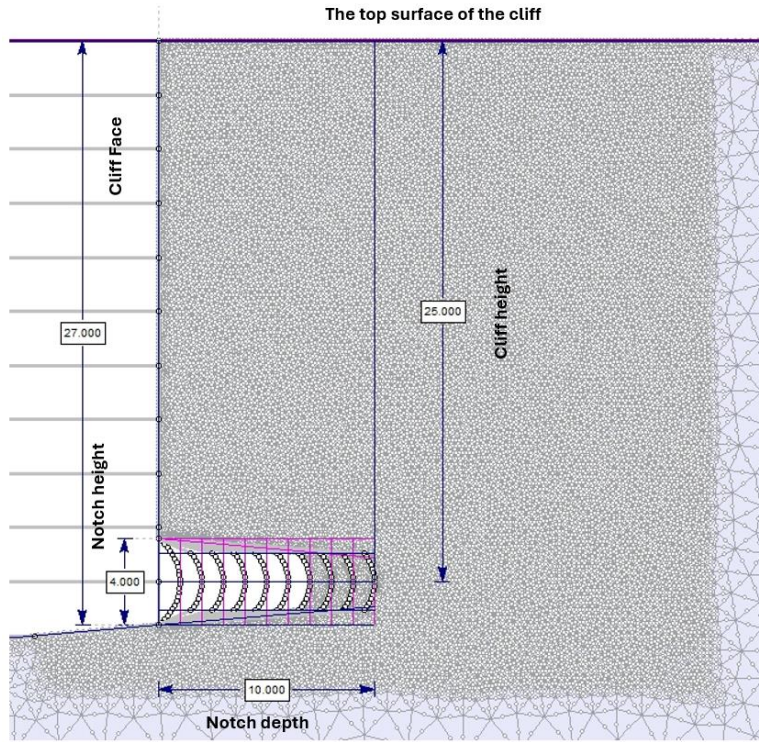


Figure 6 Geometry of the homogeneous vertical cliff without joint.

A perfect elastoplastic constitutive model with the Mohr-Coulomb strength criterion is assumed for all materials involved. Additionally, the Shear Strength Reduction method is utilized in the finite element method to compute the critical strength reduction factor (SRF) of the model and assess the overall stability of the cliff. The Mohr-Coulomb shear strength of the initial cliff is reduced by a factor  $F$ , known as the "Shear Strength Factor." This factor is defined as follows:

$$\frac{\tau}{SRF} = \frac{c'}{SRF} + \frac{\tan\phi'}{SRF} \quad (1)$$

$$\frac{\tau}{SRF} = c^* + \tan\phi^* \quad (2)$$

Where:

$$c^* = \frac{c'}{SRF} \quad (3)$$

$$\tan\phi^* = \frac{\tan\phi'}{SRF} \quad (4)$$

After each reduction step, a finite element stress analysis is conducted. This iterative process continues for various SRF values until the model reaches instability, which is indicated by the non-convergence of the analysis results. Ultimately, the critical SRF is the one for which convergence is not obtained.

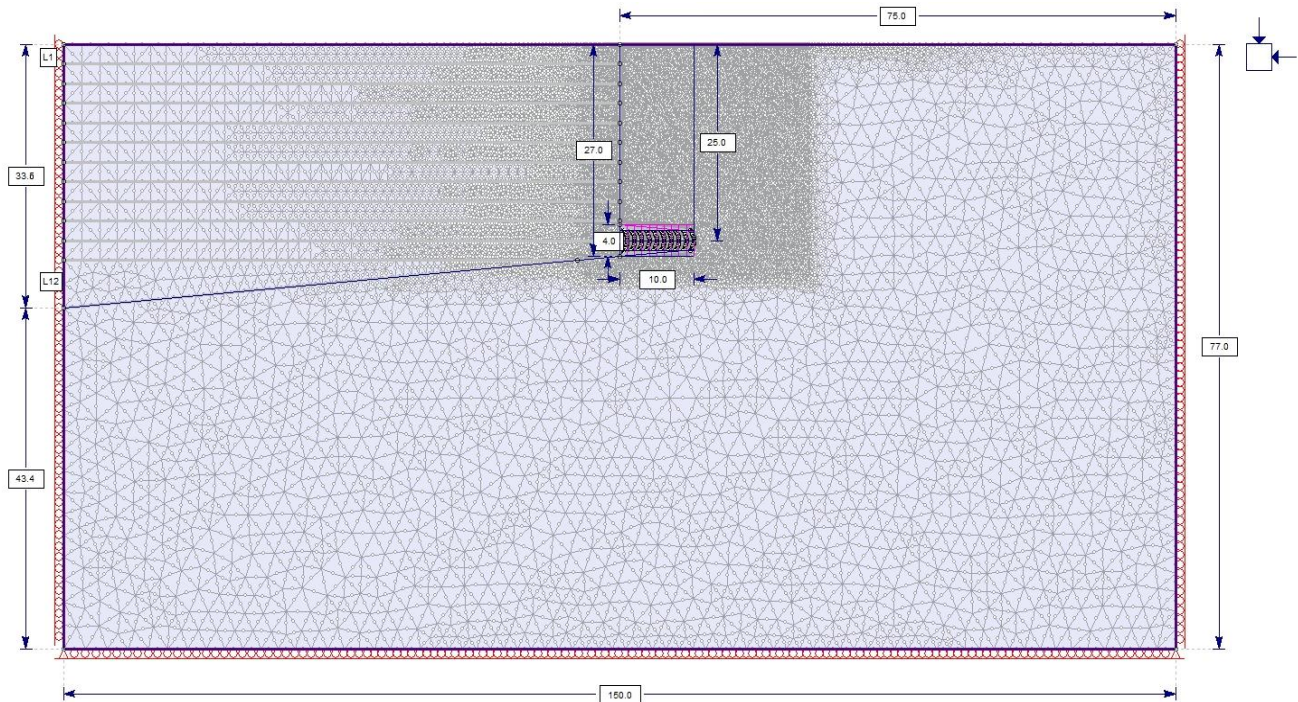


Figure 7 Simplified numerical model of the Punta Ferruccio in RS2

For the initial model, the boundary dimensions extend broadly to 150 meters for both the left and right directions of the cliff face, while the vertical boundary extends below the base of the cliff to approximately 75 meters.

Regarding boundary conditions, the left and right sides of the models are restrained in the x-direction, while the bottom part of the model is restrained in the y-direction. The two corners of the bottom side are fully restrained in both the x and y directions. In contrast, nodes on the slope surface are left without any restraints.

The 2D model is discretized using a graded mesh with 6-node triangular elements, with an approximate total of 35,000 grid cells. For more precise results, the density of the mesh is increased in areas close to cliff faces and notches, while the grid in surrounding areas remains unchanged.

The analysis involves three stages:

1. initial conditions, representing static conditions;
2. progressive excavation of 2.5-meter layers to obtain the final slope profile, conducted in 12 stages (from L1 to L12); to avoid stress modeling disturbance
3. excavation of notches at 1-meter intervals, simulating notch formation due to basement erosion.

The parametric analysis considers different cliff heights, ranging from 25 meters to 2.5 meters.

All analyses are performed under static conditions, with the cliff model subjected to field stresses obtained by gravity loads on the actual ground. The ratio of vertical earth stress to horizontal earth pressure is equal to 1.

### 4.2.1 Homogeneous vertical cliff without joint

The first part of the study aims to analyse the effect of base notch depth on induced cliff failure. The cliff is considered a homogeneous continuum, composed primarily of conglomerates, with no physical discontinuities. The notch depths are assumed to be 3m and 5m, with different cliff heights, as follows:

- In the case of a 5 m notch depth, the cliff heights have been varied as follows: 25 m, 22.5 m, 20 m, 17.5 m, 15 m, 12.5 m, 10 m, 9 m, 8.5 m, 7.5 m, 7 m, 6 m, 5 m, 4 m, 3.5 m, and 3 m.
- In the case of a 3 m notch depth, the cliff heights have been varied as follows: 25 m, 22.5 m, 20 m, 17.5 m, 15 m, 12.5 m, 10 m, 8.5 m, 7.5 m, 7 m, 6 m, 5 m, 4 m, 3 m, and 2.5 m.

These analyses allow us to analyse correlations between cliff height, safety-critical factors, and notch depth. Furthermore, the failure mechanism of the homogeneous cliff is studied through the results of yield distribution and maximum shear strain.

### 4.2.2 Homogeneous inclined cliff without joint

This section investigates the impact of slope inclination on cliff stability. The cliff is treated as a uniform continuum predominantly comprised of conglomerates without any joints. A slope angle of  $70^\circ$  (the angle between the left side surface of the cliff and the horizontal) is considered, along with notches of depths 3m, 5m, 7m, and 10m, as illustrated in [Figure 8](#).

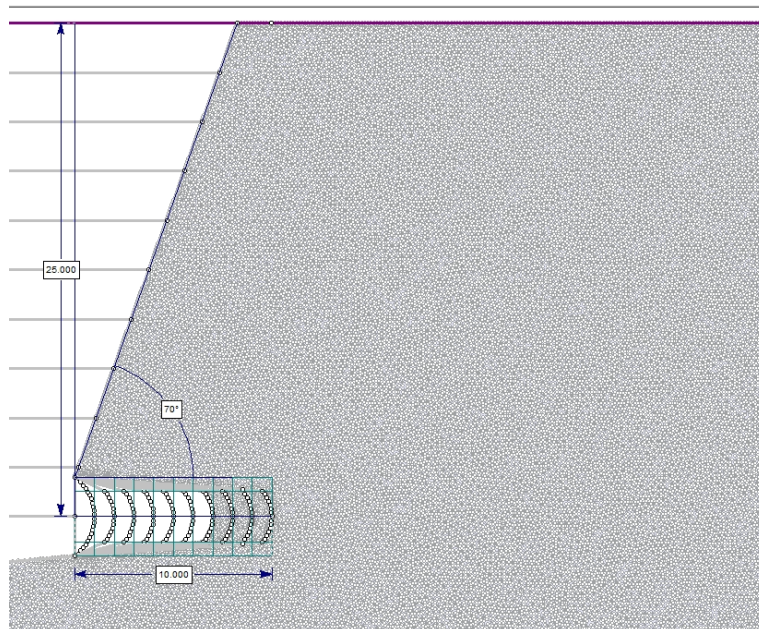


Figure 8 The model of a homogeneous inclined cliff without a joint.

These analysis results allow us to compare the yield distribution and maximum shear strain differences between vertical and inclined cliffs, thereby assessing their stability and changes in failure mechanisms.

### 4.2.3 Homogeneous vertical cliff with joint

This section aims to study the impact of discontinuities (especially vertical joints) on the stability of cliff-notch systems. The joint was modeled by assigning the properties, shown in Table 1. The tensile strength of the joint was assumed to be approximately one-tenth the tensile strength of the conglomerate material. The tensile strength of the joint is calculated as follows:

$$\sigma_{joint}^t = \frac{1}{10} \sigma_{rock\ mass}^t = \frac{1}{10} \times 0.38\ MPa = 0.038\ MPa \quad (5)$$

In RS2 the mesh density in the joint area is increased for a more accurate analysis. The joint end condition is treated as "First point open/Last point closed", where the first point is on the top face of the cliff.

Based on the evidence that an instability event occurred in 2014 Punta Ferruccio cliff, which collapsed due to notches in the toe cliffs and major joints, a back analysis, was performed. The joint persistence (unknown) was used as a key parameter for the back-analysis. Its change was simulated by appropriately varying the relevant joint parameters (friction angle, cohesion, and tensile strength) until the value of the critical Shear Strength Factor was 1. For this purpose, the following equations are used:

$$\varphi = p * (\varphi_{joint}) + (1 - p) * (\varphi_{rock\ mass}) \quad (6)$$

$$c = p * (c_{joint}) + (1 - p) * (c_{rock\ mass}) \quad (7)$$

$$\sigma_{t,joint} = (1 - p) * (\sigma_{t,rock\ mass}) \quad (8)$$

Where  $\varphi_{joint}$  and  $\varphi_{rock\ mass}$  represent friction angle of the joint and rock mass;  $c_{joint}$  and  $c_{rock\ mass}$  are the cohesion of the joint and rock mass  $\sigma_{t,joint}$  and  $\sigma_{t,rock\ mass}$  represent the tensile strength of the joint and rock mass;  $p$  is the persistence, i.e. the length of the joint trace.

In this study a conglomerate cliff model with 23.75m and 18.75m depth joints at different locations was adopted, considering a constant cliff height of 25 m, a notch depth of 7 m, and a height of 4 m.

The results are expressed in terms of critical SRF, maximum shear strain, and yielded elements distribution, providing insight into the stability of the cliff under the influence of discontinuities such as a joint.

## 4.3 FDEM analyses of cliffs

The purpose of this section is to use the FDEM Irazu software to conduct a simulation analysis of the stability and failure mechanisms of cliffs. The results are compared with those obtained from FEM analysis to determine the respective advantages and disadvantages of each approach.

Irazu software (Version 6.1) implements the Combined Finite Discrete Element Method (FDEM), originally developed by Mungiza et al. in 1995. This method facilitates dynamic simulations involving multiple interacting objects. In the FDEM, simulations can begin from either a single holonomic domain or a collection of discrete holobodies. Throughout the simulation, these objects can elastically deform, translate, rotate, interact, and undergo fracture when specific criteria are met, resulting in the creation of new discrete objects. These newly generated objects can experience further movement, interaction, deformation, and fracture. The FDEM integrates finite element method (FEM) techniques to evaluate induced deformation, while discrete element method (DEM) concepts are utilized to detect new contacts and manage the translation, rotation, and interaction of discrete bodies. This integration allows for comprehensive simulations of dynamic interactions and failure processes.

This analysis maintains the same cliff geometry and material properties as those used in the RS2 software. Additionally, the fracture energy for mode I and mode II of the model is estimated according to Zhang's (2002) formulations:

$$K_{IC} = \frac{\sigma_t}{6.88} \quad (9)$$

$$E' = \frac{E}{(1 - \nu^2)} \quad (10)$$

Mode I Fracture Energy:

$$G_I = \frac{K_{IC}^2}{E'} \quad (11)$$

Mode II Fracture Energy:

$$G_{II} = 10G_I \quad (12)$$

Where  $\sigma_t$  and  $K_{IC}$  represent the tensile strength and Mode I fracture toughness of rock;  $E$  and  $\nu$  represent Young's Modulus and Poisson's Ratio.

### 4.3.1 Homogeneous vertical cliff without joint

Four different models are established and analyzed using Irazu software to determine if the simulation of the progressive erosion process influences significantly the results. The models are characterized as follows:

- Homogeneous vertical cliff without joint and excavation stages.

As illustrated in [Figure 9](#) and [Figure 10](#), the first model represents a 25-meter-high homogeneous cliff with a 4-meter high and 7-meter-deep notch, devoid of any joints and notch excavation stage. Additionally, by setting a mesh refinement area to increase the mesh density around the notch and the cliff above it, a total of approximately 50,000 mesh elements are formed.



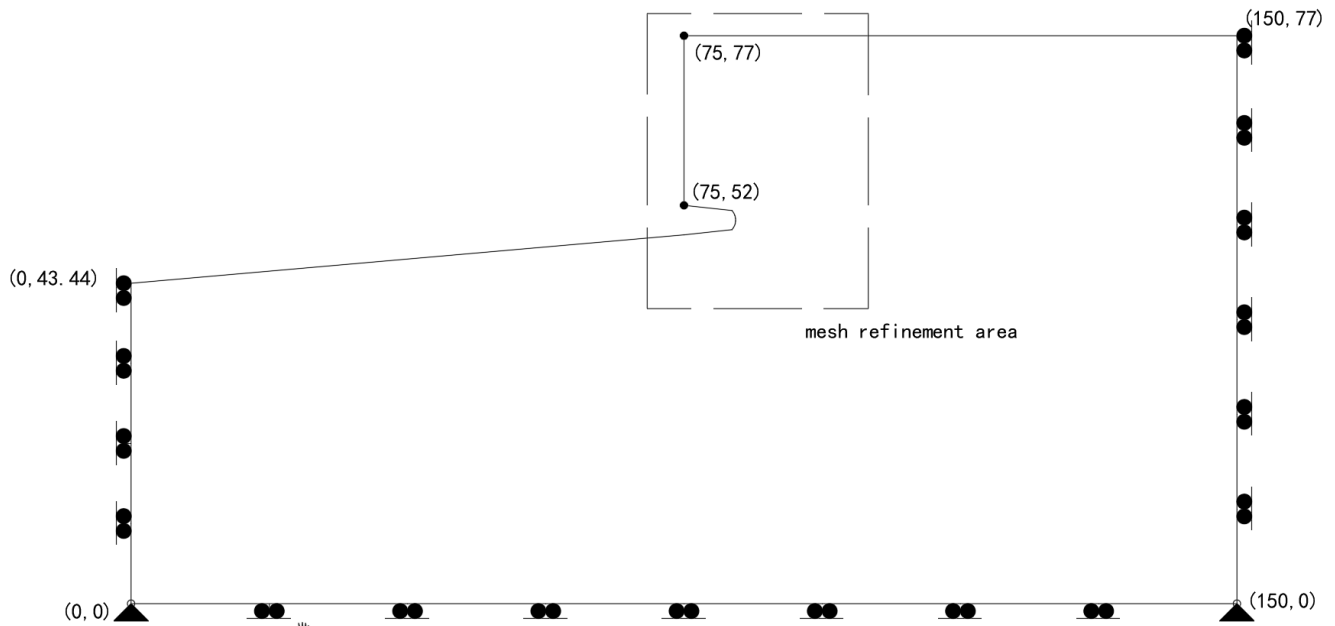


Figure 9 Coordinates defining the homogeneous vertical cliff without joint and excavation stages geometry.

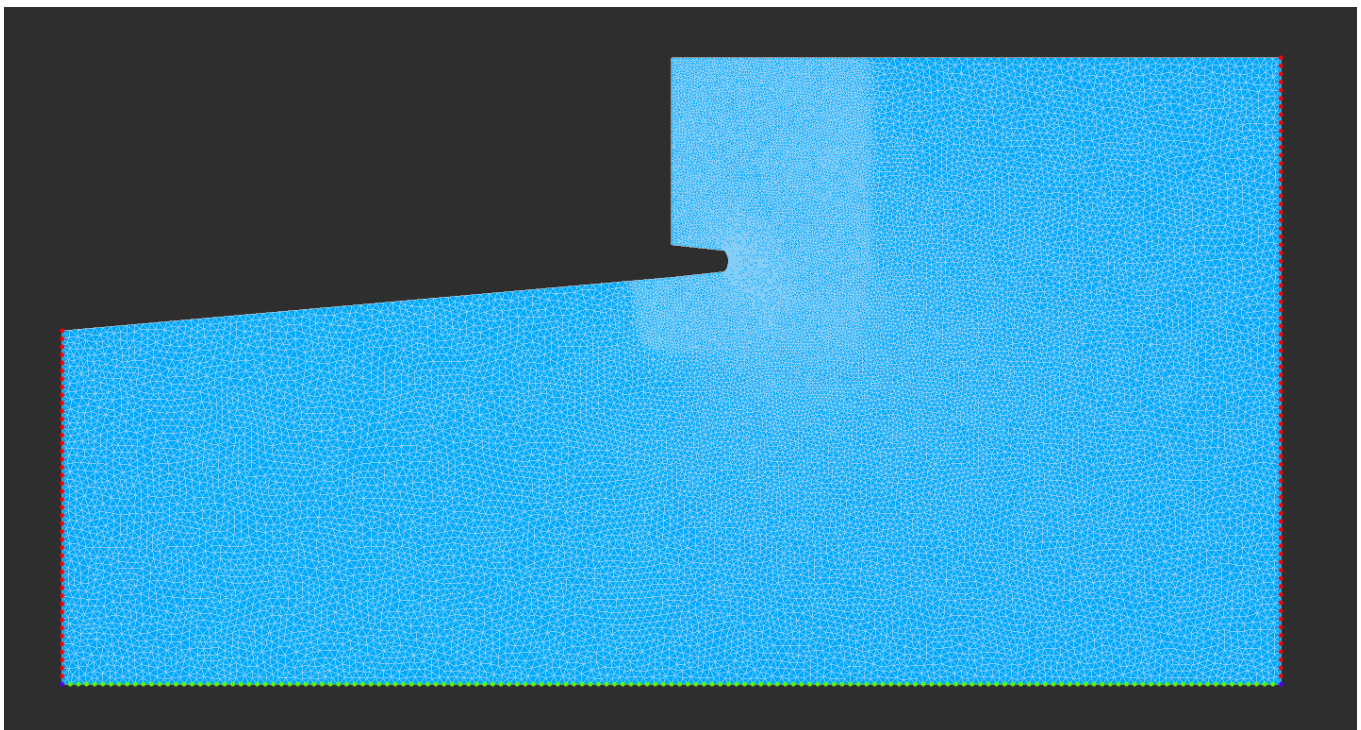


Figure 10 Final finite element mesh generated for the homogeneous vertical cliff without joint and excavation stages model.

- Homogeneous vertical cliff without joint, with 2-notch excavation stages.  
 This model represents a 25-meter-high homogeneous cliff with two excavation stages of a 4-meter-high notch at the base to simulate seawater erosion. The first excavation depth is 3.5 meters, followed by a second excavation depth of 7 meters. Additionally, there are no joints in this model. The mesh settings remain consistent with the first model, as shown in [Figure 11](#) and [Figure 12](#).

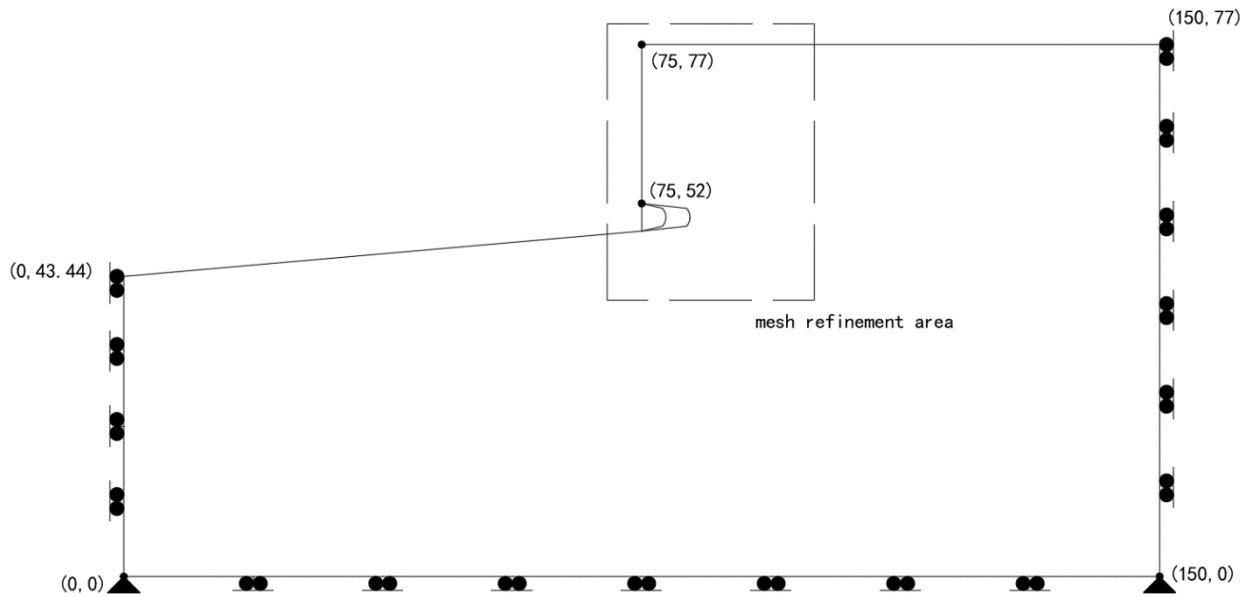


Figure 11 Coordinates defining the homogeneous vertical cliff without joint, with 2-notch excavation stages geometry.

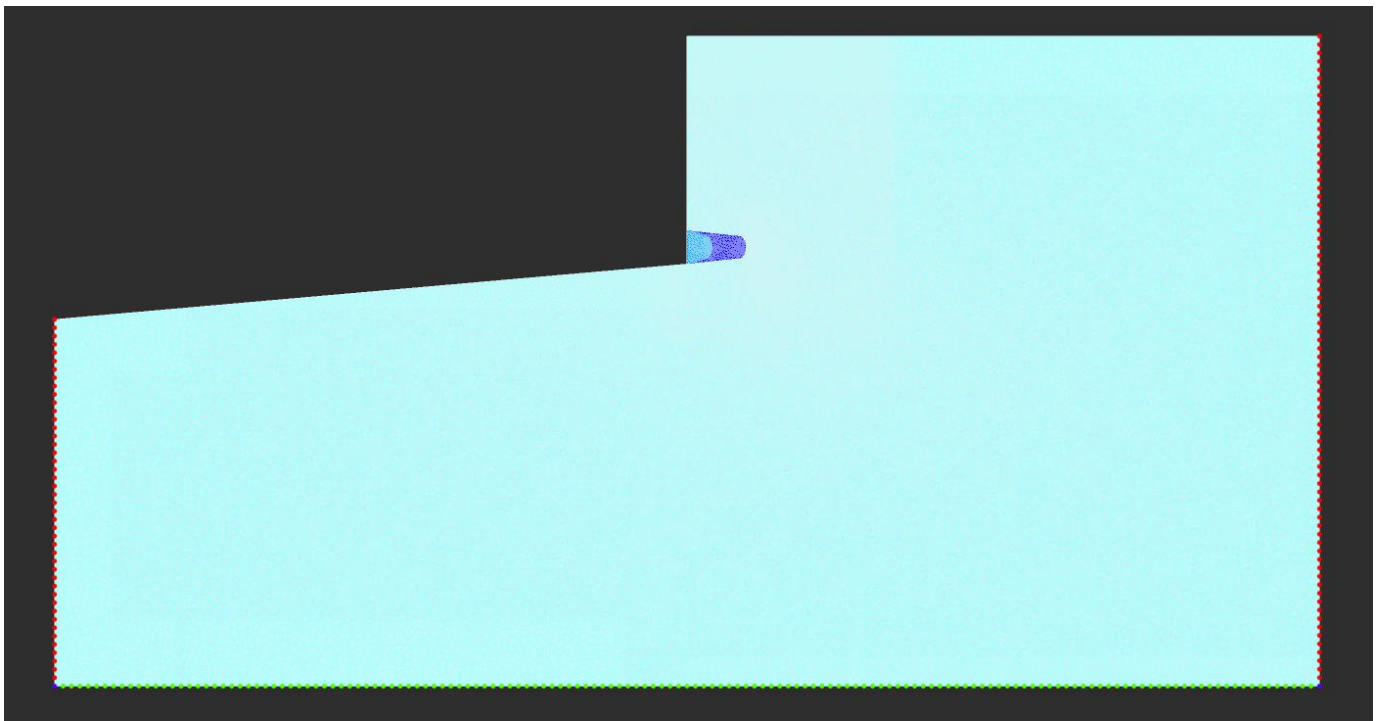


Figure 12 Final finite element mesh generated for the homogeneous vertical cliff without joint, with 2-notch excavation stages model.

- Homogeneous vertical cliff without joint, with 4-notch excavation stages.

The third model shows a 25-meter-high homogeneous cliff with four-notch excavation stages at the base of the cliff. The first excavation depth is 1 meter, the second excavation depth is 1.5 meters, the third excavation depth is 1.5 meters and the fourth excavation depth is 3 meters. Furthermore, the mesh setting remains unchanged as shown in [Figure 13](#) and [Figure 14](#).

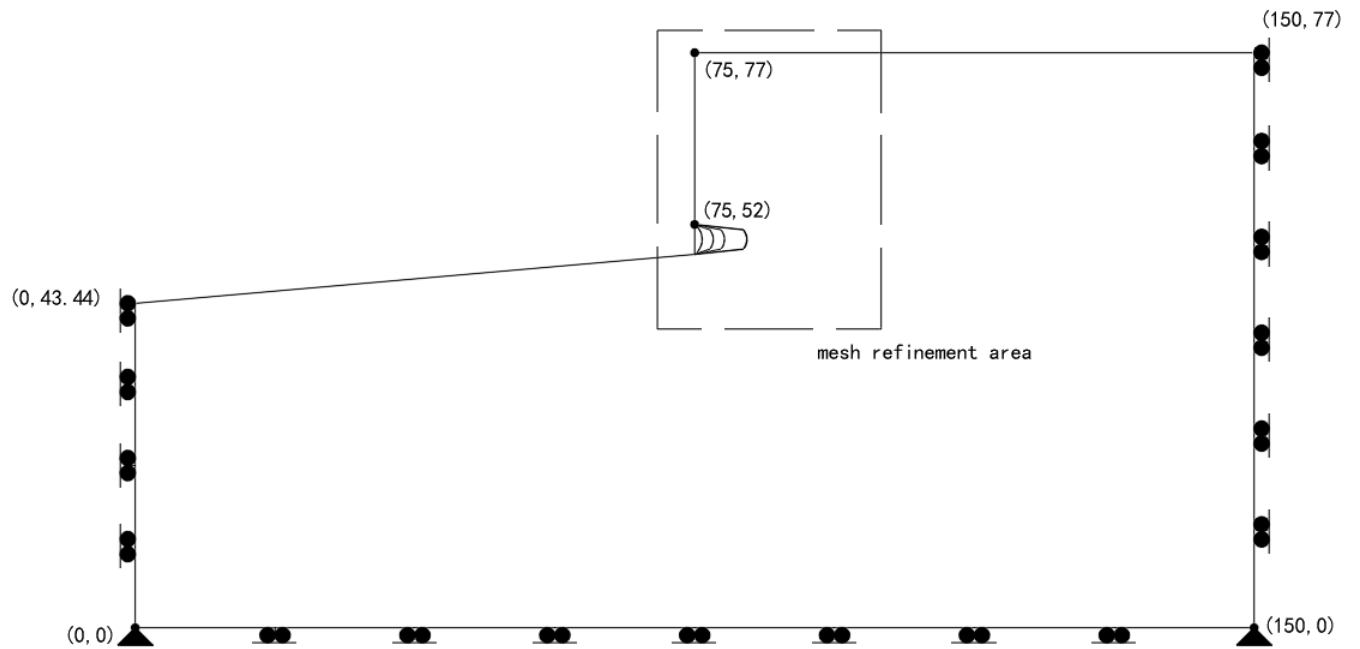


Figure 13 Coordinates defining the homogeneous vertical cliff without joint, with 4-notch excavation stages geometry.

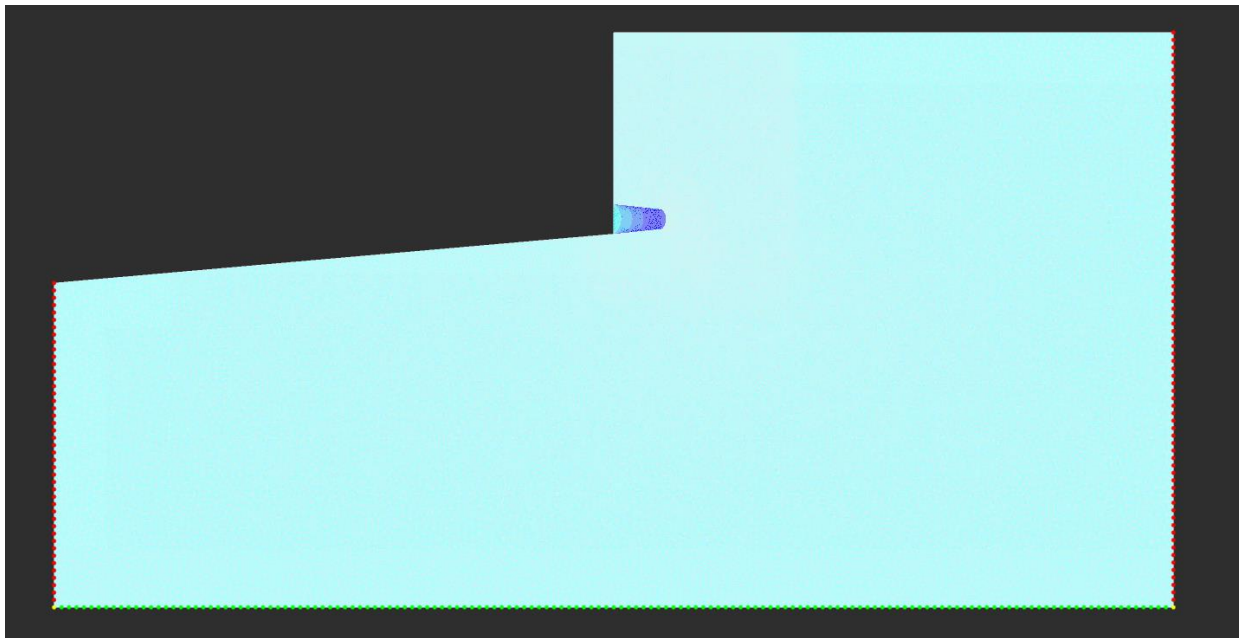


Figure 14 Final finite element mesh generated for the homogeneous vertical cliff without joint, with 4-notch excavation stages model.

- Homogeneous vertical cliff without joint, with 10 vertical and 4-notch excavation stages.

For the fourth model, the boundary dimensions are significantly extended to 150 meters horizontally along the cliff face and approximately 75 meters vertically below the cliff base, resulting in a rectangular homogeneous model. The eleven vertical excavations, each approximately 2 meters deep, were conducted on the left side of the cliff to form a 25-meter-high vertical cliff. Subsequently, the four notch excavation steps of the previous model were performed (the first with a depth of 1 meter, the second with a depth of 1.5 meters, the third with a depth of 1.5 meters, and the fourth with a depth of 3 meters). The mesh settings remain unchanged, as shown in [Figure 15](#) and [Figure 16](#).

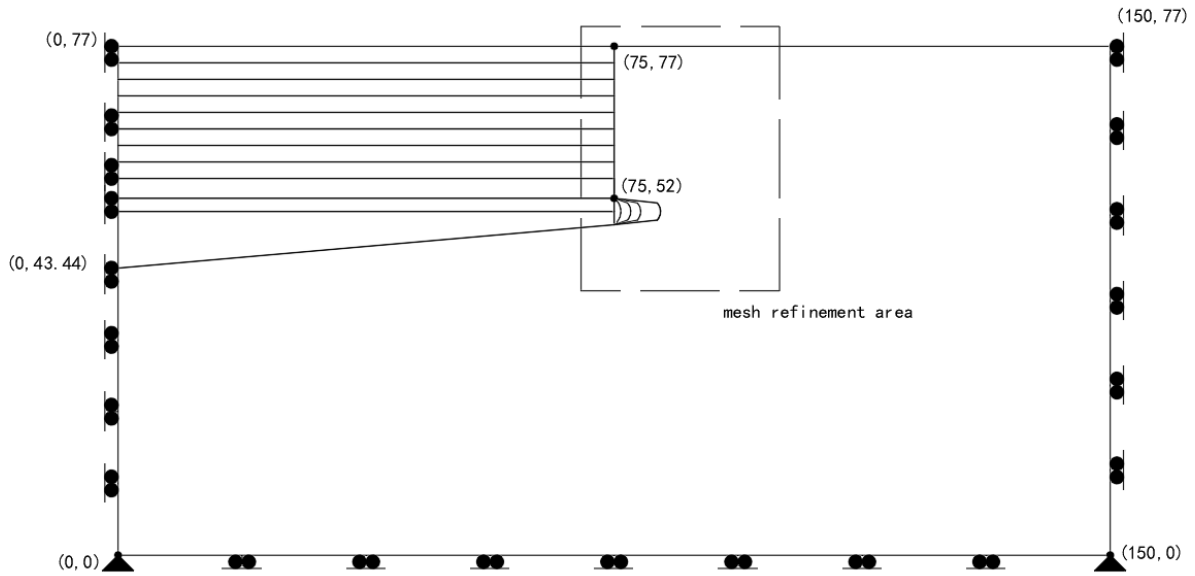


Figure 15 Coordinates defining the homogeneous vertical cliff without joint, with 10 vertical and 4-notch excavation stages geometry.

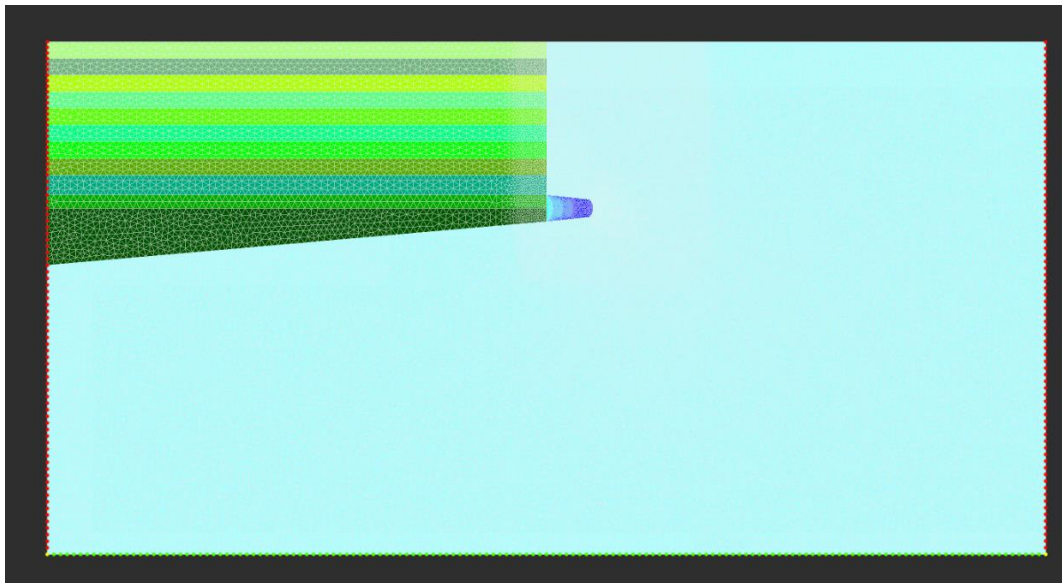
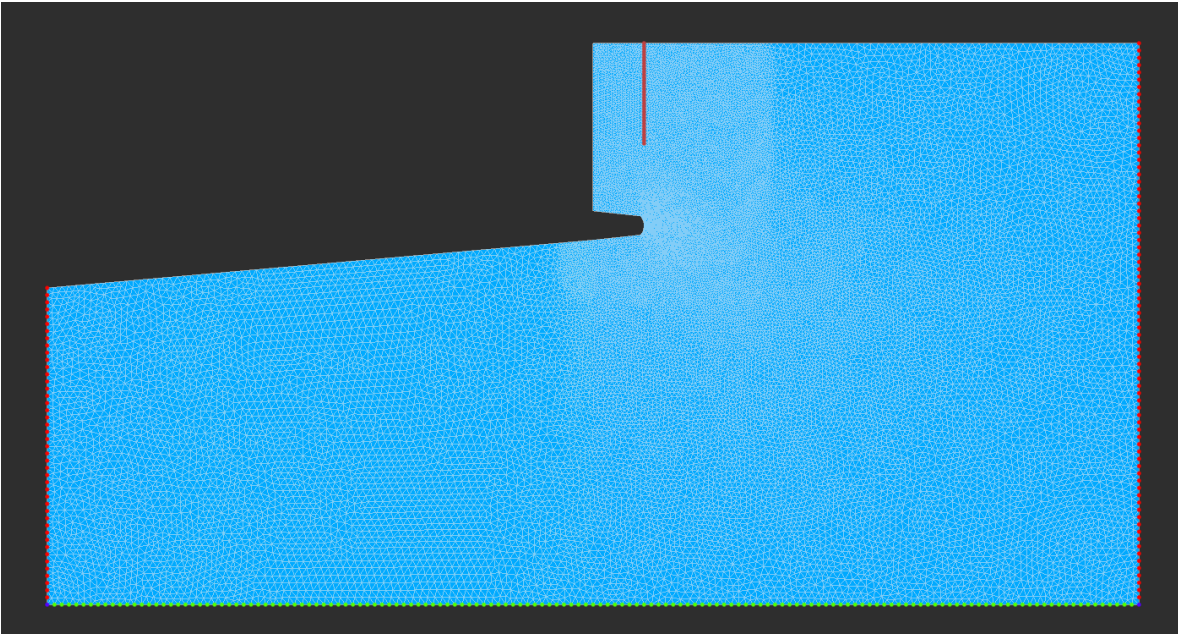


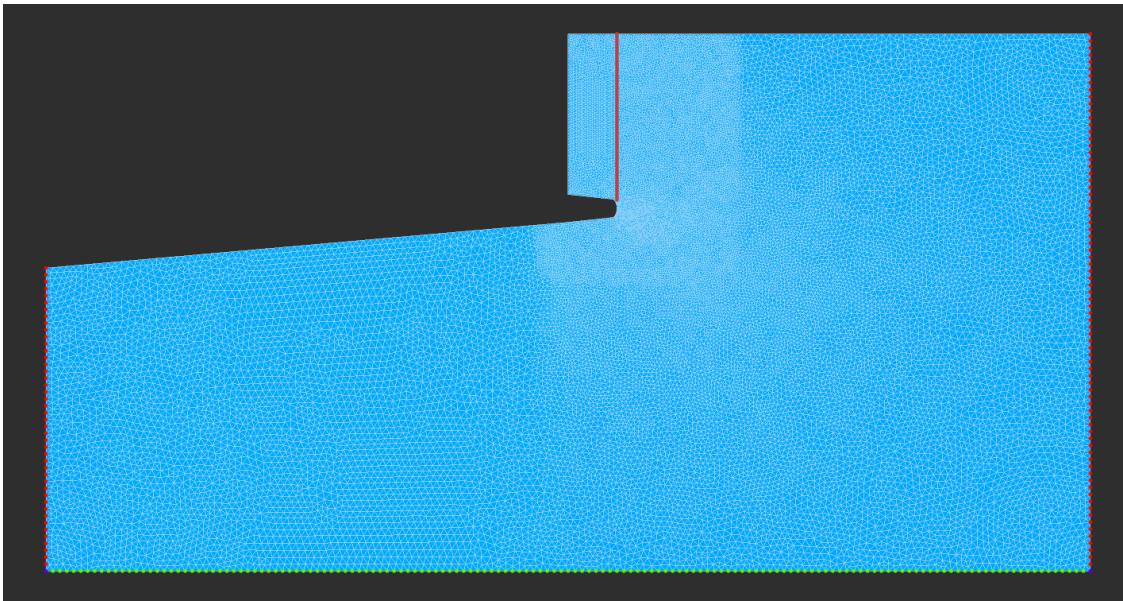
Figure 16 Final finite element mesh generated for the homogeneous vertical cliff without joint, with 10 vertical and 4-notch excavation stages model.

### 4.3.2 Homogeneous vertical cliff with joint

This section simulates the failure mechanisms of a rock cliff containing a joint with two different lengths located at a distance from the cliff face equal to the notch depth. As shown in Figure 17 and Figure 18, these models represent a 25-meter-high homogeneous cliff with a 4-meter-high, 7-meter-deep notch, a 23.75-meter-long continuous joint, and a 13.75-meter-short continuous joint located 7 meters from the cliff edge. Notably, the mode I fracture energy and mode II fracture energy of the joint is set to 1 N/m and 5 N/m, respectively, according to Zhang (2002).



*Figure 17 Final geometry of the cliff model with a 13.75m joint.*



*Figure 18 Final geometry of the cliff model with a 23.75m joint.*

The results, expressed in terms of cliff displacement, maximum shear strains, and yielded element distributions, offer valuable insight into the crack propagation process in cliffs affected by discontinuities like joints. The modeling process is outlined in Appendix D.

## 5. Results

### 5.1 FEM analyses

#### 5.1.1 Homogeneous vertical cliff without joint

##### 5.1.1.1 Numerical analyses of homogeneous vertical cliffs with a notch depth of 5 meters

The results obtained from the SSR method for cliffs of 16 different heights with a notch depth of 5 m are presented in [Figure 19](#) and [Table 2](#). The slenderness, defined as the ratio between the cliff height and the notch depth, and the cliff height are the parameters considered for the interpretation of the results.

*Table 2 Critical SRF of homogeneous cliffs with 16 different heights at a notch depth of 5 m.*

Experiment number	Cliff height	Slenderness	Result
	Hc	Hc/Ln	SRF
	[m]	[-]	[-]
1	25.00	5.00	2.42
2	22.50	4.50	2.55
3	20.00	4.00	2.70
4	17.50	3.50	2.84
5	15.00	3.00	3.00
6	12.50	2.50	3.14
7	10.00	2.00	3.21
8	9.00	1.80	3.21
9	8.50	1.70	3.19
10	7.50	1.50	3.12
11	7.00	1.40	3.07
12	6.00	1.20	2.89
13	5.00	1.00	2.60
14	4.00	0.80	2.17
15	3.50	0.70	1.86
16	3.00	0.60	1.59

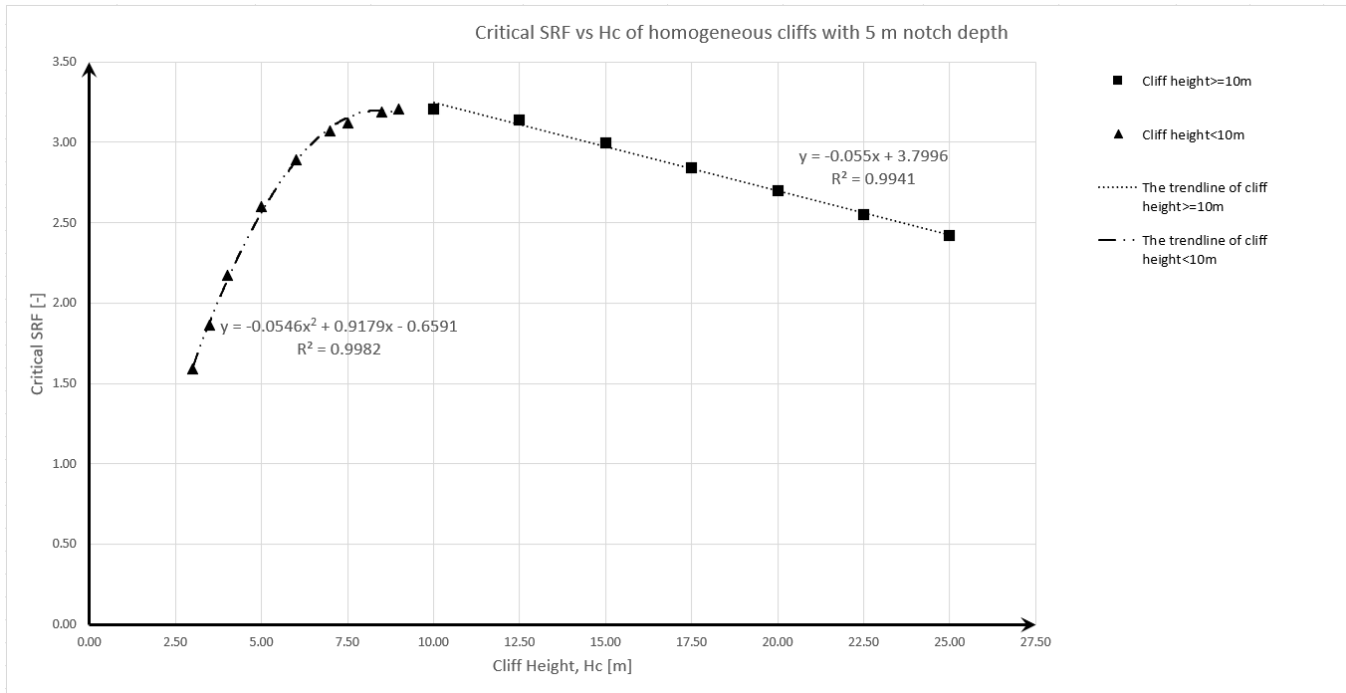


Figure 19 Correlation between the critical SRF and cliff height of homogeneous cliffs with a notch depth of 5 m.

For cliff heights below 10 meters, the results show that the critical Shear Reduction Factor (SRF) decreases significantly with the height decrease, after maintaining a constant maximum value for a while, making the cliffs more prone to instability. For example, when the cliff height decreases from 10 meters to 8.5 meters, the critical SRF fluctuates between 3.21 and 3.19. Below 8.5 meters, the critical SRF decreases from 3.19 to 1.59.

For cliff models with heights exceeding 10 meters, the fluctuations in the critical SRF are lower a bit and the trend of SRF is opposite. As the cliff height decreases from 25 to 10 meters, the critical SRF slightly increases from 2.42 to 3.21. This effect is probably due to a different failure mechanism induced on higher cliffs.

To investigate the failure mechanism of the cliff through numerical modeling, we analyzed the results in terms of maximum shear strain contours in RS2 Interpret.

Based on the results, cliff heights can be divided into two categories:

- High cliffs: cliffs heights equal to or higher than 10 m ( $H_c \geq 10$  meters)
- Low cliffs: cliffs heights lower than 10 m ( $H_c < 10$  meters)

The results show that the area with the largest shear strain on the high cliff is a clear shear band. In contrast, for low cliffs, the area of the maximum shear zone is triangular and extends broadly toward the cliff face. Therefore, the two sets of results are interpreted differently.

- **High cliffs**

Figure 20 shows the maximum shear strain for a homogeneous cliff with a height of 22.5 meters representing the typical failure mechanism of high cliffs. In this scenario, the maximum shear strain zone starts from the deepest part of the notch and extends upward to the surface. To study the effect of cliff height on cliff stability, the tilt angle of this shear zone can be measured using the measurement tools provided in RS2 Interpret. This measurement allows for a detailed analysis of how changes in cliff height influence the development and orientation of the shear strain band, thereby affecting overall cliff stability.

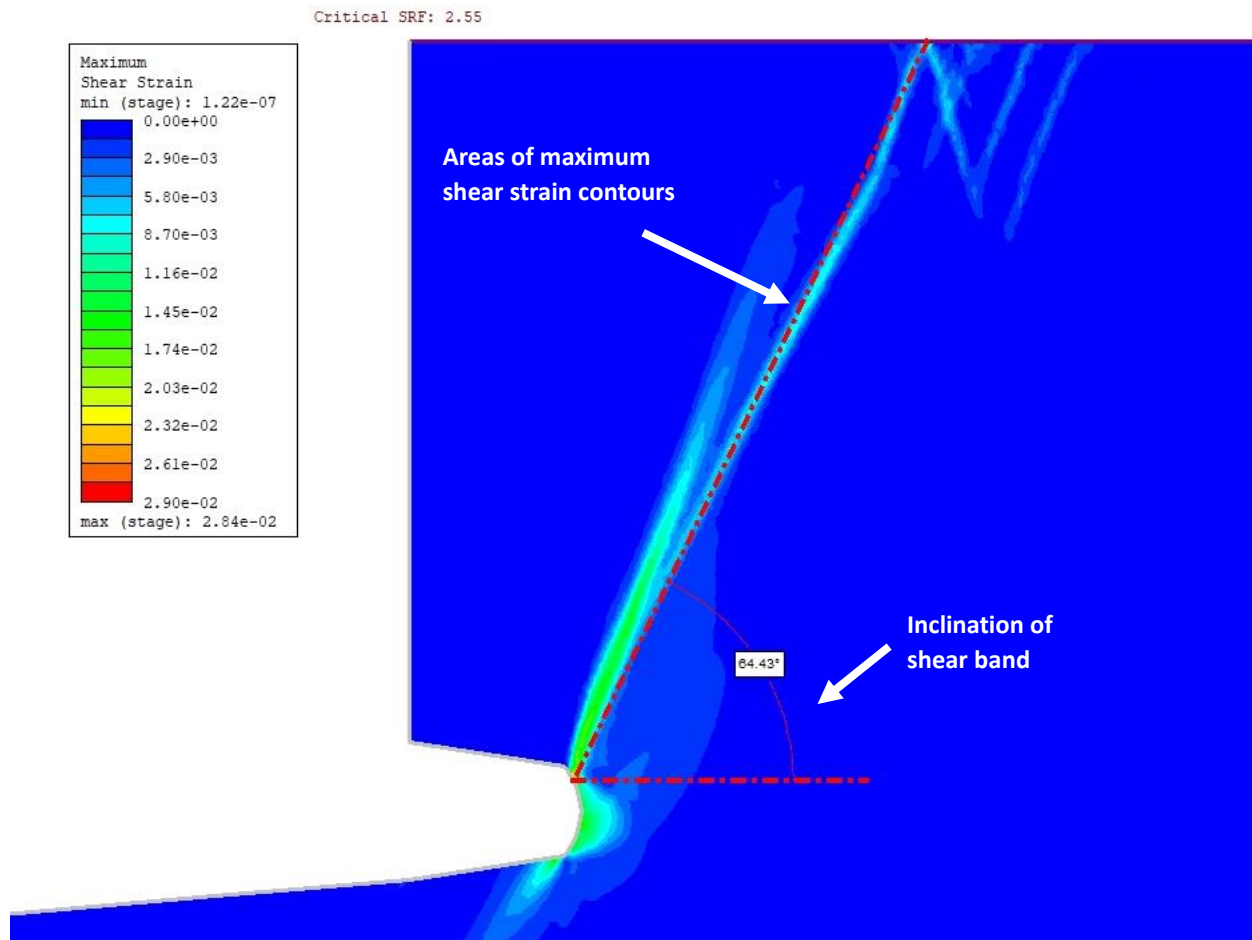


Figure 20 Failure mechanisms for high cliffs ( $H_c \geq 10$  m) with notch depth of 5 m: Maximum shear strain in a homogeneous cliff with a height of 22.5 m.

The measurement of the inclination of the maximum shear strain band was taken at the next stage beyond the critical SRF. For instance, if the critical SRF of a cliff with a height of 25 meters is 2.42, the measurement of inclination would be conducted at an SRF of 2.43. This approach is chosen as it indicates the probable failure pathway, considering that one stage beyond the critical SRF represents the maximum shear strain at which the cliff becomes unstable. Table 3 reveals that the inclination of the maximum shear strain band increases from  $62.96^\circ$  to  $69.81^\circ$  as the cliff height reduces from 25 meters to 10 meters, respectively. This indicates that as the cliff height decreases, the angle of the shear strain zone becomes steeper, affecting the stability of the cliff and the failure mechanism that progressively changes from a sliding (for higher cliffs) to a toppling failure (for lower cliffs).



Table 3 Results of the maximum shear strain at high cliffs ( $H_c \geq 10\text{ m}$ ) with 5 m notch depth.

Experiment number	Cliff height	Notch height	Notch depth	Slenderness	Result	Maximum shear strain band
	$H_c$	-	$L_n$	$H_c/L_n$	SRF	Angle
	[m]	[m]	[m]	[-]	[-]	[deg]
1	25.00	4	5	5.00	2.42	62.96
2	22.50	4	5	4.50	2.55	63.60
3	20.00	4	5	4.00	2.70	64.38
4	17.50	4	5	3.50	2.84	64.64
5	15.00	4	5	3.00	3.00	64.76
6	12.50	4	5	2.50	3.14	66.60
7	10.00	4	5	2.00	3.21	69.81

The relationship between the inclination of the maximum shear band and the cliff height can be obtained, represented in Figure 21. The results show the significant trend that the inclination of the maximum shear strain band increases as the cliff height decreases.

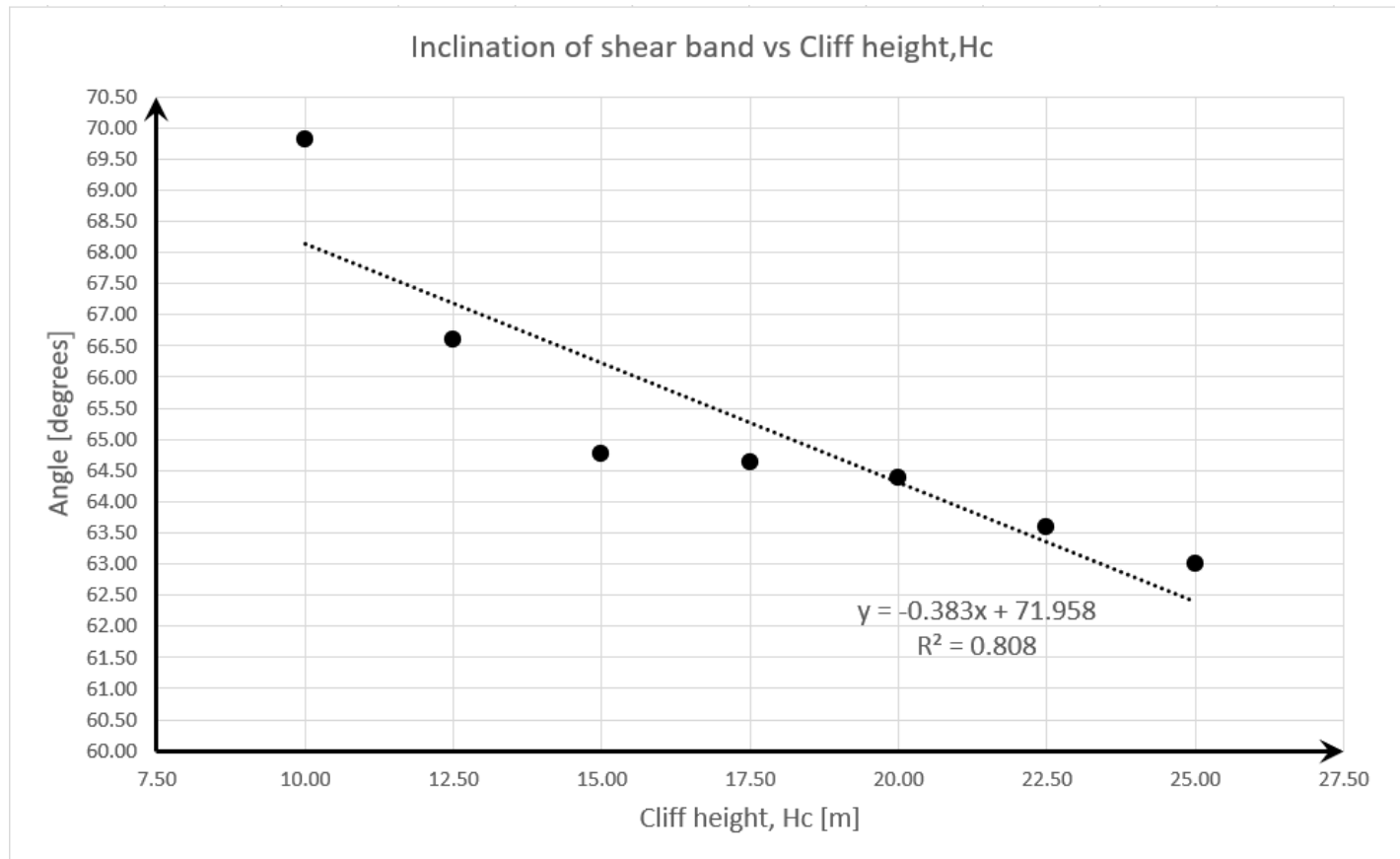


Figure 21 Correlation between the inclination of the maximum shear strain band and cliff height of the high cliffs ( $H_c \geq 10\text{ m}$ ) with 5 m notch depth.

• **Low cliffs**

The maximum shear strain pattern indicates the difference in failure mechanisms between high and low cliffs. In low cliffs less than 10 meters in height, the region of maximum shear strain originates at the upper end of the notch and then extends wider upward before reaching the top of the cliff. This progression results in the formation of concentrated areas of maximum shear strain with a triangular shape.

The extension of the shear strain on the top surface, and the angle of the triangle of maximum shear strain with the horizontal axis, starting from the end of the notch to the top surface are measured. The terms distance and angle are described below:

- L1 is the distance from the maximum shear strain area to the cliff face.
- L2 is the width of the maximum shear strain area of the top of the cliff.
- L3 is the width of the maximum shear strain zone at the tip of the notch.
- m is the angle measured from the left edge of the notch to the left edge of the area of maximum strain.
- n is the angle measured from the right edge at the end of the notch to the right edge of the maximum strain area.

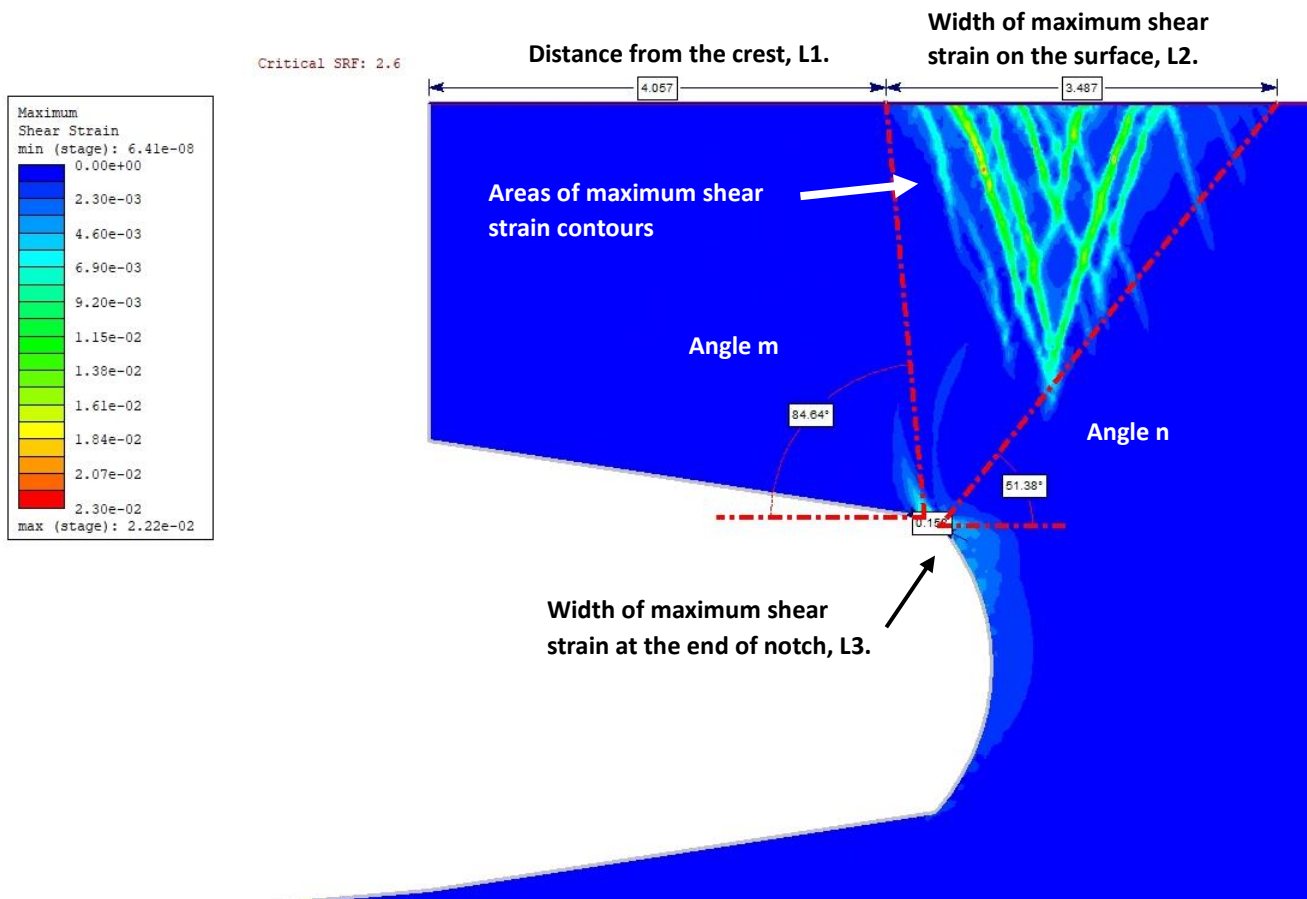


Figure 22 Failure mechanisms for low cliffs ( $H_c < 10$  meters) with notch depth of 5 meters: Maximum shear strain in a homogeneous cliff with height 5 meters.

Table 4 lists the results for low cliff measurements with different cliff heights and different slenderness.

Table 4 Results of the maximum shear strain at low cliffs ( $H_c < 10$  meters) with 5 meters notch depth.

Experiment number	Cliff height	Slenderness	Results	Shear band pattern at low-height cliffs				
	$H_c$	$H_c/L_n$	SRF	L1	L2	L3	m	n
	[m]	[-]	[-]	[m]	[m]	[m]	[deg]	[deg]
8	9.00	1.80	3.21	6.252	4.983	0.931	103.37	55.08
9	8.50	1.70	3.19	5.766	4.715	0.735	100.50	54.19
10	7.50	1.50	3.12	5.144	4.631	0.705	96.71	52.76
11	7.00	1.40	3.07	4.981	4.306	0.497	95.50	53.26
12	6.00	1.20	2.89	4.516	3.958	0.299	91.08	51.96
13	5.00	1.00	2.60	4.057	3.487	0.158	84.64	51.38
14	4.00	0.80	2.17	3.782	3.089	0.147	77.60	49.08
15	3.50	0.70	1.86	3.556	3.068	0.166	70.05	47.02
16	3.00	0.60	1.59	3.496	2.598	0.183	63.67	46.98

The values of L1 and L2 follow a similar trend, decreasing from 6.252 meters and 4.983 meters to 3.496 meters and 2.598 meters, respectively, as the cliff height drops from 9 meters to 3 meters. Figure 23-Figure 25 demonstrates a strong graphical correlation between the values of L1 and L2 with the height of the cliff. As the height of the cliff increases, both L1 and L2 proportionally increase. Furthermore, the values of L3 increase from 0.183 meters to 0.931 meters with the cliff height increasing.

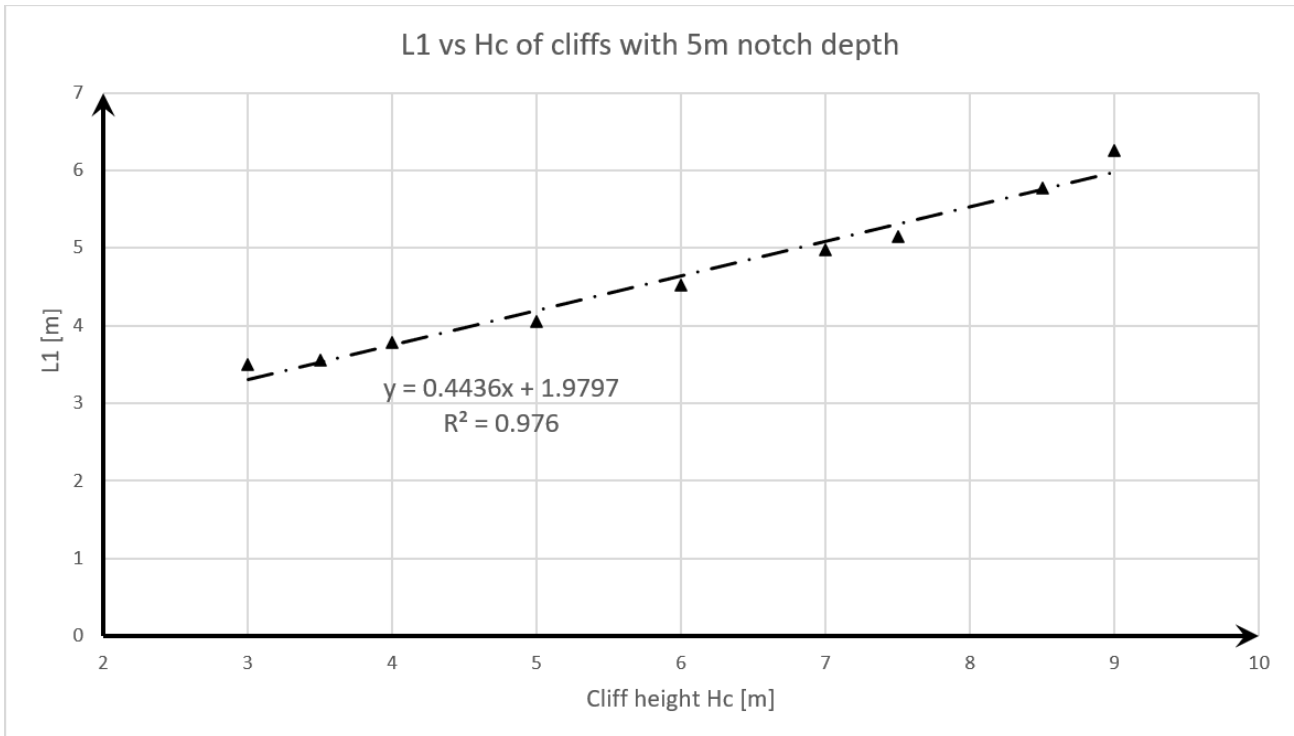


Figure 23 Correlation between L1 and cliff heights of low cliffs with 5 meters notch depth.

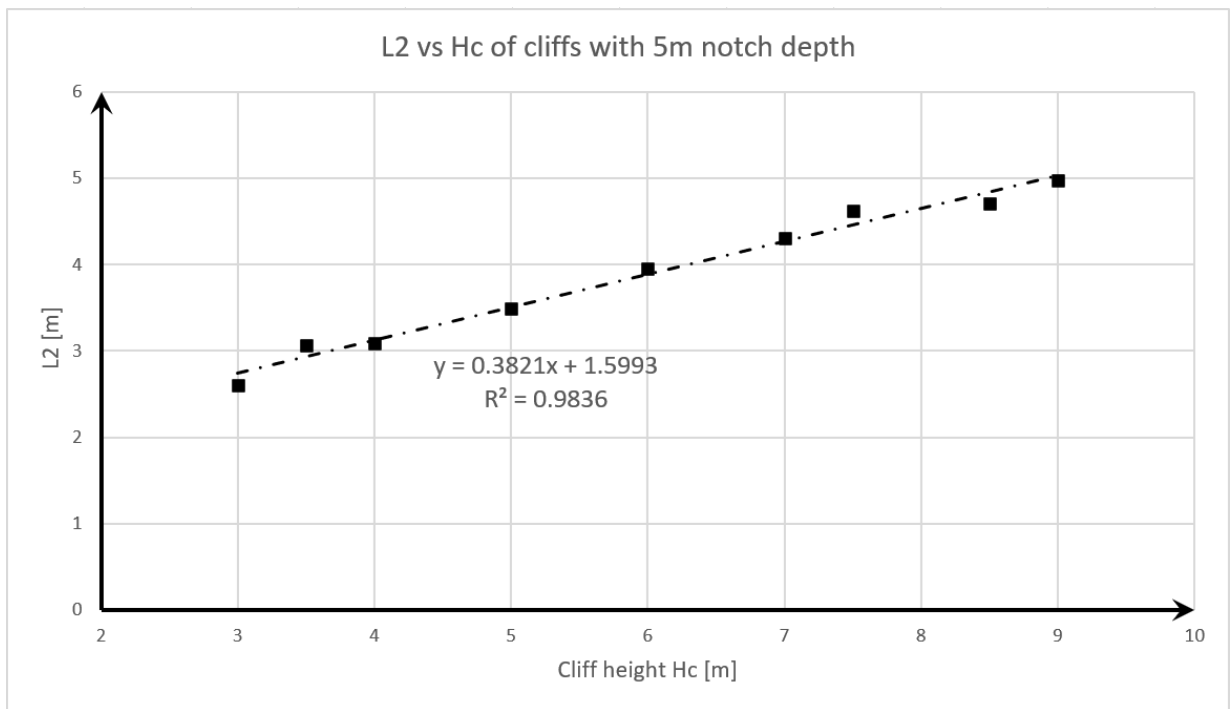


Figure 24 Correlation between L2 and cliff heights of low cliffs with 5 meters notch depth.

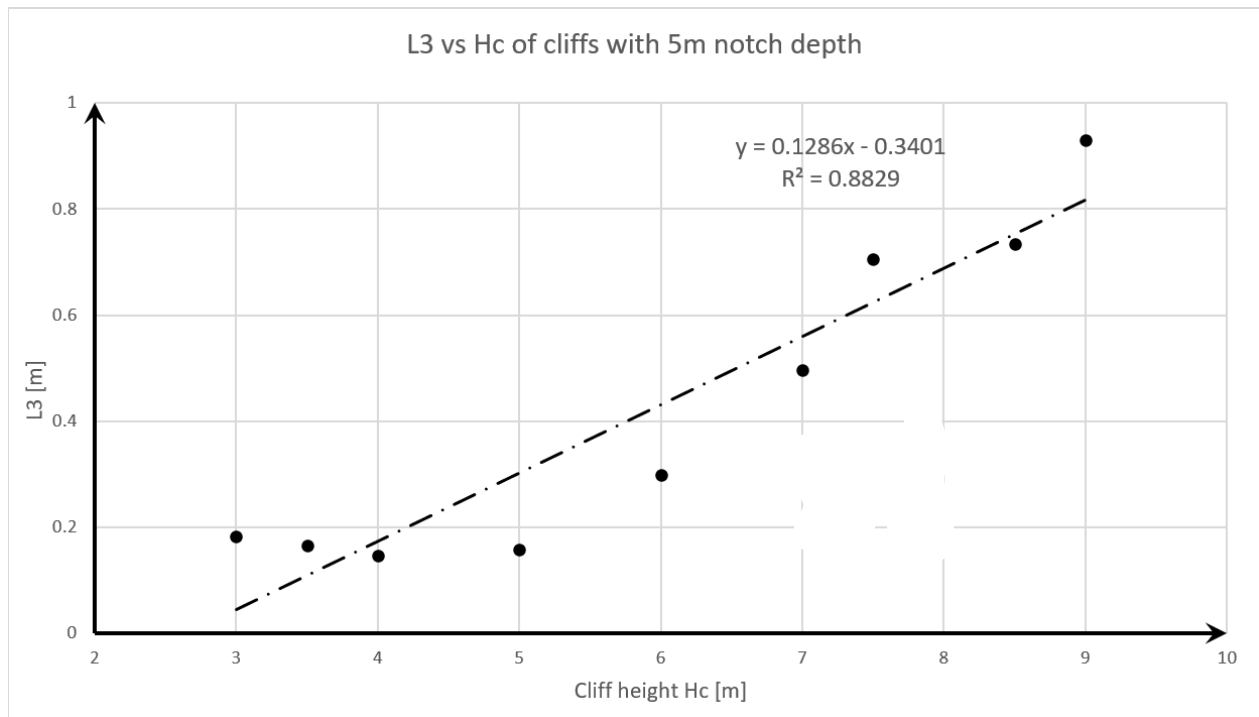


Figure 25 Correlation between L3 and cliff heights of low cliffs with 5 meters notch depth.

As can be seen from [Figure 26](#), there is a significant correlation between cliff height and parameters  $m$ , and  $n$ . The value of angle  $m$  tends to increase with increasing cliff height. Meanwhile, the values of angle  $n$  increase within the range of  $46.98^\circ$  to  $55.08^\circ$ .

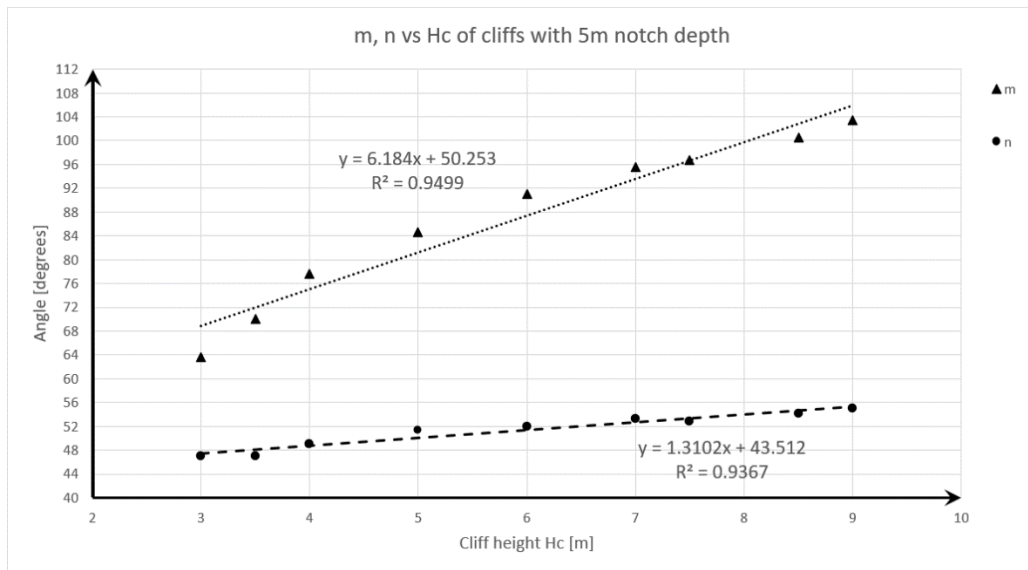


Figure 26 Correlation between *m*, *n*, and cliff heights of low cliffs with 5 meters notch depth.

### 5.1.1.2 Numerical analysis of homogeneous vertical cliffs with a notch depth of 3 meters

Figure 27 and Table 5 show the results obtained by the SSR method for fifteen cliffs of different heights with a notch depth of 3 meters. The critical SRF increased from 3.91 to 5.30 values in the cliff height range of 2.5 to 4 meters. In contrast, the critical SRF values remain about 5.42 and 5.43 when the cliff height increases from 4 meters to 6 meters, indicating greater stability in this height range. Above 6 meters, as the cliff height increases, the critical SRF value decreases gradually faster, indicating a sharp decrease in stability. This highlights that lower cliffs tend to have greater stability.

Table 5 Critical SRF of homogeneous cliffs with 15 different heights at a notch depth of 3 meters.

Experiment number	*Depth of the notch 3m			**Depth of the notch 3m		
	Cliff height	Slenderness	Results	Cliff height	Slenderness	Results
	Hc [m]	Hc/Ln [-]	SRF [-]	Hc [m]	Hc/Ln [-]	SRF [-]
1	25.00	8.33	2.91	25.00	8.33	2.86
2	22.50	7.50	3.10	22.50	7.50	3.05
3	20.00	6.67	3.33	20.00	6.67	3.27
4	17.50	5.83	3.60	17.50	5.83	3.53
5	15.00	5.00	3.94	15.00	5.00	3.83
6	12.50	4.17	4.34	12.50	4.17	4.20
7	10.00	3.33	4.82	10.00	3.33	4.65
8	8.50	2.83	5.17	8.50	2.83	4.96
9	7.50	2.50	5.39	7.50	2.50	5.17
10	7.00	2.33	5.48	7.00	2.33	5.27
11	6.00	2.00	5.71	6.00	2.00	5.43
12	5.00	1.67	5.75	5.00	1.67	5.42
13	4.00	1.33	5.75	4.00	1.33	5.30
14	3.00	1.00	4.87	3.00	1.00	4.54
15	2.50	0.83	5.27	2.50	0.83	3.91

\*: The data is from Inkate (2023). \*\*: The data is from this study.

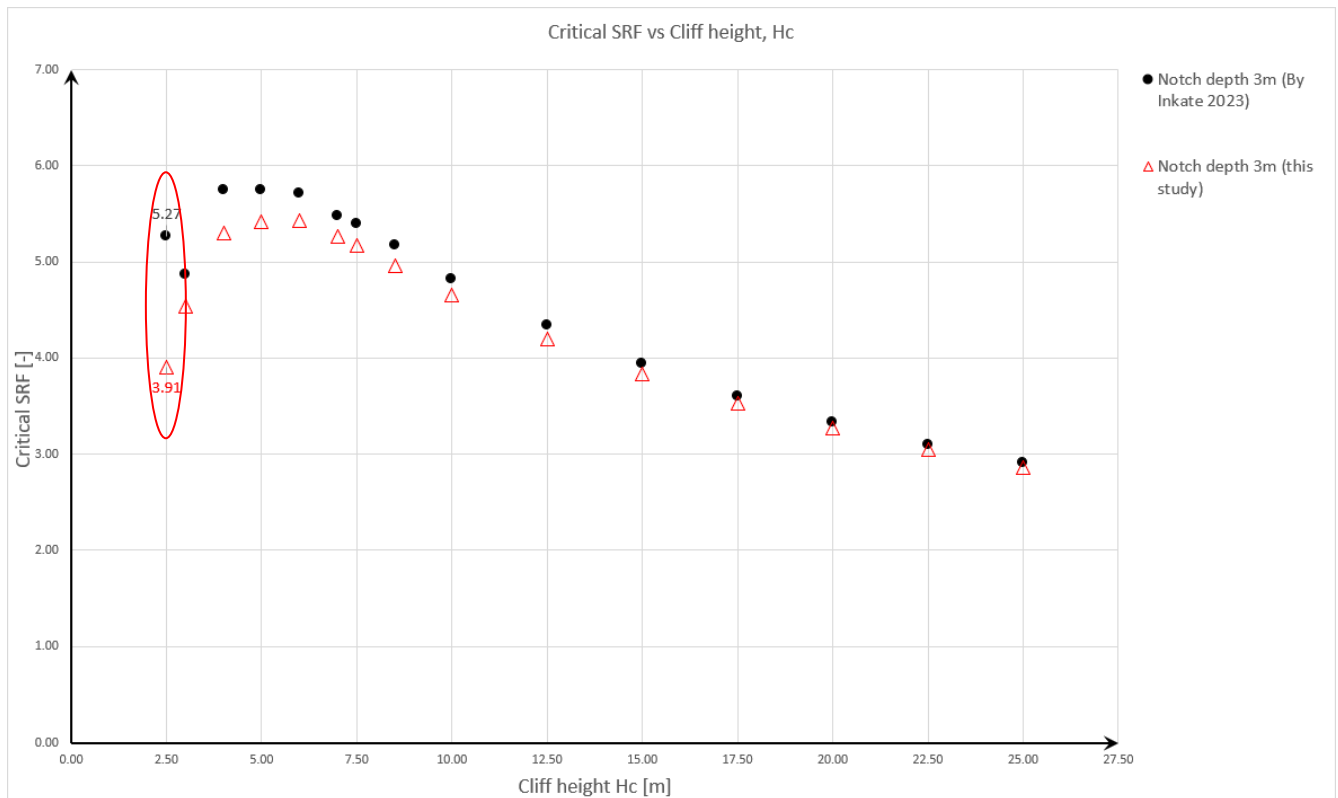


Figure 27 Comparison of the Inkate's (2023) results with this study's results: correlation between the critical SRF and cliff height of homogeneous cliffs with a notch depth of 3 meters.

Compare Inkate's (2023) results with the results of this study. Except for the SRF values of cliffs with a height of 2.5 meters, which are very different, the critical SRF values of cliffs with other heights are similar.

Based on the results in terms of shear strain, cliff heights can be divided into two categories:

- High cliffs: cliffs heights equal to or higher than 5 meters ( $H_c \geq 5$  meters)
- Low cliffs: cliffs heights lower than 5 meters ( $H_c < 5$  meters)

The results show the maximum shear strain area on the high cliff is mainly represented by a shear band. In contrast, for low cliffs, the area of the maximum shear zone is triangular and extends broadly over the top surface and notch end. Therefore, the two sets of results require different interpretations, similar to the previous analysis results.

### • High cliffs

The slope of the linear band of maximum shear strain is measured at the next stage beyond the critical SRF, as shown in Table 6 and Figure 28, allowing the development of the maximum shear strain at failure to be studied.

Table 6 Comparison the Inkate's (2023) results with this study's results of maximum shear strain band for high cliffs with a notch depth of 3 meters.

Experiment number	Cliff height	Slenderness	*Results	*Maximum shear strain band		**Results	**Maximum shear strain band	
	Hc		SRF	Failure	Angle	SRF	Failure SRF	Angle
	[m]	[-]	[-]	SRF	[deg]	[-]	[-]	[deg]
1	25.00	8.33	2.91	2.92	56	2.86	2.87	58.29
2	22.50	7.50	3.10	3.11	61	3.05	3.06	59.63
3	20.00	6.67	3.33	3.34	64	3.27	3.28	60.43
4	17.50	5.83	3.60	3.61	60	3.53	3.54	59.21
5	15.00	5.00	3.94	3.95	57	3.83	3.84	60.28
6	12.50	4.17	4.34	4.35	61	4.20	4.21	61.03
7	10.00	3.33	4.82	4.83	64	4.65	4.66	63.35
8	8.50	2.83	5.17	5.18	61	4.96	4.97	63.64
9	7.50	2.50	5.39	5.40	61	5.17	5.18	64.40
10	7.00	2.33	5.48	5.49	62	5.27	5.28	66.94
11	6.00	2.00	5.71	5.72	67	5.43	5.44	69.11
12	5.00	1.67	5.75	5.76	69	5.42	5.43	70.76

\*: The data is from Inkate (2023). \*\*: The data is from this study.

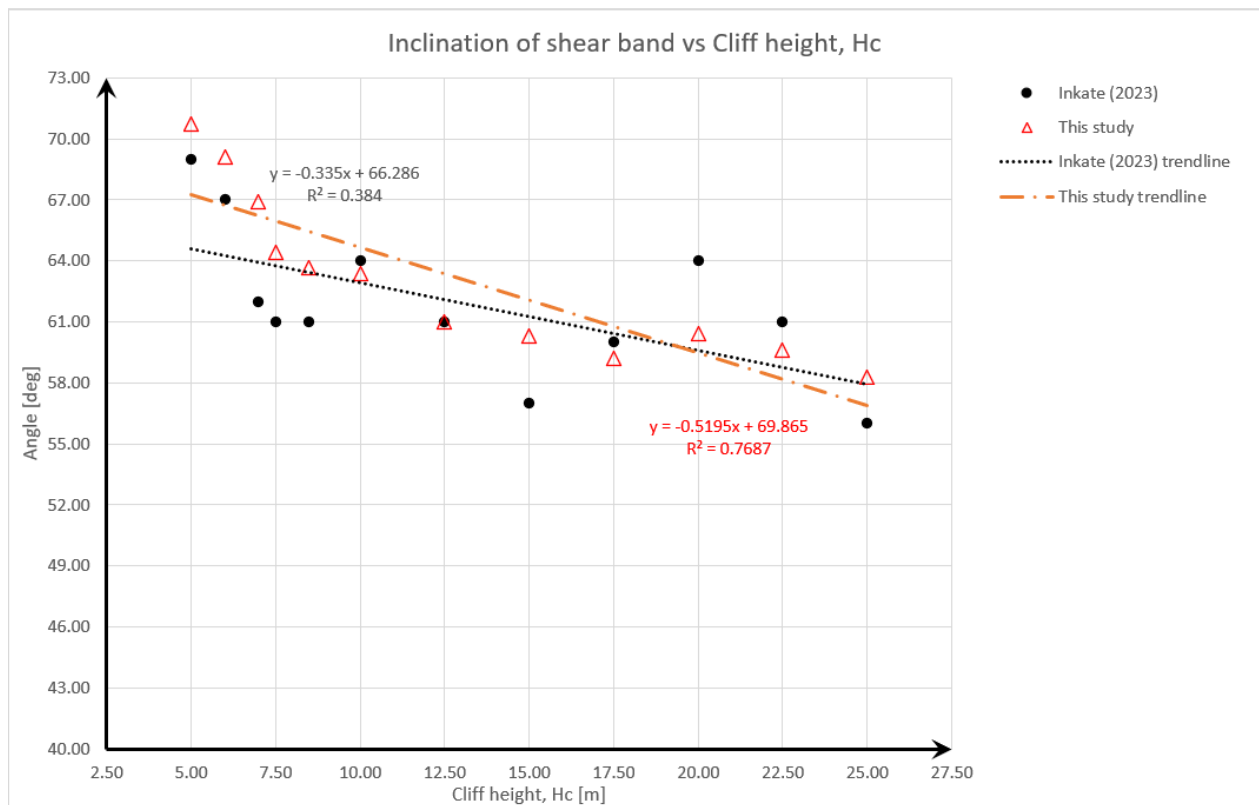


Figure 28 Comparison of the Inkate (2023) results with this study's results of correlation between the inclination of maximum shear strain band and cliff with notch depth of 3 meters: High cliffs.

The study concluded that the slope of the maximum shear strain area decreases with increasing cliff height. This trend is consistent with Inkate's (2023) conclusion.

• **Low cliffs**

Figure 29-Figure 31 shows that distances L1, L2, and L3 have a similar trend and decrease as the cliff height decreases from 4 meters to 2.5 meters. Likewise, Figure 32 and Figure 33 present the angles m and n decrease with decreasing cliff height. In summary, for the lower cliffs, all parameters related to the maximum shear strain zone increase with increasing cliff height. This result is consistent with the conclusion of Inkate (2023).

Table 7 Comparison the Inkate's (2023) results with this study's results of maximum shear strain band for low cliffs with a notch depth of 3 meters.

Experiment number	Cliff height	Slenderness	*Results	*Shear band pattern at low heights					**Results	**Shear band pattern at low heights				
	Hc	Hc/Ln	SRF	L1	L2	L3	m	n	SRF	L1	L2	L3	m	n
	[m]	[-]	[-]	[m]	[m]	[m]	[deg]	[deg]	[-]	[m]	[m]	[m]	[deg]	[deg]
13	4	1.33	5.75	2.81	2.28	1.30	104	60	5.30	2.786	2.602	0.730	92.72	52.42
14	3	1.00	4.87	2.10	1.76	0.81	94	59	4.54	2.134	2.012	0.336	81.19	51.58
15	2.5	0.83	5.27	2.15	1.83	0.68	96	46	3.91	2.026	1.520	0.087	70.64	50.02

\*: The data is from Inkate (2023). \*\*: The data is from this study.

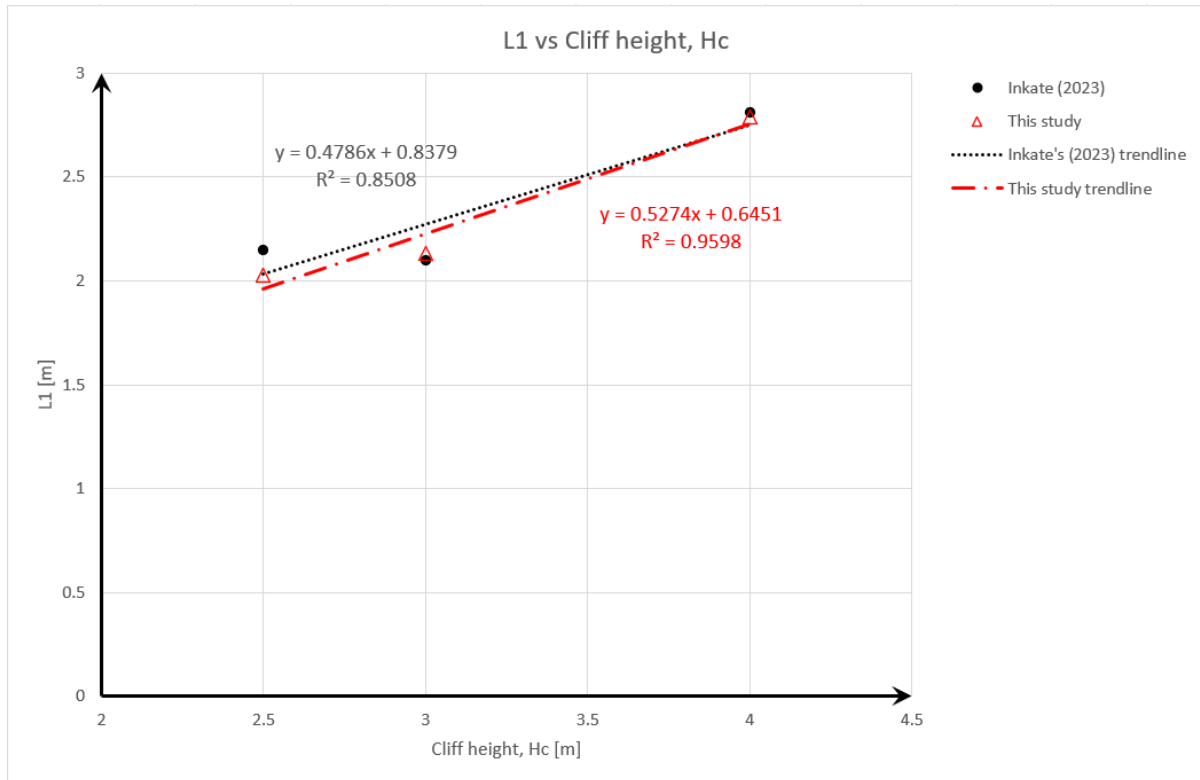


Figure 29 Comparison the Inkate's (2023) results with this study's results of correlation between L1 and cliff heights of low cliffs with 3 meters notch depth.



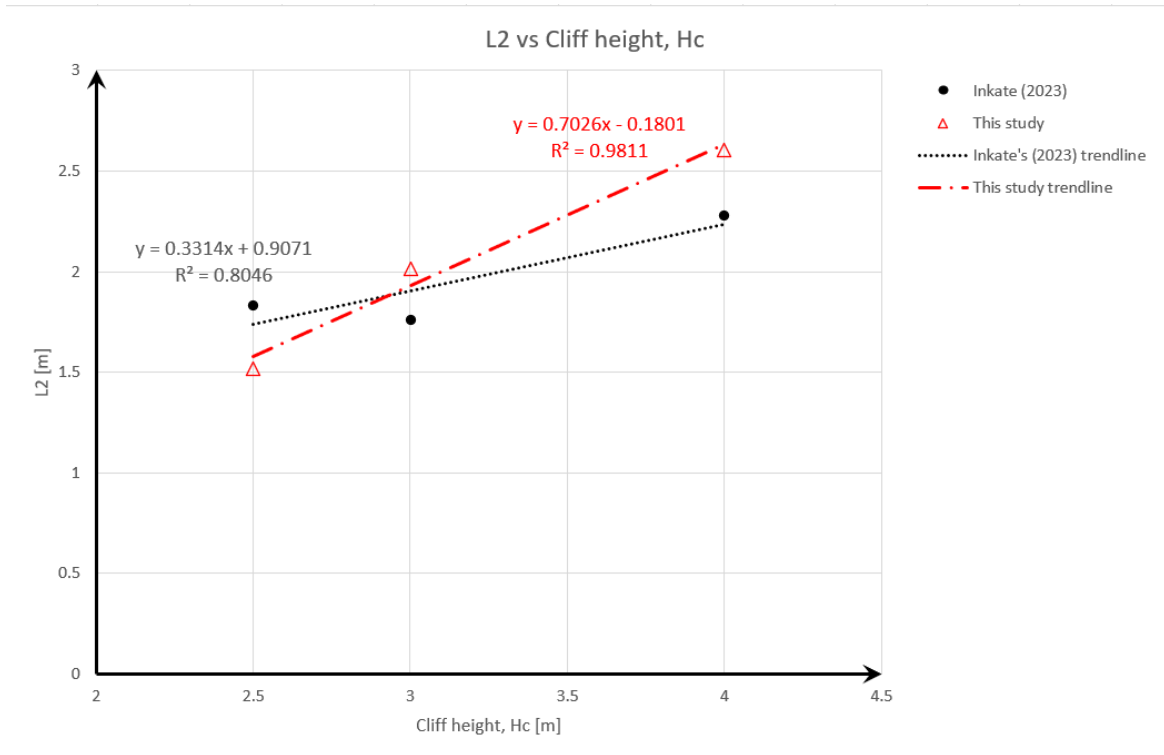


Figure 30 Comparison the Inkate's (2023) results with this study's results of correlation between L2 and cliff heights of low cliffs with 3 meters notch depth.

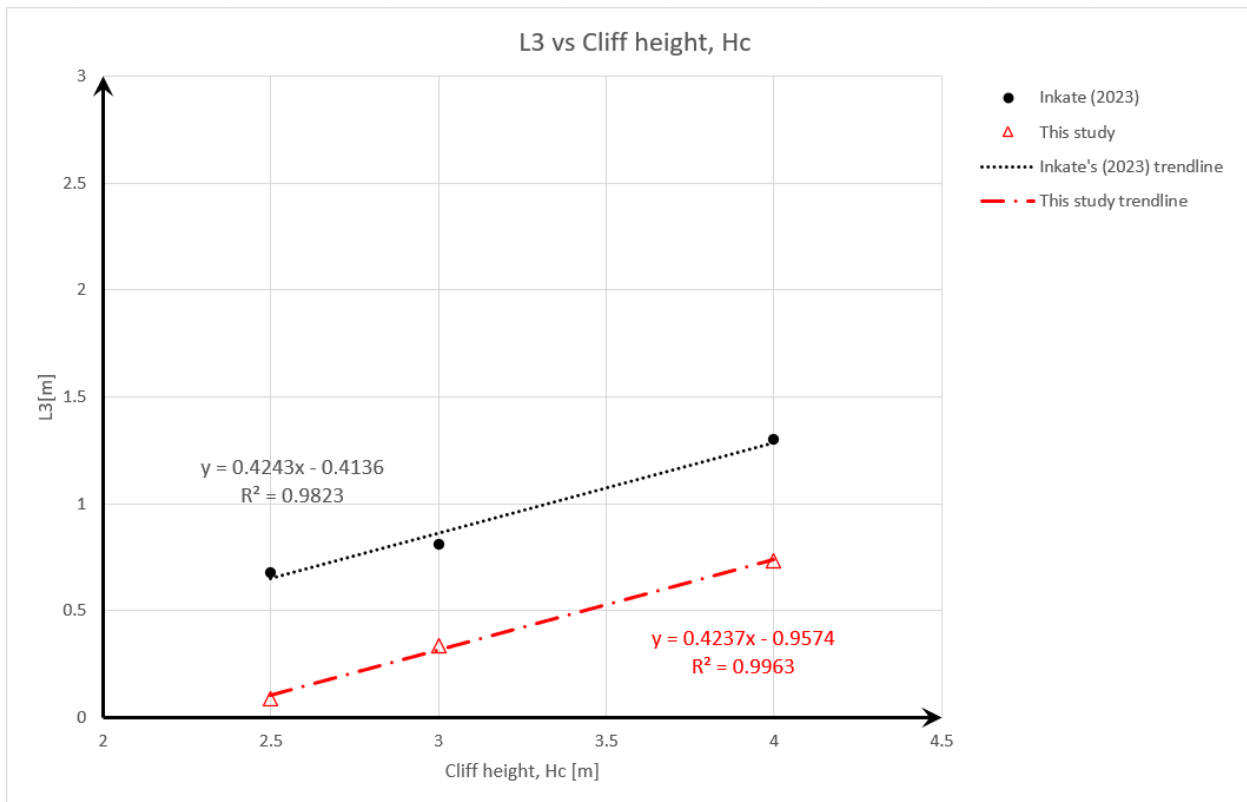


Figure 31 Comparison the Inkate's (2023) results with this study's results of correlation between L3 and cliff heights of low cliffs with 3 meters notch depth.

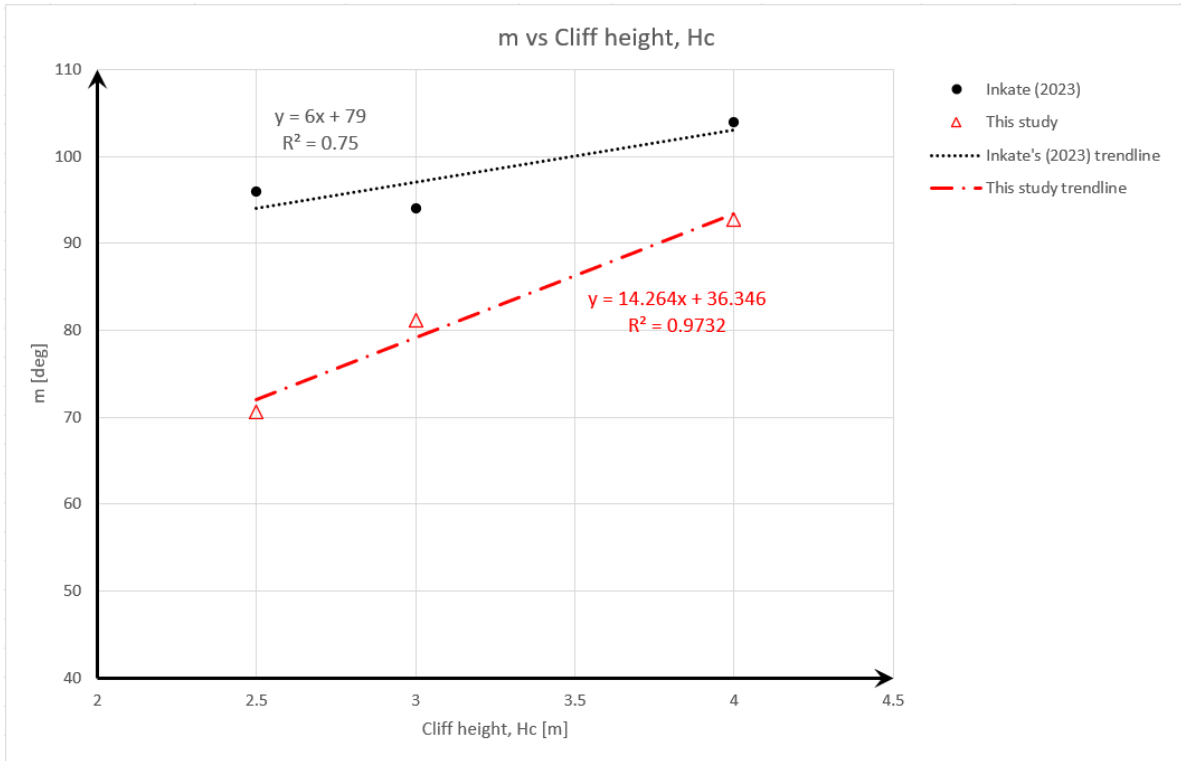


Figure 32 Comparison the Inkate's (2023) results with this study's results of correlation between  $m$  and cliff heights of low cliffs with 3 meters notch depth.

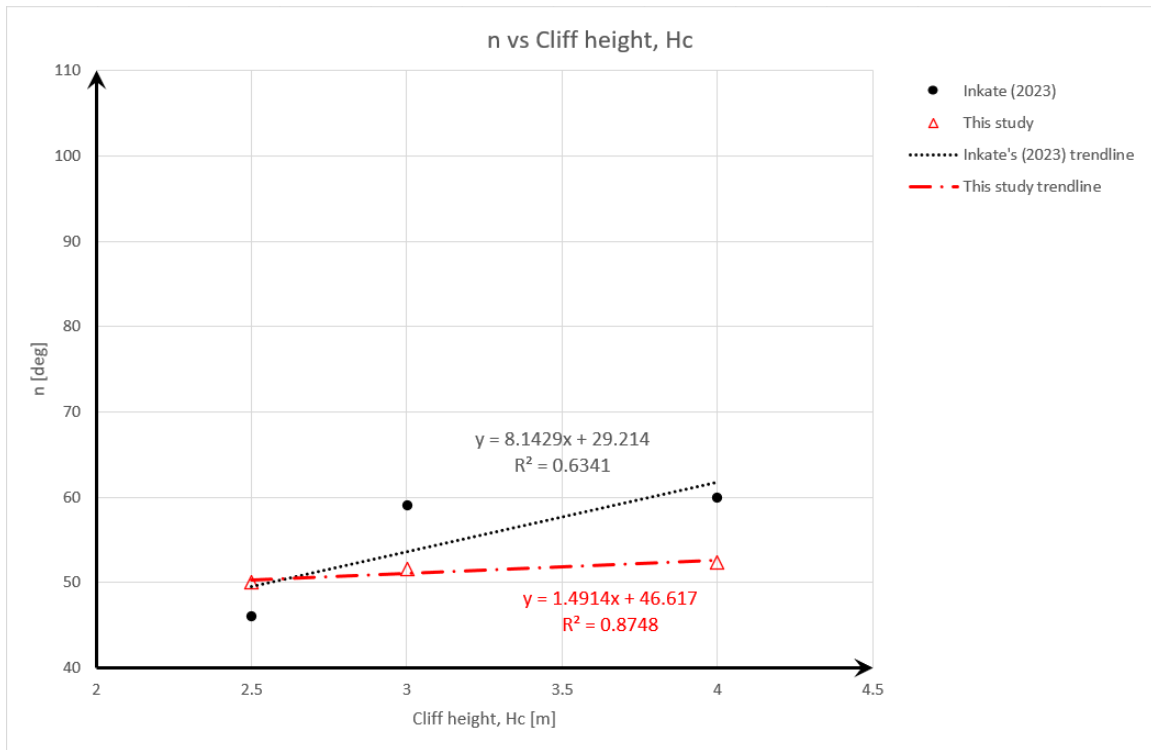


Figure 33 Comparison of Inkate's (2023) results with this study's correlation between  $n$  and cliff heights of low cliffs with 3 meters notch depth.

### 5.1.1.3 Correlation between slenderness ratio and critical SRF

The results by Inkate (2023) and this study's results of homogeneous cliffs with varying notch depths are collected in Table 8, which details cliff height, slenderness ratio, and critical SRF values for four constant notch depths: 10 meters, 7 meters, 5 meters, and 3 meters. In Figure 34, the results demonstrate noticeable trends for cliffs with varying notch depths.

Table 8 Slenderness and critical SRF of homogeneous cliffs with notch depth of 10 meters, 7 meters, 3 meters (from Povanat Inkate 2023) and 5 meters (This study)

*Depth of the notch 10m			*Depth of the notch 7m			**Depth of the notch 5m			**Depth of the notch 3m		
Hc [m]	Hc/Ln [-]	SRF	Hc [m]	Hc/Ln [-]	SRF	Hc [m]	Hc/Ln [-]	SRF	Hc [m]	Hc/Ln [-]	SRF
25.00	2.50	1.61	25.00	3.57	2.12	25.00	5.00	2.42	25.00	8.33	2.86
22.50	2.25	1.63	22.50	3.21	2.13	22.50	4.50	2.55	22.50	7.50	3.05
20.00	2.00	1.63	20.00	2.86	2.21	20.00	4.00	2.70	20.00	6.67	3.27
17.50	1.75	1.61	17.50	2.50	2.27	17.50	3.50	2.84	17.50	5.83	3.53
15.00	1.50	1.53	15.00	2.14	2.32	15.00	3.00	3.00	15.00	5.00	3.83
12.50	1.25	1.48	12.50	1.79	2.31	12.50	2.50	3.14	12.50	4.17	4.20
10.00	1.00	1.34	10.00	1.43	2.24	10.00	2.00	3.21	10.00	3.33	4.65
9.00	0.90	1.17	9.00	1.29	2.18	9.00	1.80	3.21	8.50	2.83	4.96
8.50	0.85	1.10	8.50	1.21	2.11	8.50	1.70	3.19	7.50	2.50	5.17
7.50	0.75	0.86	7.50	1.07	2.00	7.50	1.50	3.12	7.00	2.33	5.27
7.00	0.70	0.67	7.00	1.00	1.93	7.00	1.40	3.07	6.00	2.00	5.43
6.00	0.60	-	6.00	0.86	1.75	6.00	1.20	2.89	5.00	1.67	5.42
5.00	0.50	-	5.00	0.71	1.49	5.00	1.00	2.60	4.00	1.33	5.30
			4.00	0.57	1.17	4.00	0.80	2.17	3.00	1.00	4.54
			3.50	0.50	0.97	3.50	0.70	1.86	2.50	0.83	3.91
			3.00	0.43	-	3.00	0.60	1.59			

\*: The data is from Inkate (2023). \*\*: The data is from this study.

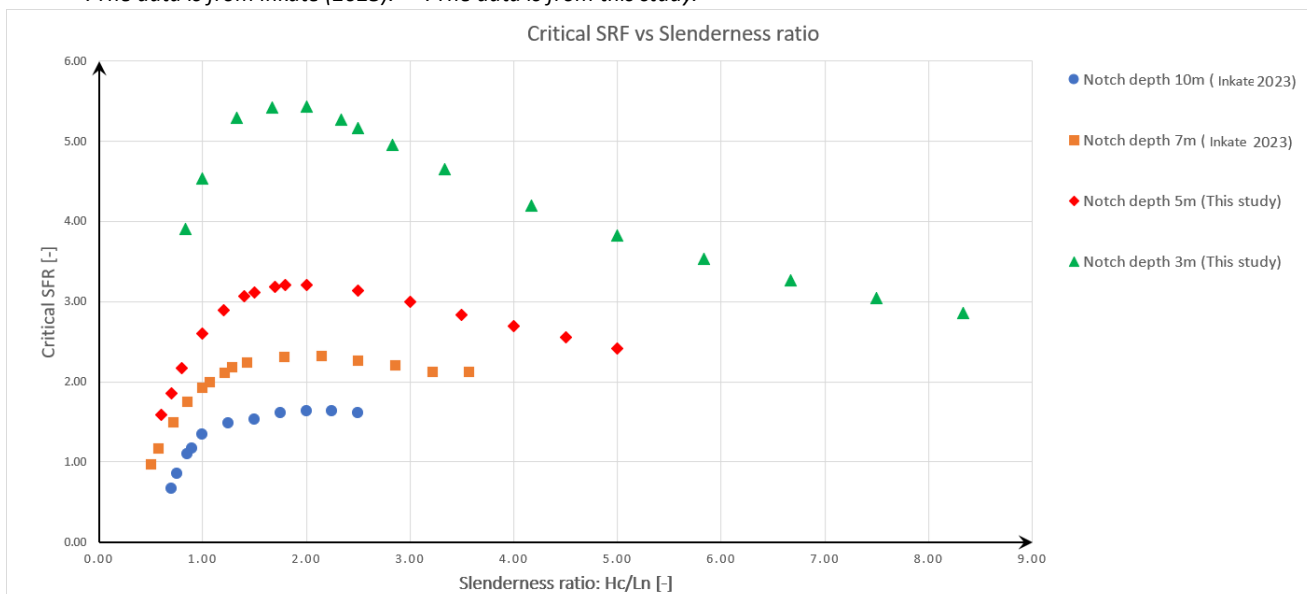


Figure 34 Correlation between critical SRF and slenderness ratio of cliffs with notch depth of 10 meters, 7 meters, 5 meters, and 3 meters.

The results for cliffs with 5-meter deep notches have similar trends to those reported by Inkate (2023) for 10- and 7-meter deep notches. When the slenderness ratio is below 1.70, the critical SRF gradually increases with the slenderness ratio and varies from 1.59 (notch=10m) to 3.19 (notch=5m), and then reaches peak stability when the slenderness ratio is between 1.70 and 2.00. Beyond this range, as the slenderness ratio continues to increase, the SRF of the cliff gradually decreases.

The results for the cliff with a 3-meter deep notch show a significantly higher critical SRF value compared to cliffs with deeper notches. Initially, as the slenderness ratio increases from 0.83 to 2, the critical SRF rises from 3.91 to 5.43. However, beyond this point, as the slenderness ratio rises from 2 to 8.33, the critical SRF value decreases from 5.43 to 2.86. This trend differs slightly from the results for the 7-meter and 10-meter notches reported by Inkate (2023) and from the results of the 5-meter deep notch in this study. Specifically, the cliff with a 3-meter deep notch reaches its peak stability at the slenderness ratio of 2, after which stability rapidly decreases. In contrast, cliffs with 10-meter and 7-meter notches maintain stability for a period after reaching their maximum SRF value.

In summary, the trend of cliff stability for the 5-meter deep notch in this study is consistent with Inkate's (2023) conclusions for the 7-meter and 10-meter deep notches and confirms that at slenderness ratios of 1.7 to 2, the failure mechanism changes from toppling to sliding.

### 5.1.2 Homogeneous inclined cliff without joint

A 70° inclined cliff made of homogeneous material, 4 different notch depths, and 25 meters height was analyzed using RS2 software. These results are shown in Table 9 and Figure 35.

Table 9 Comparison of critical SRF for vertical cliffs and inclination cliffs

Experiment number	Cliff height	Notch depth	Vertical cliff (angle = 90°)	Inclination cliff (angle = 70°)
	Hc	Ln	SRF	SRF
	[m]	[m]	[-]	[-]
1	25	3	2.86	3.74
2	25	5	2.42	3.32
3	25	7	2.12*	2.84
4	25	10	1.61*	2.21

\*: The data is from Inkate (2023)

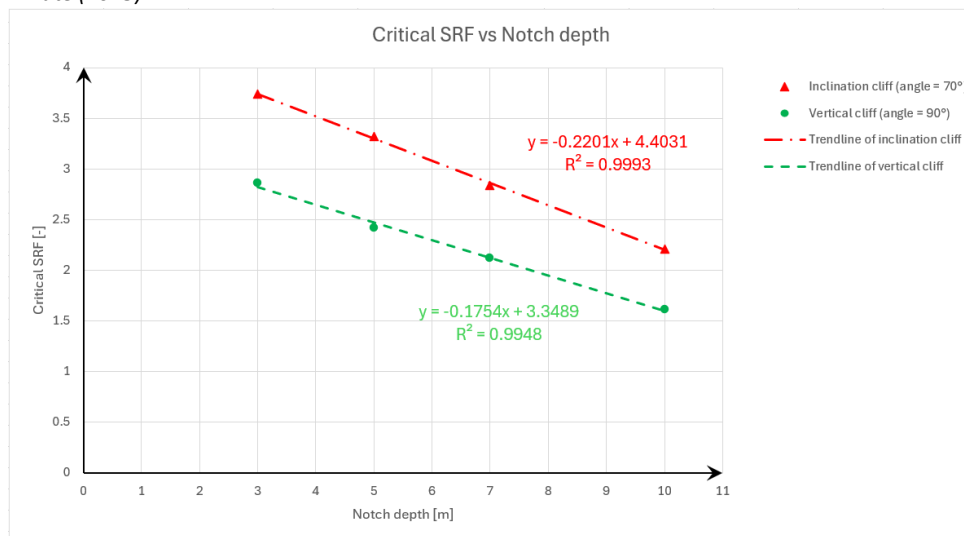


Figure 35 Correlation between critical SRF and notch depth for vertical and inclined cliffs.

The results indicate that as the notch depth increases, the critical SRF values for both vertical and inclined cliffs decrease linearly. It is noteworthy that the critical SRF values for inclined cliffs are consistently higher than those for vertical cliffs due to the lower weight of the overhang. This suggests that, regardless of the notch depth, the stability of inclined cliffs is superior to that of vertical cliffs for a given cliff height.

The slope of the maximum shear strain band is measured at the next stage beyond the critical SRF, as shown in Table 10 and Figure 36, to study the development of the maximum shear strain at failure.

Table 10 Comparison of the maximum shear strain band for vertical and inclined cliffs.

Experiment number	Cliff height	Notch depth	Vertical cliff (angle = 90°)			Inclination cliff (angle = 70°)		
			Results	Maximum shear strain band		Results	Maximum shear strain band	
	Hc	Ln	SRF	Failure SRF	Angle	SRF	Failure SRF	Angle
	[m]	[m]	[-]	[-]	[deg]	[-]	[-]	[deg]
1	25	3	2.86	2.87	58.29	3.74	3.75	50.23
2	25	5	2.42	2.43	62.96	3.32	3.33	53.28
3	25	7	2.12*	2.13*	63.00*	2.84	2.85	58.65
4	25	10	1.61*	1.62*	65.96*	2.21	2.22	65.45

\*: The data is from Inkate (2023)

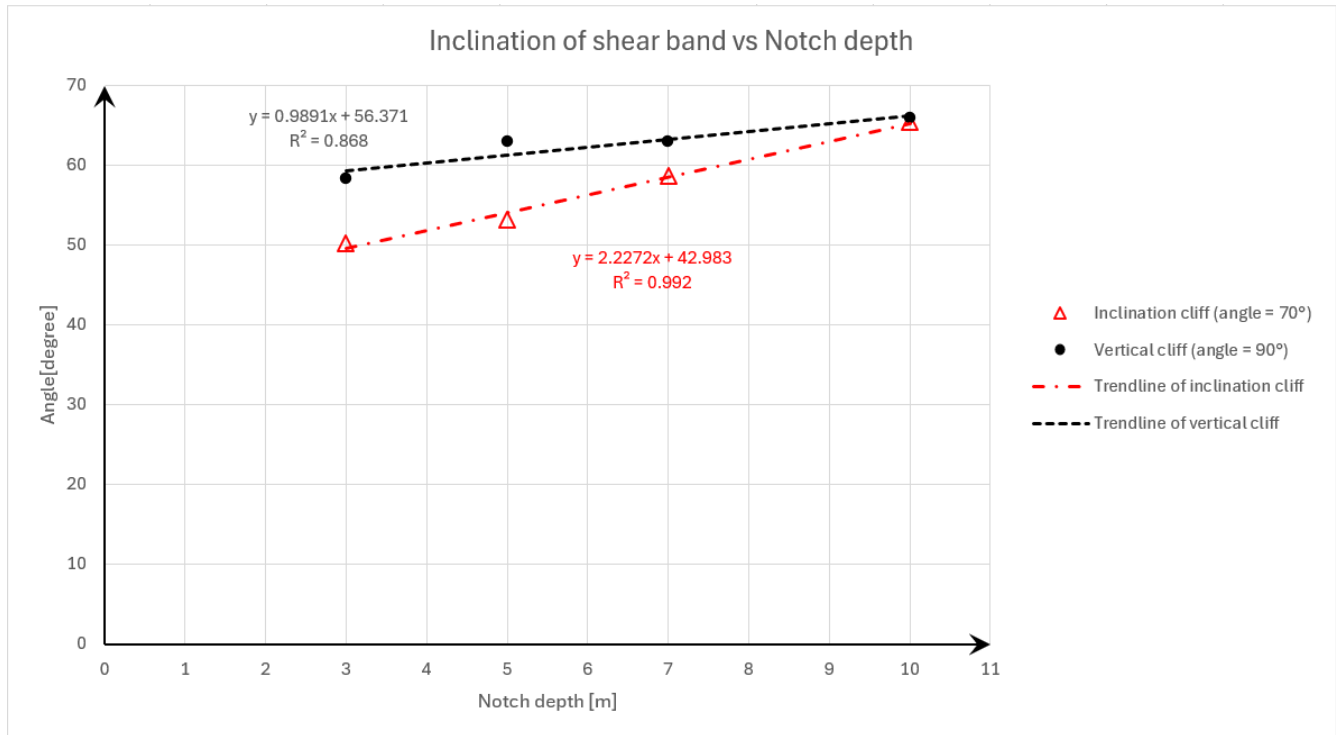


Figure 36 Correlation between Inclination of the shear band and notch depth for vertical and inclination cliffs.

Figure 36 illustrates that the maximum shear strain inclination increases with the depth of the notch. However, the maximum shear strain inclination for vertical cliffs is always higher than that for inclined cliffs. This implies that as the notch depth increases, vertical cliffs exhibit steeper maximum shear strain bands compared to inclined cliffs, thereby highlighting the relative stability advantage of inclined cliffs over vertical cliffs.

### 5.1.3 Homogeneous vertical cliff with joint

This section examines how the presence of discontinuities in the rock cliff impacts cliff failure mechanisms. A vertical joint was included in a cliff with a height of 25 meters and a notch of 7 meters deep to simulate the Punta Ferruccio conglomerate cliff. The conglomerate material and joint parameters were obtained by Calista et al. (2019), as shown in Table 11. In addition, in the back analysis, the tensile strength, cohesion, and friction angle of the joint is estimated according to Equation (1), to account for the presence of (unknown) rock bridges.

Table 11 The strength parameters of joint

Strength parameter for joint	Value and physical units
Cohesion ( $j_c'$ )	1.00E+04 Pa
Friction angle ( $j\phi'$ )	30°
Normal stiffness ( $j k_n$ )	1.20E+08 Pa/m
Shear stiffness ( $j k_s$ )	1.20E+08 Pa/m
Tensile strength ( $\sigma_t^j$ )	3.80E+04 Pa

After the parametric analysis of the joint, The study focuses on the influence of joint lengths of 23.75 meters and 18.75 meters at different horizontal positions on the critical SRF of the cliff and observing cliff failure mechanisms.

#### 5.1.3.1 Numerical analysis of homogeneous vertical cliffs with a notch depth of 7 meters and a joint length of 23.75 meters

According to Inkate (2023), when the joint length is 23.75 meters, the joint persistence (p) that leads to a becomes 62.40%, critical SRF equal to 1, indicating that the cliff is close to instability. Therefore, according to Eq.(1) the joint properties obtained from the analysis are as follows:

Table 12 The strength parameters of the joint considering a joint persistence of 62.40% for the length of 23.75 meters.

Strength parameter for joint	Value and physical units
Cohesion ( $c_{joint}$ )	1.491E+05 Pa
Friction angle ( $\varphi_{joint}$ )	35.64°
Tensile strength ( $\sigma_{t,joint}$ )	1.429E+05 Pa

As shown in Table 13, the SRF values were obtained by changing the joint horizontal location with respect to the cliff face. The analysis begins with the joint 4 meters from the cliff face, which is located to the right of the notch end. Afterward, the joint was moved to the right in 1-meter increments until the analysis stopped at the joint 16 meters from the cliff face. At each joint position, critical SRF values are obtained, allowing the correlation between the joint length of 23.75 meters at different horizontal positions and SRF to be studied.

Table 13 Influence of horizontal location of joints with the joint length of 23.75 meters and notch depth of 7 meters.

Joint location [m]	*SRF [-]	**SRF [-]
4	2.14	2.03
5	2.11	1.97
6	1.60	unknown
7	1.26	0.91
8	1.70	1.66
9	1.86	1.88
10	2.03	1.93
11	2.17	0.49
12	1.01	0.61
13	1.11	0.79
14	1.32	0.98
15	1.39	1.17
16	-	1.28

\*: The data is from Inkate (2023). \*\*: The data is from this study.

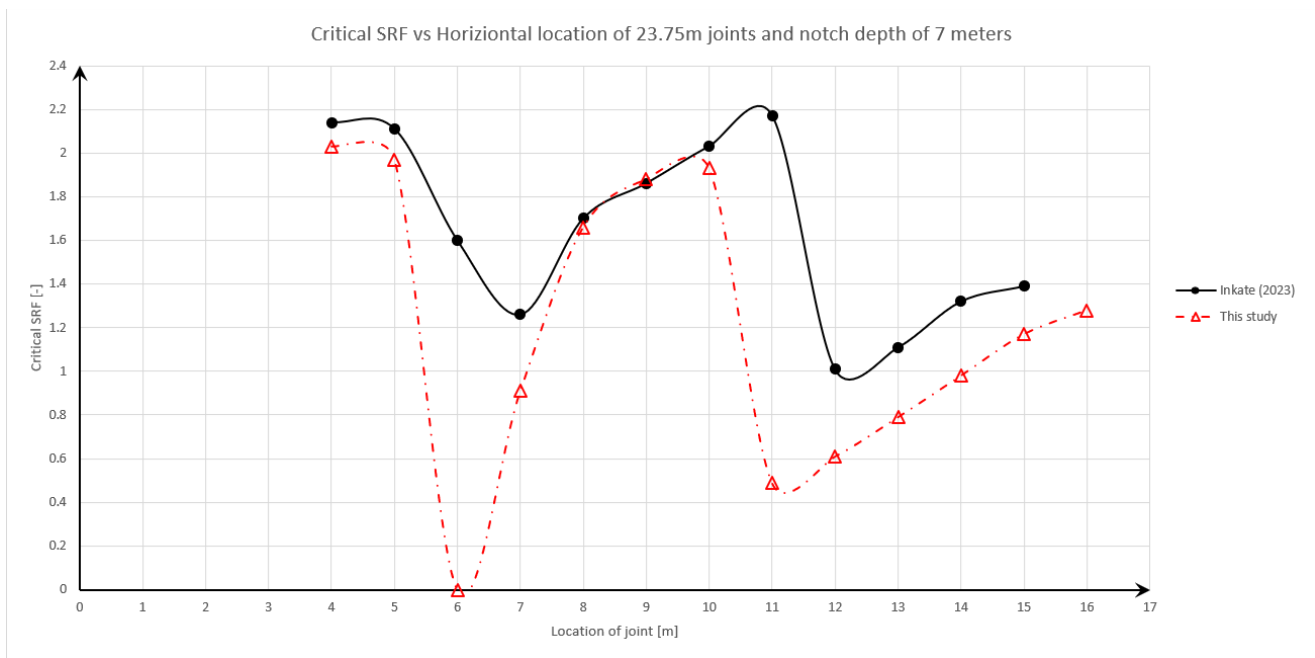


Figure 37 Comparison the Inkate's (2023) results with this study's results of the influence of horizontal joint location on the cliff stability ( $L_{joint}=23.75$  meters) and notch depth of 7 meters

Increasing the horizontal distance from the cliff face of the joint from 4 meters to 5 meters decreases the critical SRF values from 2.03 to 1.97. During this process, the influence of the joint on the stability of the cliff gradually increases, leading to a decrease in stability and a lower critical SRF value. When the joint is at 6 meters from the cliff face, a collapse occurs (convergence is not reached). From 7 meters to 10 meters, the critical SRF value gradually increases from 0.91 to 1.93. However, at a horizontal distance of 11 meters, the critical SRF does not continue to increase; instead, it rapidly drops from 1.93 to 0.49. As the joint shifts from 11 meters to 16 meters, the critical SRF value increases from 0.49 to 1.28. This increase occurs because the joint is moving farther away from the deepest part of the notch, weakening its influence on the stability of the cliff, and resulting in a gradually increasing critical SRF value. This trend is similar to the results of Inkate (2023).

### 5.1.3.2 Numerical analysis of homogeneous vertical cliffs with a notch depth of 7 meters and a joint length of 18.75 meters

Table 14 reveals that RS2 software could find a convergence when the joint persistence was less than 65%; for instance, the critical SRF is equal to 0.58 at a joint persistence of 63.75%. By decreasing the values of joint persistence from 63.75% to 60%, SRF values increase from 0.58 to 1.91.

Table 14 Results of parametric analysis of 25 m high homogeneous cliff with 18.75 m long joint, and a notch depth of 7 m.

Experiment number	Joint length		P	Friction angle	Cohesion	Tensile strength	SRF
	[%]	[m]	[%]	[deg]	[MPa]	[MPa]	[-]
1	75%	18.75	70.00%	34.50	0.1210	0.1140	unknown
2	75%	18.75	65.00%	35.25	0.1395	0.1330	unknown
3	75%	18.75	63.75%	35.44	0.1441	0.1378	0.58
4	75%	18.75	63.50%	35.48	0.1451	0.1387	0.74
5	75%	18.75	63.32%	35.50	0.1457	0.1394	1
6	75%	18.75	63.00%	35.55	0.1469	0.1406	1.21
7	75%	18.75	62.50%	35.63	0.1488	0.1425	1.45
8	75%	18.75	60.00%	36.00	0.1580	0.1520	1.91

Parametric analysis can be performed to identify joint characteristics that contribute to cliff failure. When the joint persistence ( $p$ ) changes to 63.32%, the critical SRF equals 1, indicating that the cliff is approaching instability. Therefore, the joint properties obtained from the analysis are collected in Table 15.

Table 15 The strength parameters of the joint considering joint persistence =63.32% for the length of 18.75 meters.

Strength parameter for joint	Value and physical units
Cohesion ( $c_{joint}$ )	1.457E+05 Pa
Friction angle ( $\varphi_{joint}$ )	35.5°
Tensile strength ( $\sigma_{t,joint}$ )	1.394E+05 Pa



The model considers a joint with a length of 18.75 meters from the top surface, constituting 75% of the cliff height. The parameters of the joint are outlined in [Table 15](#).

[Table 16](#) illustrates the variations in critical SRF values obtained by changing the horizontal location of the joint from the cliff face. The analysis begins with the joint located 4 meters from the left cliff face. Subsequently, the joint is incrementally shifted to the right by 1 meter until it reaches a position of 16 meters. The critical SRF values are obtained for each joint position, allowing the correlation between the horizontal position of the joint and the SRF.

*Table 16 Influence of horizontal location of joints with the joint length of 18.75 meters and notch depth of 7 meters.*

Joint location	SRF
[m]	[-]
4	2.02
5	1.95
6	1.36
7	1.01
8	1.55
9	1.82
10	1.91
11	unknown
12	0.61
13	0.85
14	1.04
15	1.11
16	1.30

A joint at different horizontal positions is divided into the following four color groups, as shown in [Figure 38](#).

- Red Group 1: Close to the edge of the cliff-side surface (Joint location: 4-7 meters)
- Yellow Group 2: Inside the area of maximum shear strain from the cliff model's results without joint. (Joint location: 7-10 meters)
- Green Group 3: Close to the area of maximum shear strain from the cliff model's results without joint. (Joint location: 10-11 meters)
- Blue Group 4: Far from the edge of the cliff-side surface (Joint location: 11-16 meters)

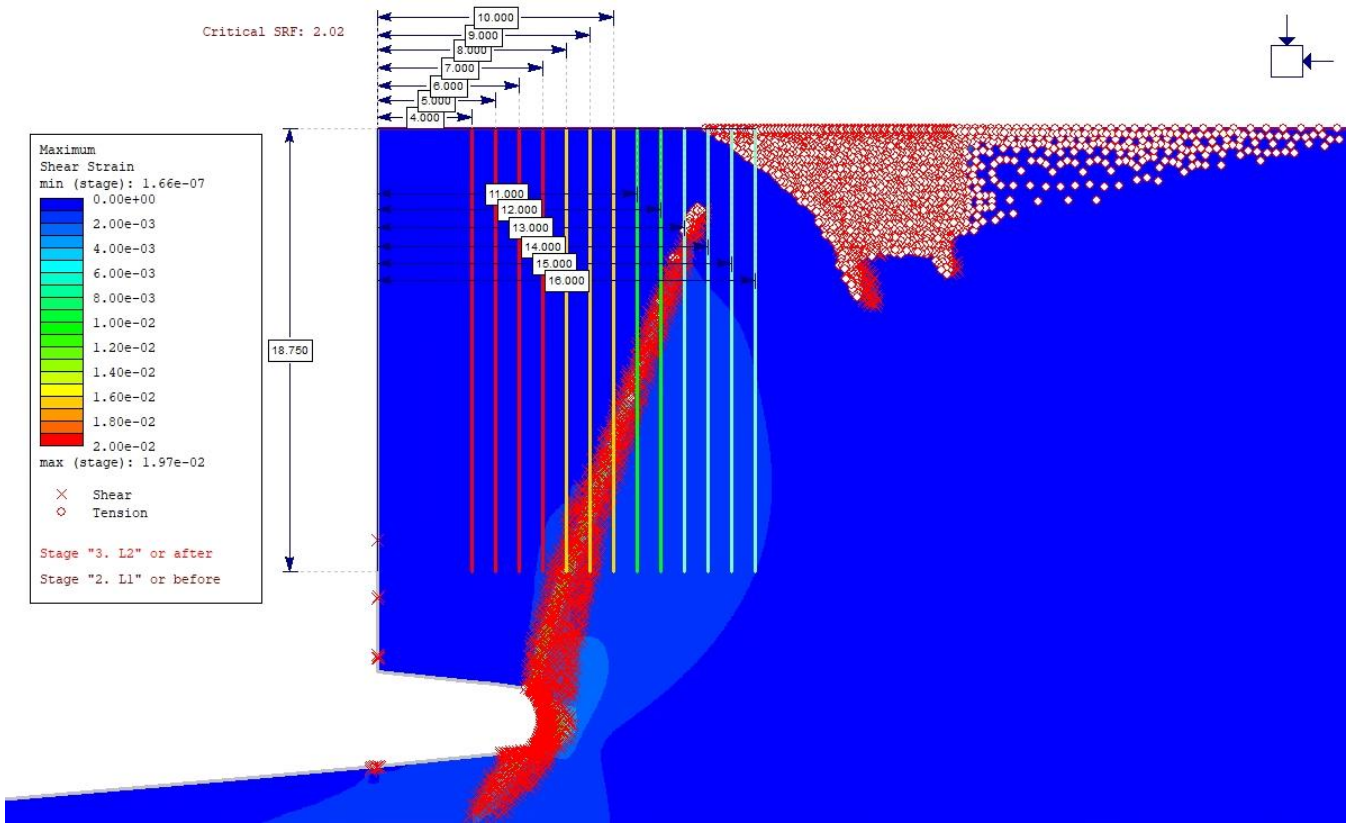


Figure 38 In the background: the cliff model with a notch depth of 7 meters without joint (SRF 2.02), and superimpose the joint at different horizontal locations.

Figure 39 represents the correlations between the horizontal location of joint and critical SRF values.

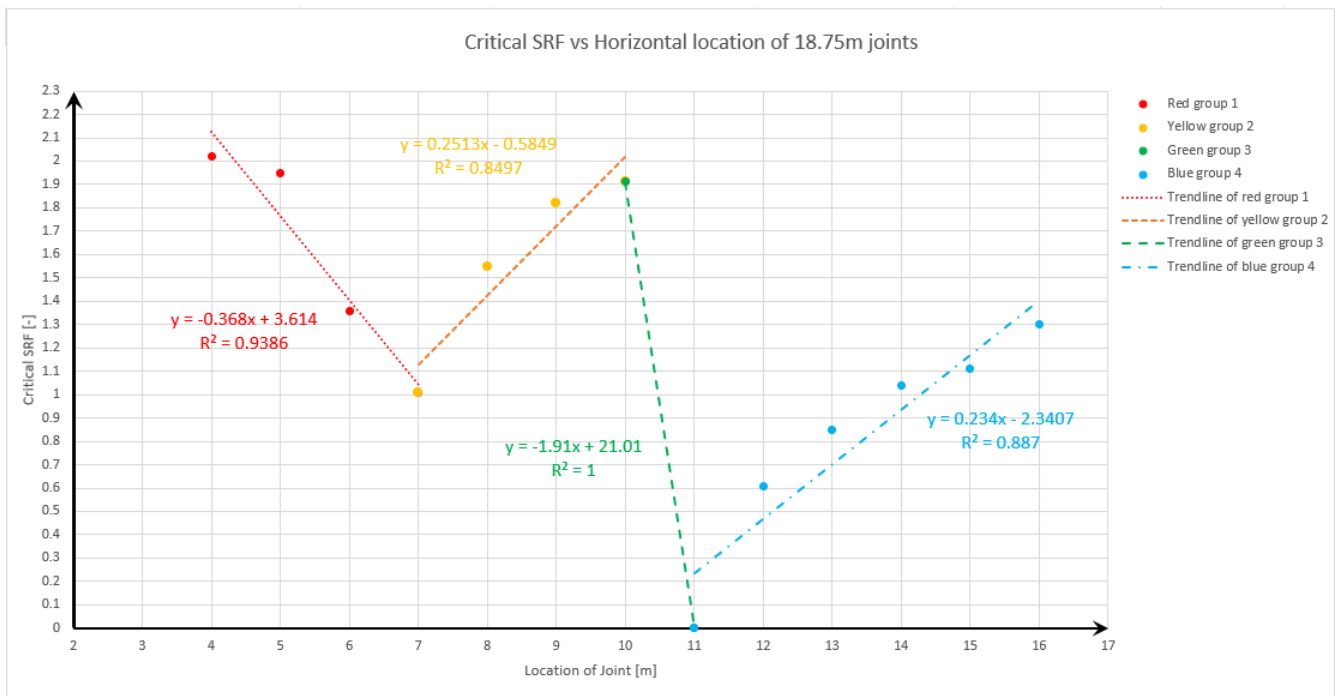


Figure 39 The influence of horizontal joint location on the cliff stability ( $L_{joint}=18.75$  meters) and notch depth of 7 meters.

For Red Group 1, the critical SRF value gradually decreases as the joint moves toward the inside of the cliff. By increasing the horizontal location from 4 meters to 7 meters, the critical SRF values drop from 2.02 to 1.01. During this process, joint interference with cliff stability ranges from nonexistent to negligible and then to significant, leading to a decrease in cliff stability and a reduction in the critical SRF value. Additionally, the maximum shear strain gradually shifts from an "original" band to being concentrated between the joint tip and the notch apex (Figure 60-Figure 62).

For joint locations from 7 meters to 10 meters in Yellow Group 2, the critical SRF value increases as the joint shifts toward the inside of the cliff. The critical SRF values increase from 1.01 to 1.91 with increasing the horizontal location. In addition, as the distance between the bottom of the joint and the apex of the notch increases, the shear strain band becomes concentrated between them and gradually widens. Although the unstable volume portion of the cliff increases, the overall stability of the cliff improves (Figure 63-Figure 66).

Compared to the previous group, Green Group 3 shows that as the bottom of the joint moves away from the maximum shear strain area, the critical SRF does not increase; instead, the critical SRF drops sharply from 1.91 to unknown (a value of 0, indicating the cliff is in an unstable state, and the maximum shear strain band is fully connected between the joint tip and the notch apex: Figure 67).

For Blue Group 4, as the joint moves from 11 meters to 13 meters, the critical SRF value increases from 0 to 0.85, but the cliff remains in a relatively unstable state. Once the joint's horizontal position exceeds 13 meters, the critical SRF consistently remains greater than 1, continuing to increase from 1.03 to 1.30. The results indicate that the further the joint is from the deepest part of the notch, the weaker its impact on the stability of the cliff, resulting in a gradual increase in the critical SRF value. Furthermore, the main maximum shear band (analogous to a homogeneous cliff without joints) bends toward the joint and induces another maximum shear band at the tip joint. Finally, the two bands connect (Figure 68-Figure 72).

Beyond 16 meters from the cliff face, joints located at large distances from the cliff face are unlikely to significantly affect the cliff's stability.

## 5.2 FDEM Numerical analyses

### 5.2.1 Homogeneous vertical cliff without joint

During the FDEM analysis process, some parameters need to be defined, as shown in Table 17.

Table 17 Material properties and parameters required by Irazu software.

Strength parameter for conglomerate	Value and physical units	Irazu setting parameters	Value and physical units
Density	2100 kg/m <sup>3</sup>	Number of time steps	2500000
Young's modulus	2.40E+08 Pa	Time step size	2.10E-06 s
Poisson's Ratio	0.3	Gravity acceleration	-9.8 m/s <sup>2</sup>
Cohesion ( <i>c</i> )	3.80E+05 Pa		
Friction coefficient	1		
Tensile strength ( <i>σ</i> )	3.80E+05 Pa		
Mode I Fracture Energy	12 N/m		
Mode II Fracture Energy	120 N/m		

The results for the four models are depicted as variations in vertical stress over time steps. In all the legends, the maximum positive value is 2.535E+05, which represents tensile stress, while the maximum negative value is -3.598E+06, which represents compressive stress.

- Homogeneous vertical cliff without joint and excavation stage.

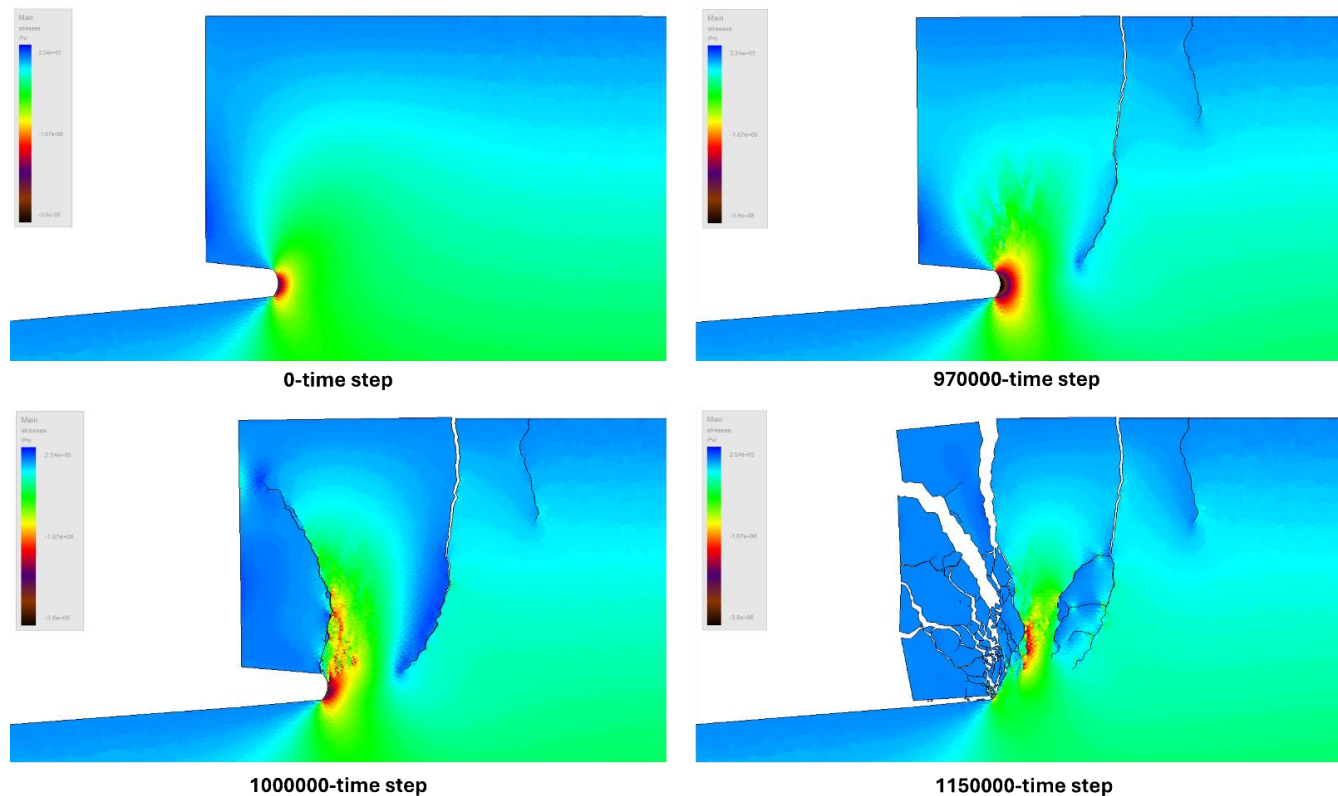


Figure 40 Simulated evolution of vertical stress contour and fracture pattern after (a) 0-time step, (b) 970,000-time step, (c) 1,000,000-time step, and (d) 1,150,000-time step.

Initially, larger vertical compressive stress is concentrated at the deepest part of the notch. As the time steps reach 970,000, the red and yellow areas indicating vertical compressive stress expand and spread to the cliff area above the notch. Meanwhile, two nearly vertical cracks appear within the cliff, with one crack gradually extending and bending towards the deepest part of the notch (Figure 40b). By 1,000,000 time steps, the arc-shaped crack at the deepest part of the notch rapidly extends to the left surface of the cliff. Due to the formation of this crack, some vertical stress propagates along the crack (Figure 40c). After 150,000 time steps, the cliff above the notch has completely collapsed. As the cliff collapses, the vertical stress weakens, and part of the stress disperses along the vertical cracks within the cliff (Figure 40d).

- Homogeneous vertical cliff without joint, with 2-notch excavation stages.

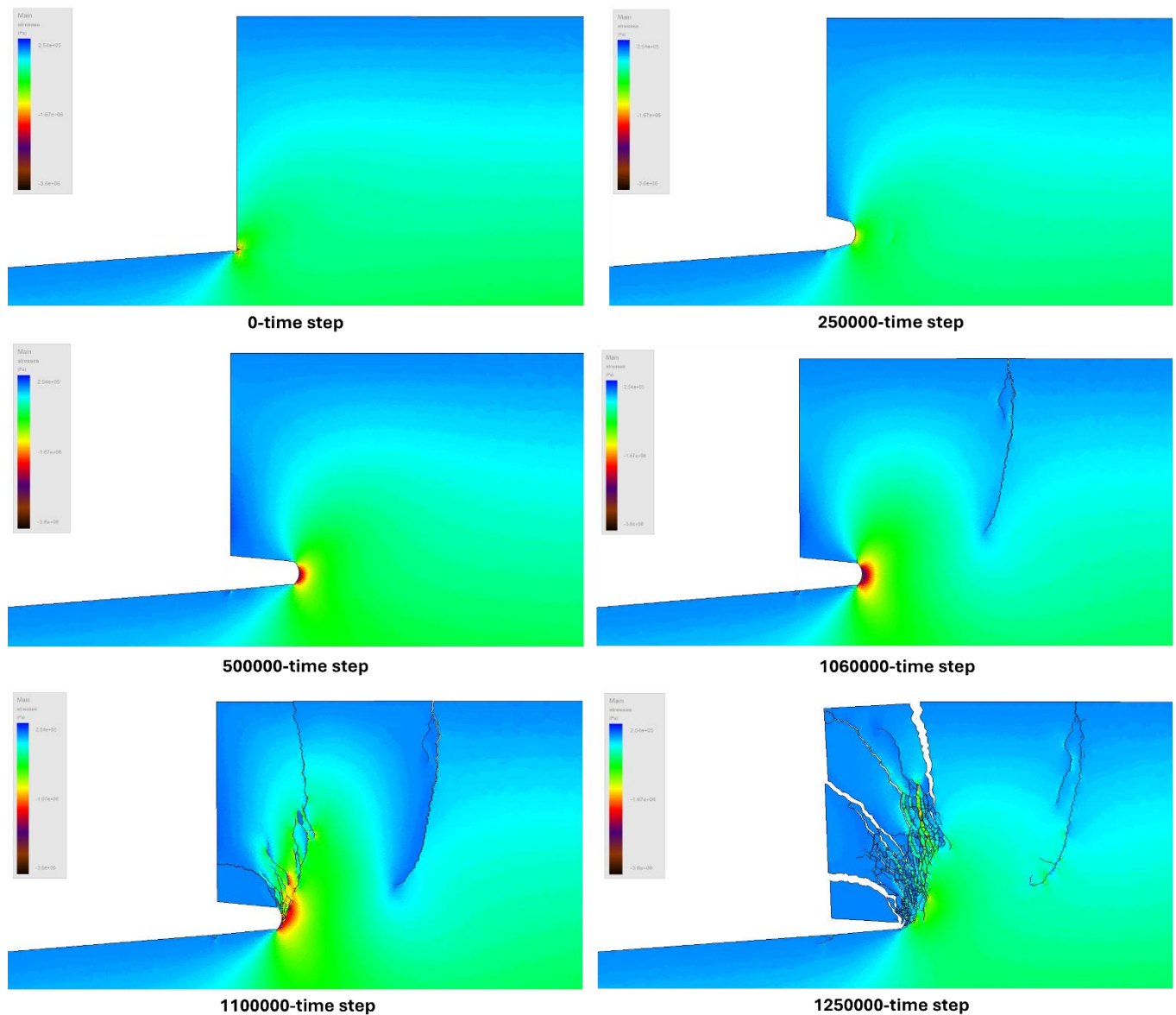
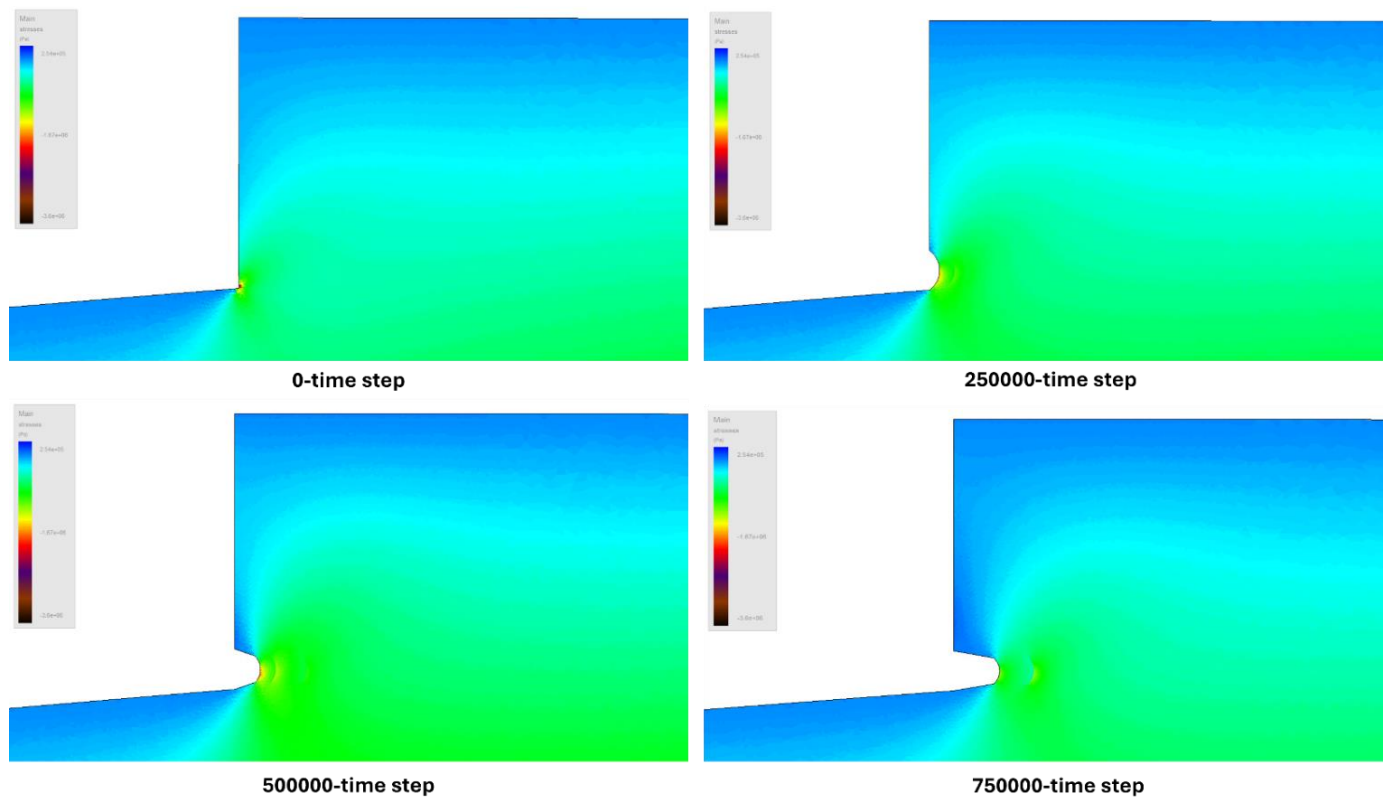


Figure 41 Simulated evolution of vertical stress contour and fracture pattern after (a) 0-time step, (b) 250,000-time step, (c) 500,000-time step, (d) 1,060,000-time step, (e) 1,100,000-time step, and (f) 1,250,000-time step.

In the initial time steps, vertical stress can be observed to be concentrated at the lower left corner of the cliff. Subsequently, the core modulus reduction method is employed to excavate the notch every 250,000-time step, simulating the erosion of the cliff by seawater. During the excavation process, no cracks form, but each excavation results in some vertical stress concentration at the top of the notch (Figure 41b, c). At 1,060,000 time steps, the red area of vertical compressive stress expands, and cracks gradually extend and bend towards the deepest part of the notch inside the cliff. Due to the occurrence of cracks, the tensile stress around them increases (Figure 41d). By 1,100,000 time steps, numerous arc-shaped cracks rapidly extend from the deepest part of the notch to the left side and the top of the cliff. Due to the formation of these cracks, some vertical stress propagates along the paths of the cracks (Figure 41e). After 150,000 time steps, the section of the cliff above the notch completely collapses, and the vertical stress gradually dissipates as the cliff collapses (Figure 41f).

- Homogeneous vertical cliff without joint, with 4-notch excavation stages.



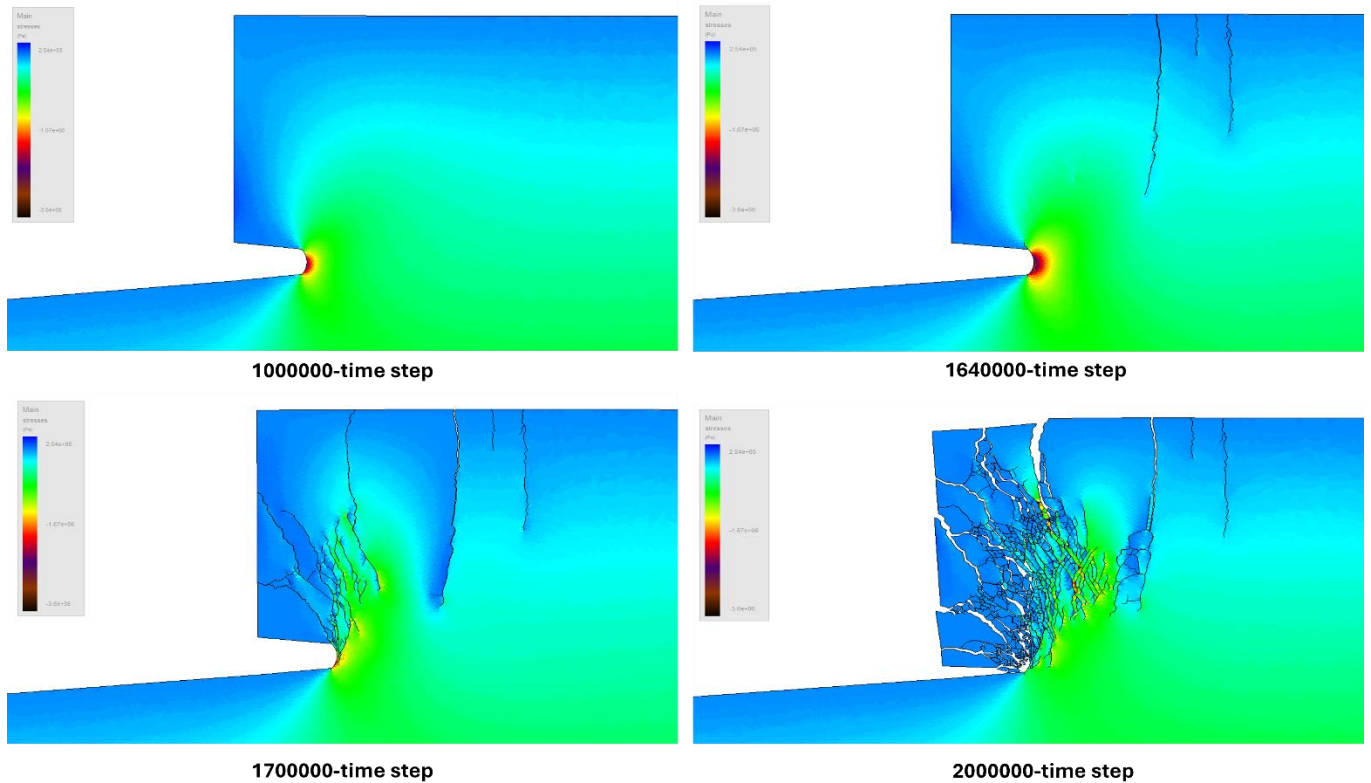


Figure 42 Simulated evolution of vertical stress contour and fracture pattern after (a) 0-time step, (b) 250,000-time step, (c) 500,000-time step, (d) 750,000-time step, (e) 1,000,000-time step, (f) 1,640,000-time step, (g) 1,700,000-time step, and (h) 2,000,000-time step.

The results show that at time step 0, there is a concentration of vertical stress at the lower left corner of the cliff. Subsequently, the core modulus reduction method is used to excavate the notch every 250,000 time steps, for a total of four excavations. During the excavation process, no cracks form, but each excavation causes a small concentration of vertical stress at the top of the notch (Figure 42b-e). At time step 1,640,000, the area of vertical compressive stress expands, and three cracks form inside the cliff, gradually extending and bending towards the deepest part of the notch, and the tensile stress around them increases (Figure 42f). By time step 1,700,000, numerous arch-shaped cracks rapidly extend from the deepest part of the notch to the left side and the top of the cliff. The formation of these cracks causes some vertical stress to propagate along the cracks (Figure 42g). After 300,000 time steps, the section of the cliff above the notch completely collapses. As the cliff collapses, the vertical stress gradually dissipates (Figure 42h).

- Homogeneous vertical cliff without joint, with 10 vertical and 4-notch excavation stages.

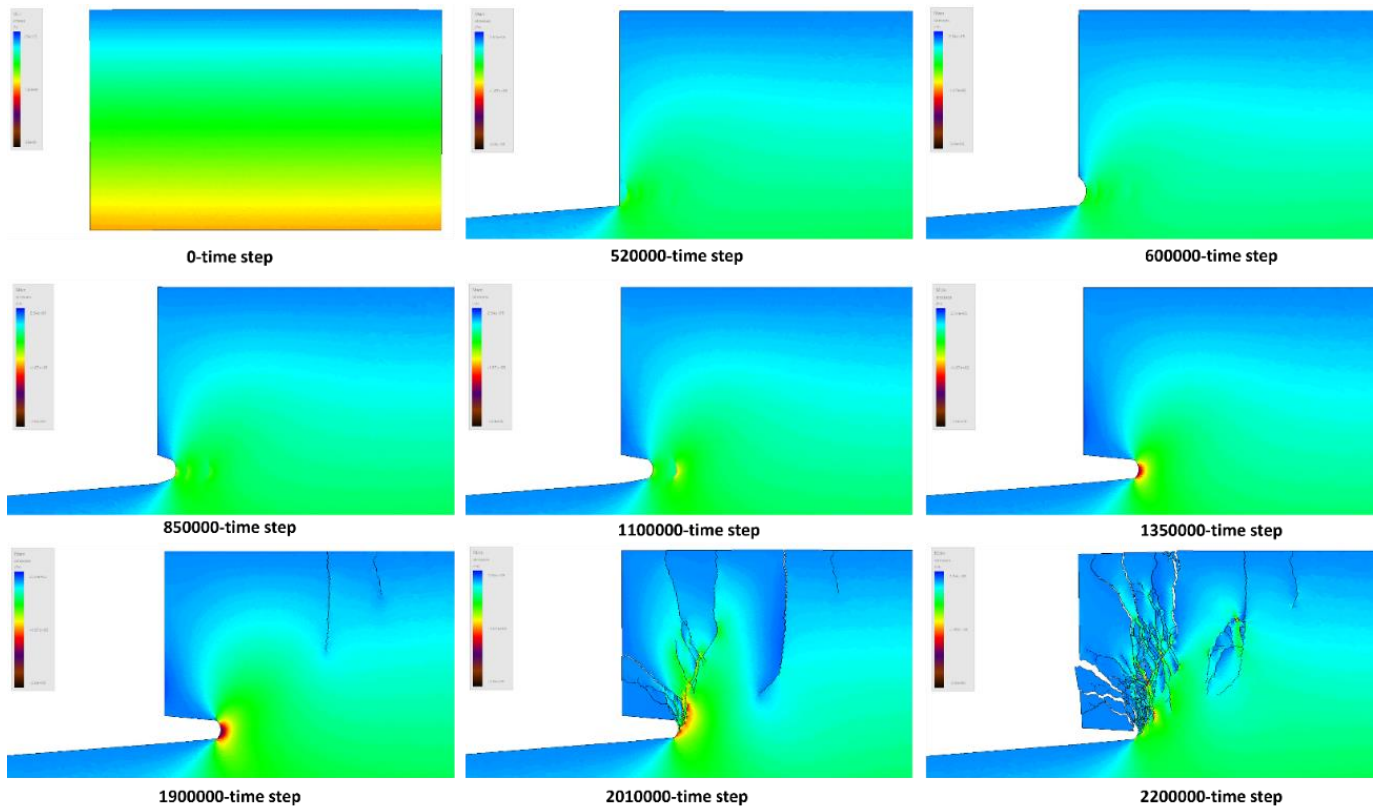


Figure 43 Simulated evolution of vertical stress contour and fracture pattern after (a) 0-time step, (b) 520,000-time step, (c) 600,000-time step, (d) 850,000-time step, (e) 1,100,000-time step, (f) 1,350,000-time step, (g) 1,900,000-time step, (h) 2,010,000-time step, and (i) 2,200,000-time step.

The results show that from time step 0 to time step 520,000, the left half of the rectangular model is excavated vertically downward, forming a vertical cliff. No cracks formed during the excavation, and after completion, no vertical stress concentration was observed at the lower left corner of the cliff (Figure 43a, b). Subsequently, the core modulus reduction method is used to excavate the notch every 250,000 time steps, for a total of four excavations. No cracks form during the excavation process, and each excavation causes almost no vertical stress concentration at the top of the notch (Figure 43c-f). At time step 1,900,000, the area of vertical compressive stress expands, and two cracks form inside the cliff, with one gradually extending and bending towards the deepest part of the notch, and the tensile stress around it fluctuates (Figure 43g). By time step 2,010,000, numerous arc-shaped cracks rapidly extend from the deepest part of the notch to the left side and the top of the cliff. The formation of these cracks causes some vertical stress to propagate along the paths of the cracks (Figure 43h). After 190,000 time steps, the section of the cliff above the notch completely collapses, and the vertical stress gradually dissipates as the cliff collapses (Figure 43i).



In the comparison of the result of FEM and FDEM analyses, the result from RS2 software (implementing Finite Element Method analysis) shows a single maximum shear strain band extending to the top surface of the cliff, along which the main crack propagates, with no cracks or strain appearing in the rest of the cliff (Figure 44 b). In contrast, the result of Irazu software (implementing Finite Discrete Element Method analysis) shows multiple cracks propagating from the notch to the cliff surface, and a deep tensile crack appearing within the cliff (Figure 44 a). The results from Irazu seem to be more realistic compared to those from RS2.

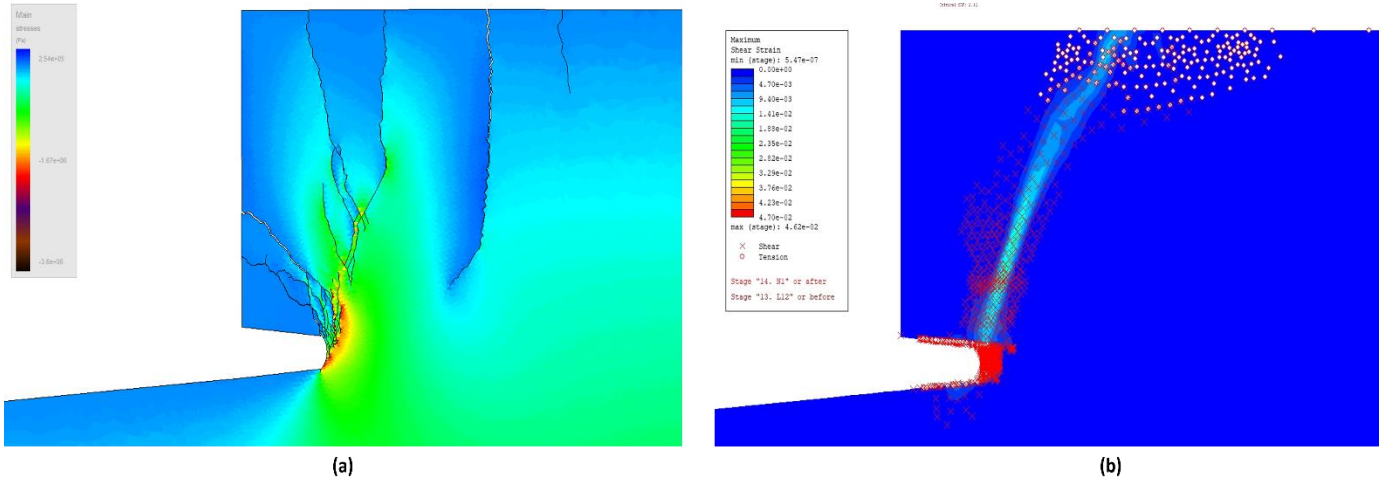


Figure 44 The results of the homogeneous vertical cliff without joint (a) Irazu (b) RS2, from Inkate 2023.

### 5.2.2 Homogeneous vertical cliff with joint

To visually study the influence of long and short joints on the cliff, the results show the development of cracks and the change of vertical stress with time.

- Homogeneous vertical cliff with 13.75 m short persistent joint.

Some parameters need to be defined for the joint length of 13.75 m, as shown in Table 18.

Table 18 The 13.75 meters joint properties and parameters required by Irazu software.

Strength parameter for joint	Value and physical units	Irazu setting parameters	Value and physical units
Cohesion ( $c$ )	5.44E+04 Pa	Number of time steps	2500000
Friction angle	31.8°	Time step size	2.10E-06 s
Tensile strength ( $\sigma$ )	4.56E+04 Pa	Gravity acceleration	-9.8 m/s <sup>2</sup>
Mode I Fracture Energy	1 N/m		
Mode II Fracture Energy	5 N/m		

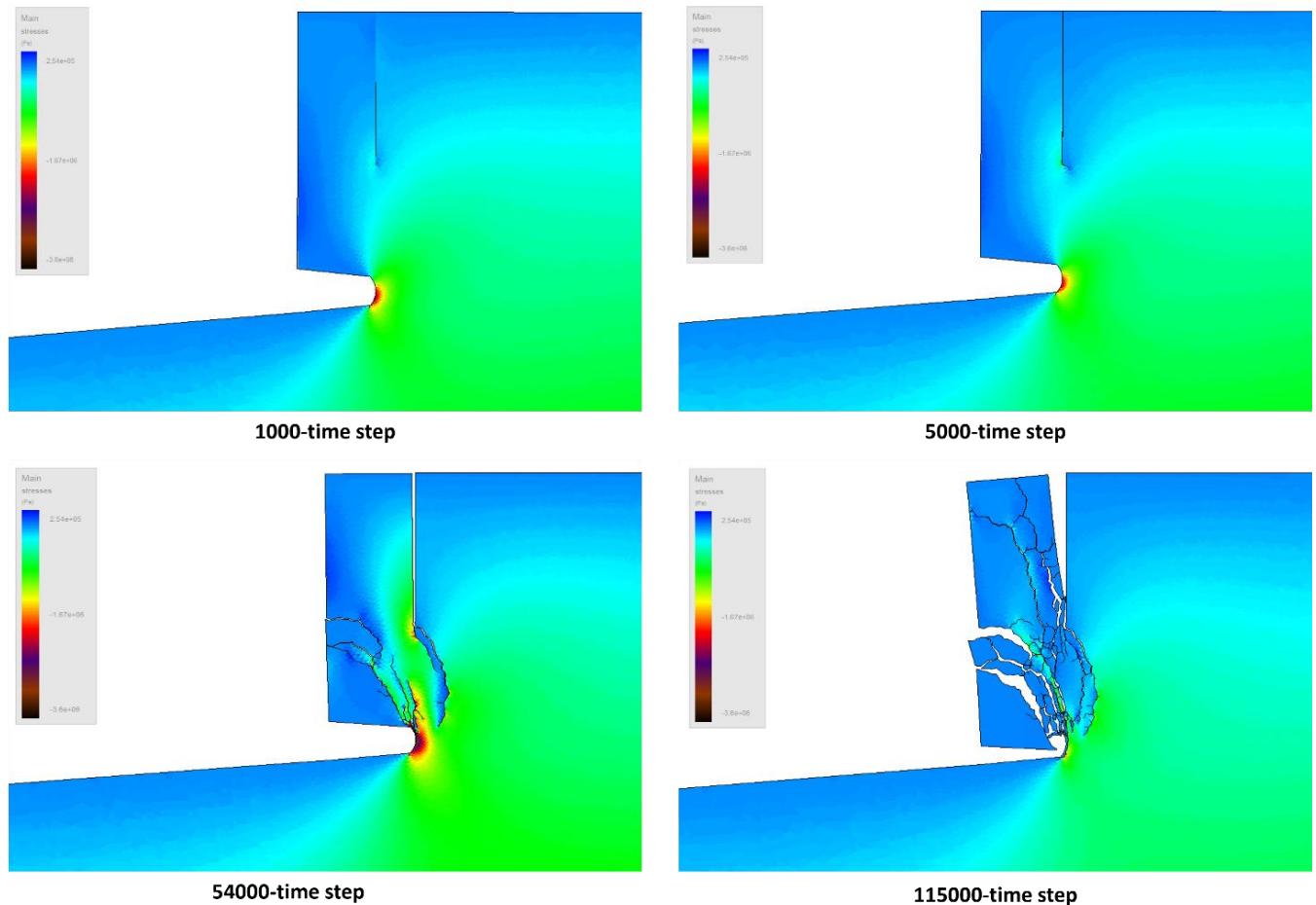


Figure 45 Simulated evolution of vertical stress contour and fracture pattern after (a) 1,000-time step, (b) 5,000-time step, (c) 54,000-time step, and (d) 115,000-time step.

At the 1,000-time step, the vertical compressive stress is concentrated at the deepest part of the notch, and the vertical support stress is concentrated at the bottom of the joint, but no cracks are present (Figure 45a). From the 5,000 to the 54,000-time step, arc-shaped cracks rapidly extend from the bottom of the joint to the deepest apex of the notch. As the crack approaches the deepest part of the notch, the tensile stress around it increases, and the vertical compressive stress gradually increases at the deepest part of the notch. Additionally, many cracks spread rapidly from the deepest part of the notch to the left side of the cliff. This propagation is caused by the partial diffusion of vertical stress above the notch (Figure 45b, c). By 115,000 time steps, the cliff has completely collapsed (Figure 45d).

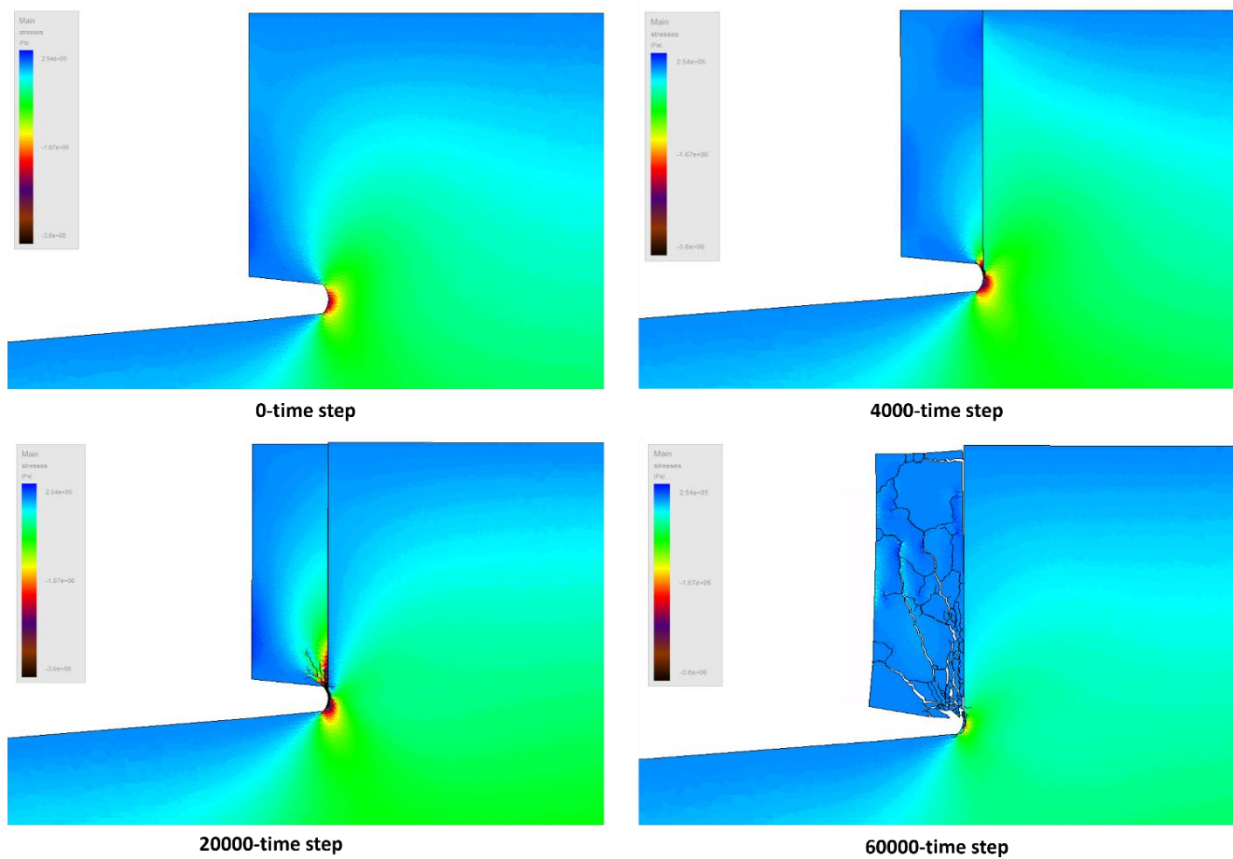
Differently from the homogeneous model without a joint, there are no cracks in the upper part of the slope. All cracks appear concentrated between the joint bottom and the notch tip, and the cracks spread quickly.

- Homogeneous vertical cliff with 23.75 m long persistent joint.

Some parameters need to be defined for the joint length of 23.75 m, as shown in [Table 19](#).

*Table 19 The 23.75 meters joint properties and parameters required by Irazu software.*

Strength parameter for joint	Value and physical units	Irazu setting parameters	Value and physical units
Cohesion ( $c$ )	1.457E+05 Pa	Number of time steps	2500000
Friction angle	35.5°	Time step size	2.10E-06 s
Tensile strength ( $\sigma$ )	1.394E+05 Pa	Gravity acceleration	-9.8 m/s <sup>2</sup>
Mode I Fracture Energy	1 N/m		
Mode II Fracture Energy	5 N/m		



*Figure 46 Simulated evolution of vertical stress contour and fracture pattern after (a) 0-time step, (b) 4,000-time step, (c) 20,000-time step, and (d) 60,000-time step.*

Initially, the vertical compressive stress is concentrated at the deepest part of the notch. At time step 4,000, a long predefined joint appears at a horizontal distance of 7 meters, very close to the deepest tip of the notch (Figure 46a, b). Shortly thereafter, the crack rapidly connects the deepest part of the notch to the bottom of the joint, causing a sharp increase in vertical compressive stress. After 20,000 time steps, numerous cracks rapidly extend from the deepest part of the notch to the cliff above the notch. By 60,000 time steps, the cliff above the notch has completely collapsed (Figure 46c, d). Unlike the previous model, the rock mass on the right of the joint is unaffected by any crack.

In the comparison of the results of FEM and FDEM analyses, for the two joints of different lengths, the FEM analysis results show that the maximum shear strain appears only between the bottom end of the joints and the tip of the notch, without extending elsewhere. However, the FDEM analysis results show numerous cracks propagating from the deepest part of the notch to the left side face of the cliff.

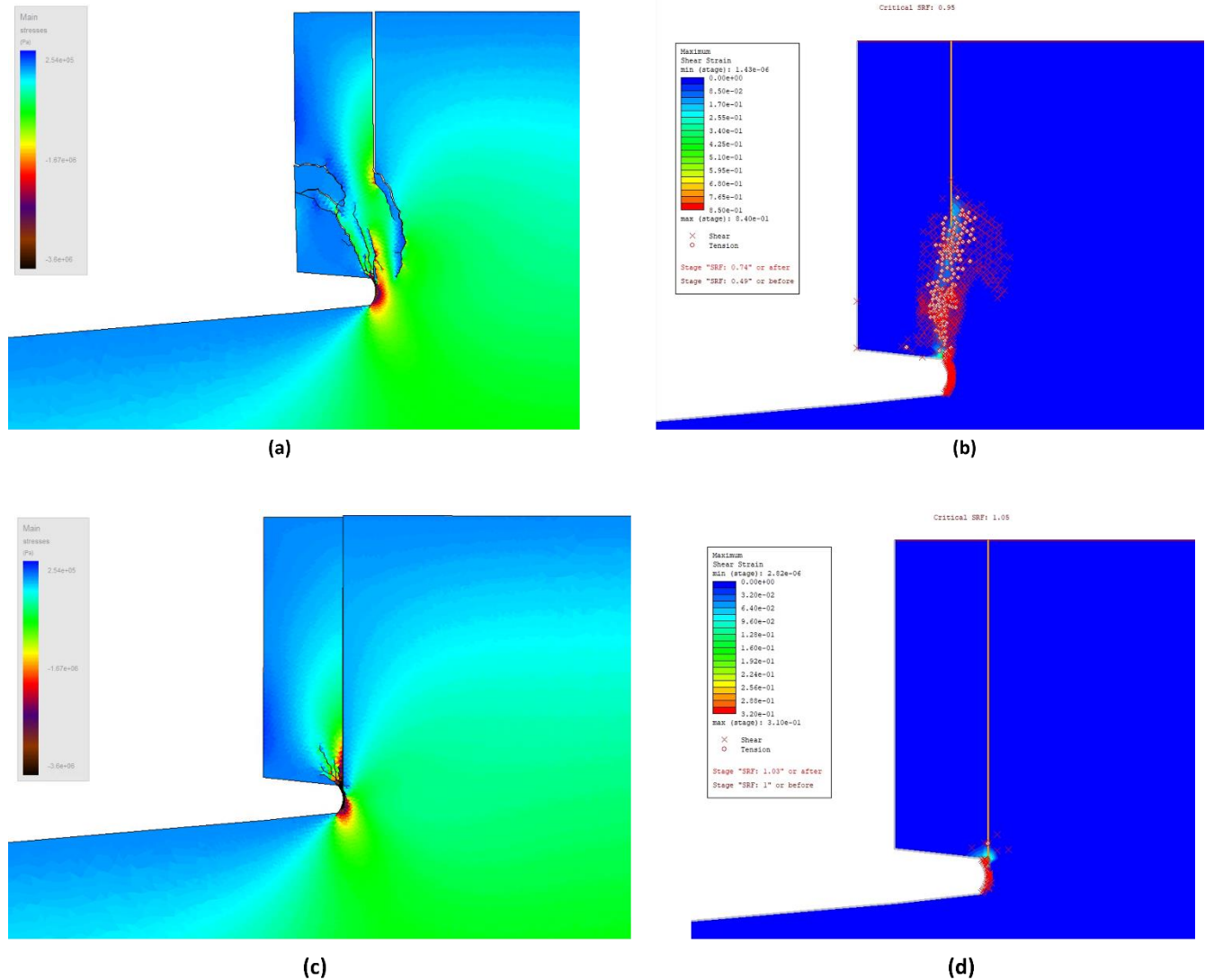


Figure 47 The results of the homogeneous vertical cliff with 13.75 meters joint (a) Irazu (b) RS2, from Inkate 2023; The results of the homogeneous vertical cliff with 23.75 meters joint (c) Irazu (d) RS2, from Inkate 2023.

## 6. Discussion

### *The homogeneous vertical cliff without joint using the FEM approach.*

Inkate (2023) utilized the finite element method and RS2 software to analyze cliffs of varying heights with notches depths of 10 meters, 7 meters, and 3 meters. The results elucidate the correlation between cliff slenderness ratio and critical SRF, showcasing distinct mechanical failure patterns in high and low slenderness ratio cliffs.

This study, employing the same software as Inkate (2023), extends Inkate's research findings and delves into the failure mechanisms of cliffs, particularly focusing on maximum shear strain under failure conditions. Cliffs are classified based on slenderness (defined as the ratio between the cliff height and the notch depth), a critical factor influencing sea cliff behavior. Two primary categories emerge high and low slenderness cliffs. Cliffs with a 5-meter deep notch are further divided into high slenderness cliffs (if the overhanging rock height exceeds 10 meters) and low slenderness cliffs (if the height is 10 meters or less).

In high slenderness cliffs, shear strain contours demonstrate a linear pattern, propagating from the notched end to the cliff's top surface. Measuring the inclination angles of the shear band offers insight into locating the failure plane relative to the cliff face. A strong correlation is evident: as cliff height decreases, the shear band inclination increases, indicating a shift in the failure mechanism from shear to tensile, and the collapse mode also changes from sliding to toppling.

Conversely, in low cliffs, the concentrated area of maximum shear strain does not follow a linear shape but extends wider towards the cliff face, forming a triangular pattern. These findings facilitate the quantification of triangular areas concerning the distance from the cliff face (L1) and the width of the concentrated area on the cliff top face (L2). As cliff height decreases, concentrated areas tend to approach the cliff face, and the top surface becomes narrower. Besides maximum shear strain, the distribution of yielded elements significantly aids in studying failure mechanisms. Initial tensile failure is observed along a triangular shear strain profile on the top surface, followed by downward spreading and connection to the notch end, consistent with Inkate's findings (2023).

### *The homogeneous inclined cliff without joint using the FEM approach.*

This study employed RS2 software simulation to comprehensively analyze the effects of cliff topography variations on failure mechanisms and stability, with a particular focus on the maximum shear strain band under failure conditions. Transitioning from a vertical 90° cliff to a slope with a 70° inclination angle enhances cliff stability, yet the failure mechanism remains consistent, predominantly governed by shear stress.

### *The homogeneous vertical cliff with joint using the FEM approach.*

Inkate (2023) conducted a finite element analysis of a homogeneous cliff measuring 25 meters in height, with a notch depth of 7 meters and a joint length of 13.75 meters. The study revealed a V-shaped trend in the relationship between joint positions and critical SRF values. Additionally, extending the joint length to 23.75 meters resulted in a W-shaped trend in this relationship.

To further investigate the impact of joint horizontal placement on cliff stability, numerical analyses were performed on homogeneous cliffs measuring 25 meters in height with a 7-meter-deep notch. By varying the placement of 18.75 meters length joints (at different horizontal positions), the study analyzed cliff stability. SRF values obtained from these analyses categorized the correlation between joint horizontal placement and critical SRF values into four groups: close to the edge of the cliff side surface (4-7 meters), within the region of maximum shear strain observed in the jointless cliff model (7-10 meters), near the region of maximum shear strain observed in the jointless cliff model (10-12 meters), and far from the edge of the cliff-side surface (12-16 meters), as illustrated in [Figure 39](#). These changing trends exhibited a W-type pattern similar to the findings of Inkate's study (2023) with a 23.75 meters joint length.

In the group close to the edge of the cliff-side surface, the critical SRF values gradually decrease as joints shift towards the internal cliff, yet they consistently remain above one. Appendix C, [Figure 60](#) illustrates that when the joint is at a horizontal distance of 4 meters from the cliff face, it is farther from the (homogeneous model) shear strain band and the deepest tip of the notch, resulting in the maximum shear strain band not extending to the bottom of the joint. The cliff's stability is slightly affected by the joint. However, when the joint moves to 5 meters, the cliff stability begins to be affected, as depicted in [Figure 61](#), where the maximum shear strain area first spreads to the bottom of the joint and then gradually extends to the top of the cliff. As the joint moves from 6 meters to 7 meters, the distance between the bottom part of the joint and the deepest part of the notch gradually shortens, shifting towards inside the maximum shear strain zone. This causes the maximum shear strain band not to spread directly to the top of the cliff but instead occurs only between the deepest part of the notch and the base of the joint, without reaching the cliff top. During this process, the influence of joints on the cliff's stability gradually increases ([Figure 62](#) and [Figure 63](#)). Additionally, the results indicate that as the joint moves from 4 meters to 7 meters, it does not entirely obstruct the paths of shear and tensile stresses propagating from the deepest part of the notch to the top of the cliff. Part of the shear stresses and tensile stresses are concentrated between the bottom of the joint and the deepest apex of the notch, while the remaining shear and tensile stresses spread to the top and left side of the cliff.

[Figure 63-Figure 66](#) clearly shows that during the joint movement from 7 meters to 10 meters, the maximum shear strain area connects the bottom of the joint and the deepest part of the notch. The influence of the joint on cliff stability gradually weakens as the distance between them increases and the critical SRF values go up from 1.01 to 1.91.

For the joint motion from 10 meters to 12 meters, as the joint bottom moves away from the maximum shear strain zone, the critical SRF does not increase. Instead, it plummets to 0.61, indicating very poor cliff stability. At a horizontal distance of 10 meters, the maximum shear strain occurs in the zone between the bottom of the joint and the deepest part of the notch, forming a triangular area. Furthermore, the joint does not impede the propagation of shear and tensile stresses to the interior and top of the cliff. However, when the joint moves to horizontal distances of 11 meters and 12 meters, it is evident that the maximum shear strain changes from a broad area to a narrow band, still connecting the bottom of the joint and the deepest tip of the notch. Particularly at a horizontal distance of 12 meters, the joint almost completely hinders the spread of shear and tensile stresses to

the interior and top of the cliff. This concentrates them in the area between the bottom of the joint and the deepest part of the notch, almost along the maximum strain band (Figure 66-Figure 68).

For the joint shifts beyond 12 m. The joint is farther and farther away from the deepest part of the notch, and its influence on the stability of the cliff is negligible, so the critical SRF value gradually increases (Figure 69-Figure 72).

#### *Homogeneous vertical cliff without joint using FDEM approach.*

This study utilized Irazu to conduct visual numerical analyses of four cliff models. By comparing the results, it was observed that in the fourth model (Figure 43), when the notch was not excavated (at time step 520,000), there was no vertical concentration stress in the lower left corner of the cliff. During the notch excavation process (from time step 600,000 to time step 1,350,000), a small stress concentration occurred at the deep part of each notch excavation. This model setup helps to mitigate the impact of concentrated stress on cliff stability analysis. Therefore, the fourth cliff model was deemed the most reasonable.

#### *Comparing the analysis results of the FEM and FDEM approach.*

The RS2 software utilizes finite element technology exclusively for analysis, taking about forty minutes to generate a result. The results are presented as images depicting the cliff's maximum shear strain, distribution, critical Safety Factor (SRF), and yielding zones, though the fracture propagation is not analyzed. Conversely, the Irazu software integrates both finite element and discrete element technologies, accounting for the impact of crack formation on cliff stability. This approach yields a more accurate and realistic digital simulation, although it takes at least eight hours or more. The results are displayed in video format, illustrating the cliff collapse process and enabling observation of crack formation and propagation during the collapse.

## 7. Conclusion

The purpose of this thesis is to study cliff failure mechanisms and key factors influencing cliff instability, particularly focusing on the presence of a notch caused by erosion and discontinuities such as joints. Both FEM and FDEM approaches are used for the numerical simulations. The results show that the emergence of a notch and joints will significantly affect the stability of the cliff, leading to a decrease in cliff stability until the cliff reaches a state of collapse.

In the first part, the differences in failure mechanisms are studied in homogeneous cliffs of different cliff heights, which are divided into two main categories according to their slenderness: high cliffs and low slender cliffs. In high slenderness cliffs, tensile failure showed up on the top surface of the cliff, indicating the possibility that tension cracks develop, whereas shear failure appeared mainly at the tip of the notch, and extended upwards towards the ground surface. Finally, the shear zone forms a band shape (failure surface) that connects from the end of the notch to the cliff top. However, in low slenderness cliffs, the maximum shear strain profile along with tensile failure initially forms a triangle at the cliff top, then propagates downward and connects to the notch end. This suggests that cliff failure occurs under tension rather than shear. This difference can result in different sizes of dropped blocks when the cliff reaches the condition failure.

Afterward, when the homogeneous high cliff is no longer vertical but has an inclination of  $70^\circ$ , the cliff becomes more stable although the failure mechanism is still dominated by shear stresses.

In addition, the presence of joints also has a significant effect on the stability and failure mechanisms of the cliff. In the analysis, the impact of a longer joint at different horizontal positions on the stability of the cliff was studied. The results show that as the joint gradually moves toward the interior of the cliff, the stability of the cliff gets weakened to strengthened. When the joint is at a certain horizontal distance, the stability of the cliff suddenly drops to extremely poor. It then gradually gets better, as indicated by the critical SRF forming an approximate W-shaped change trend.

In the final part, the Irazu software more effectively reflects the formation of cracks and the distribution of stress during the cliff collapse process. This allows for a better determination of the collapse area and mode and provides a more accurate analysis of the mechanism of cliff instability.



## 8. References

- Antonioli, F., Lo Presti, V., Rovere, A., Ferranti, L., Anzidei, M., Furlani, S., Mastronuzzi, G., Orru, P. E., Scicchitano, G., Sannino, G., Spampinato, C. R., Pagliarulo, R., Deiana, G., De Sabata, E., Sansò, P., Vacchi, M., & Vecchio, A. (2015). Tidal notches in Mediterranean Sea: A comprehensive analysis. *Quaternary Science Reviews*, 119, 66–84. <https://doi.org/10.1016/j.quascirev.2015.03.016>
- Antolini, F., Barla, M., Gigli, G., Giogetti, A., Intrieri, E., & Casagli, N. (2016). Combined Finite–Discrete Numerical Modeling of Runout of the Torgiovanetto di Assisi Rockslide in Central Italy. *International Journal of Geomechanics*, 16(6). [https://doi.org/10.1061/\(ASCE\)GM.1943-5622.0000646](https://doi.org/10.1061/(ASCE)GM.1943-5622.0000646)
- Barla, M., Piovano, G., & Grasselli, G. (2011). Rock Slide Simulation with the Combined Finite-Discrete Element Method. *International Journal of Geomechanics*, 12(6). [https://doi.org/10.1061/\(ASCE\)GM.1943-5622.0000204](https://doi.org/10.1061/(ASCE)GM.1943-5622.0000204)
- Budetta, P. (2010). Stability of an undercut sea-cliff along a Cilento coastal stretch (Campania, Southern Italy). *Natural Hazards*, 56, 233-250. <https://doi.org/10.1007/s11069-010-9565-y>
- Calista, M., Mascioli, F., Menna, V., Miccadei, E., & Piacentini, T. (2019). Recent Geomorphological Evolution and 3D Numerical Modelling of Soft Clastic Rock Cliffs in the Mid-Western Adriatic Sea (Abruzzo, Italy). *Geosciences*, 9(7), 309. <https://doi.org/10.3390/geosciences9070309>
- Dodge-Wan, D., & Nagarajan, R. (2019). Chapter 3 – Typology and Mechanisms of Coastal Erosion in Siliciclastic Rocks of the Northwest Borneo Coastline (Sarawak, Malaysia): A Field Approach. *Coastal Zone Management*, 65-98. <https://doi.org/10.1016/B978-0-12-814350-6.00003-3>
- Geomechanica Inc., (2023). Irazu 2D Geomechanical Simulation Software. V. 6.1. Theory Manual.
- Geomechanica Inc., 2023. Irazu 2D Geomechanical Simulation Software. V. 6.1. Tutorial Manual.
- Geomechanica Inc., 2023. Irazu 2D Geomechanical Simulation Software. V. 6.1. Verification Manual.
- Inkate, P. (2023) Numerical study on the failure mechanisms of rock cliffs subjected to basal erosion. Thesis, Politecnico di Torino.
- Kogure, T., Aoki, H., Maekado, A., Hirose, T., & Matsukura, Y. (2006). Effect of the development of notches and tension cracks on instability of limestone coastal cliffs in the Ryukyus, Japan. *Geomorphology*, 80(3-4), 236-244. <https://doi.org/10.1016/j.geomorph.2006.02.012>
- Kogure, T., & Matsukura, Y. (2011). Effect of vertical joints on the planar shape of fallen blocks in coastal collapses at Kuro-Shima, Okinawa, Japan. *The Japanese Geomorphological Union*, 32(1), 15-28.
- Lollino, P., Fazio, N.L., Perrotti, M., & Pesola, M.D. (2018). FDEM analysis of fracturing processes affecting vertical cliffs in soft calcarenites. *American Rock Mechanics Association*, 18-1178.
- Lollino, P., Pagliarulo, R., Trizzion, R., Santaloia, F., Pisano, L., Zumpano, V., Perrotti, M., & Fazio, N.L. (2021). Multi-scale approach to analyse the evolution of soft rock coastal cliffs and role of controlling factors: a case study in South-Eastern Italy. *Geomatics, Natural Hazards and Risk*, 12(1), p. 1058-1081. <https://doi.org/10.1080/19475705.2021.1910351>
- Mahabadi, O.K., Lisjak, A., Munjiza, A., & Grasselli, G. (2012). Y-Geo: New Combined Finite-Discrete Element Numerical Code for Geomechanical Applications. *International Journal of Geomechanics*, 12(6). [https://doi.org/10.1061/\(ASCE\)GM.1943-5622.0000216](https://doi.org/10.1061/(ASCE)GM.1943-5622.0000216)

- Miccadei, E., Mascioli, F., Ricci, F., & Piacentini, T. (2019). Geomorphology of soft clastic rock coasts in the mid-western Adriatic Sea (Abruzzo, Italy). *Geomorphology*, 324, p. 72-94. <https://doi.org/10.1016/j.geomorph.2018.09.023>
- Miščević, P., & Vlastelica, G. (2014). Impact of weathering on slope stability in soft rock mass. *Journal of Rock Mechanics and Geotechnical Engineering*, 6(3), 240–250. <https://doi.org/10.1016/j.jrmge.2014.03.006>
- Piovano, G., Antolini, F., Barla, M., & Barla, G. (2013). Continuum-Discontinuum Modelling of Failure and Evolution Mechanisms of Deep Seated Landslides. *6th International Conference on Discrete Element Methods (DEM6)*, Colorado School of Mines, Golden.
- Piovano, M., Barla, M., & Barla G. (2011). FEM/DEM modeling of a slope instability on a circular sliding surface. *13<sup>th</sup> International Conference of the IACMAG 2011*, Melbourne, Australia, 9–11 May 2011.
- Rocscience. (2020). RS2 Version 11.0-Finite Element Analysis for Excavations and Slopes. Canada Toronto, Ontario.
- Sunamura, T. (2015). Rocky coast processes: with special reference to the recession of soft rock cliffs. *Proceedings of the Japan Academy, Series B*, 91(9), 481-500. <https://doi.org/10.2183/pjab.91.481>
- Terefenko, P., & Terefenko, O. (2014). Determining the role of exposure, wave force, and rock chemical resistance in marine notch development. *Journal of Coastal Research*, 70, 706–711. <https://doi.org/10.2112/SI70-105a.1>
- Trenhaile, A. (2016). Modelling coastal notch morphology and developmental history in the Mediterranean. *GeoResJ*, 9–12, 77–90. <https://doi.org/10.1016/j.grj.2016.09.003>
- Zhang, Z.X. (2002) An empirical relation between mode I fracture toughness and the tensile strength of rock. *International Journal of Rock Mechanics and Mining Sciences*, 39(3), 401-406. [https://doi.org/10.1016/S1365-1609\(02\)00032-1](https://doi.org/10.1016/S1365-1609(02)00032-1)

## 9. Appendices

### 9.1 Appendix A: Numerical Results of Homogeneous Vertical Cliffs Without Joint

#### 9.1.1 A1 : Maximum shear strain of homogeneous vertical cliffs with notch depth of 5m

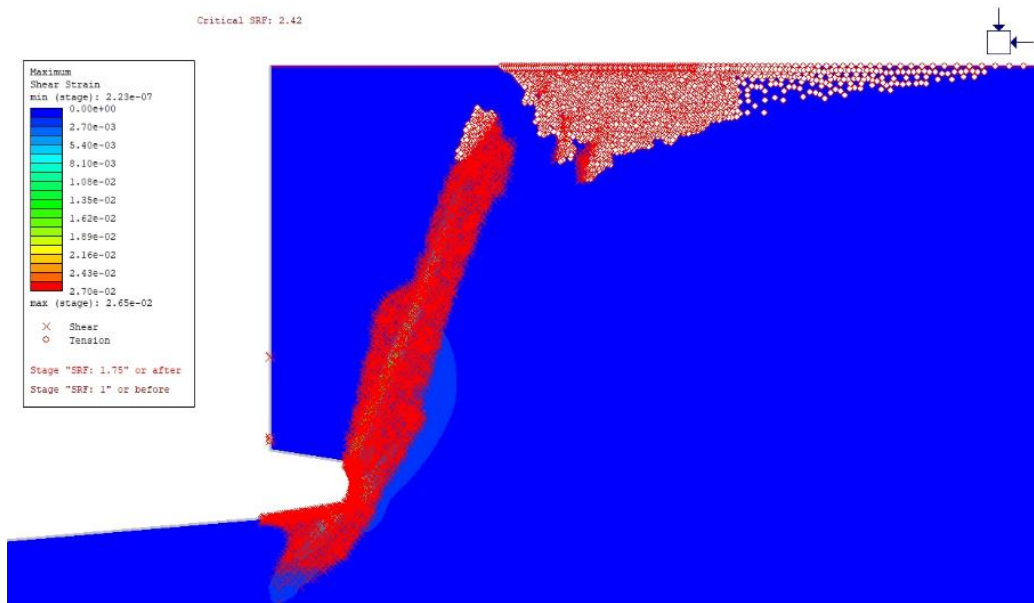


Figure 48 Maximum shear strain and distribution of yielded stresses of homogeneous vertical cliffs with 5 meters notch depth – Cliff height of 25 meters.

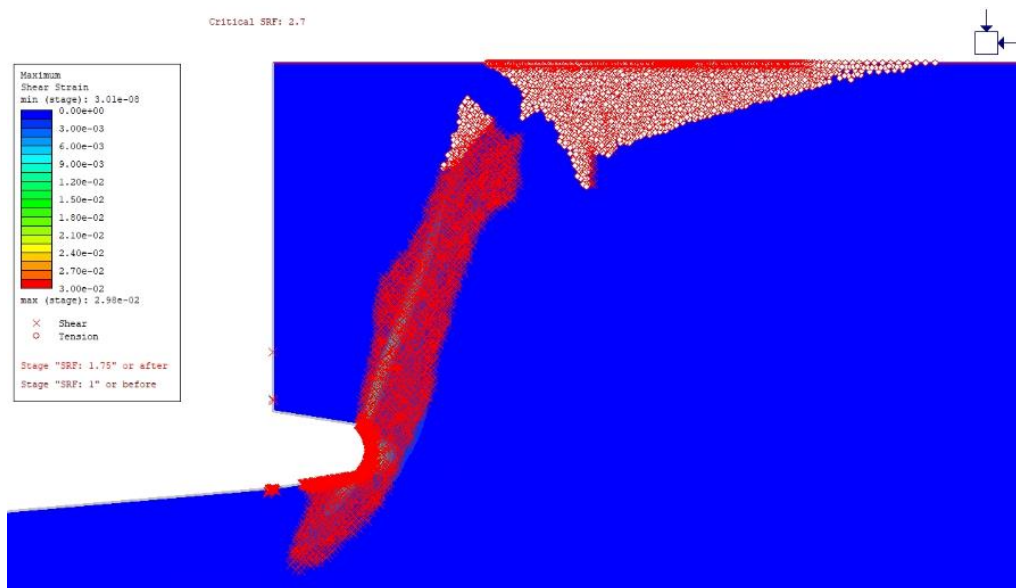


Figure 49 Maximum shear strain and distribution of yielded stresses of homogeneous vertical cliffs with 5 meters notch depth – Cliff height of 20 meters.

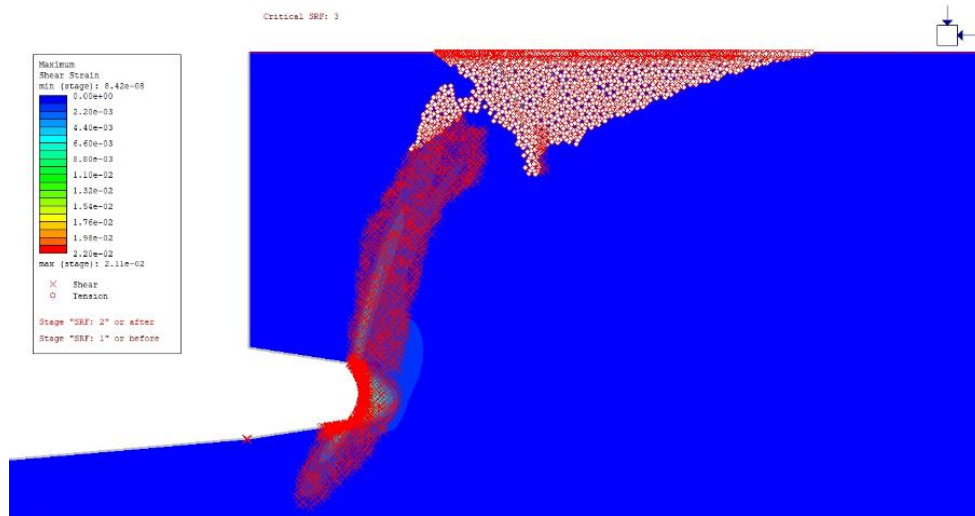


Figure 50 Maximum shear strain and distribution of yielded stresses of homogeneous vertical cliffs with 5 meters notch depth – Cliff height of 15 meters.

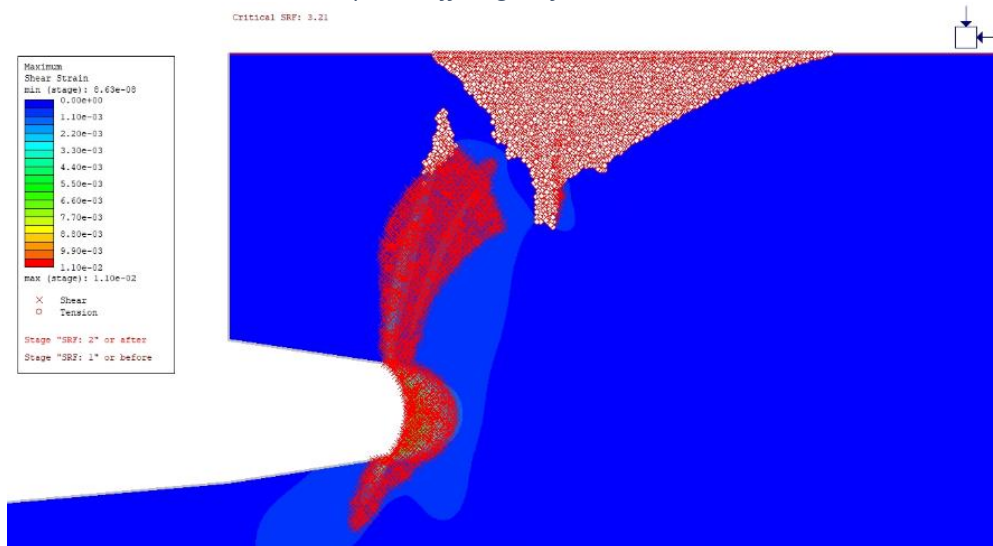


Figure 51 Maximum shear strain and distribution of yielded stresses of homogeneous vertical cliffs with 5 meters notch depth – Cliff height of 10 meters.

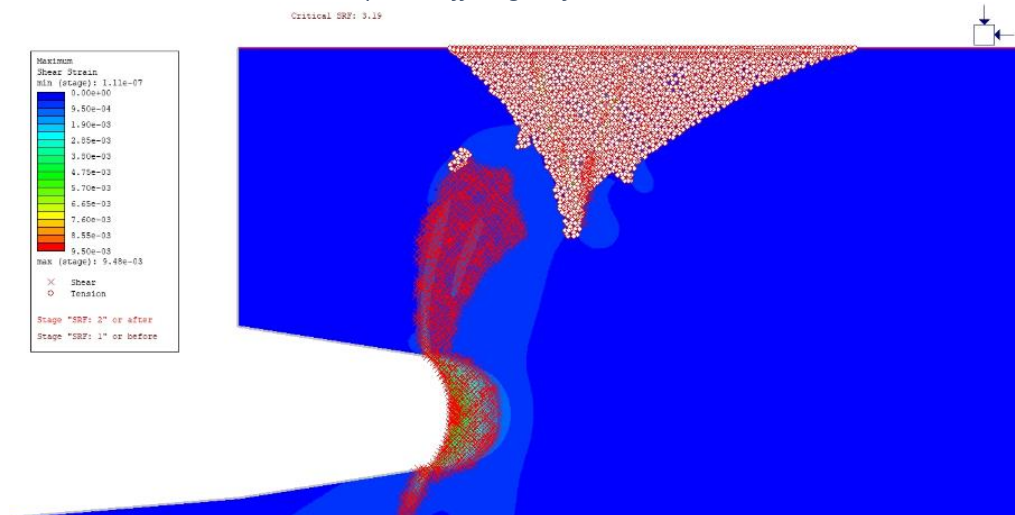


Figure 52 Maximum shear strain and distribution of yielded stresses of homogeneous vertical cliffs with 5 meters notch depth – Cliff height of 8.5 meters.

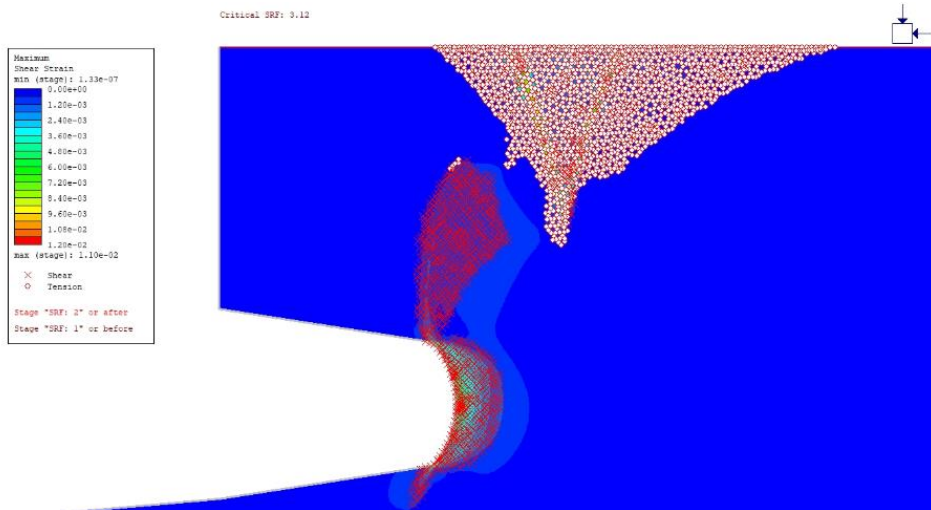


Figure 53 Maximum shear strain and distribution of yielded stresses of homogeneous vertical cliffs with 5 meters notch depth – Cliff height of 7.5 meters.

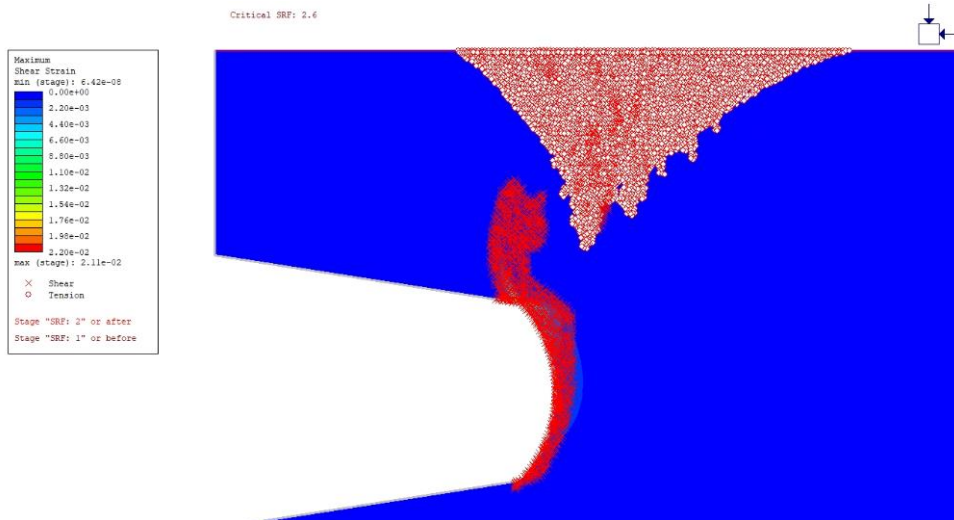


Figure 54 Maximum shear strain and distribution of yielded stresses of homogeneous vertical cliffs with 5 meters notch depth – Cliff height of 5 meters.

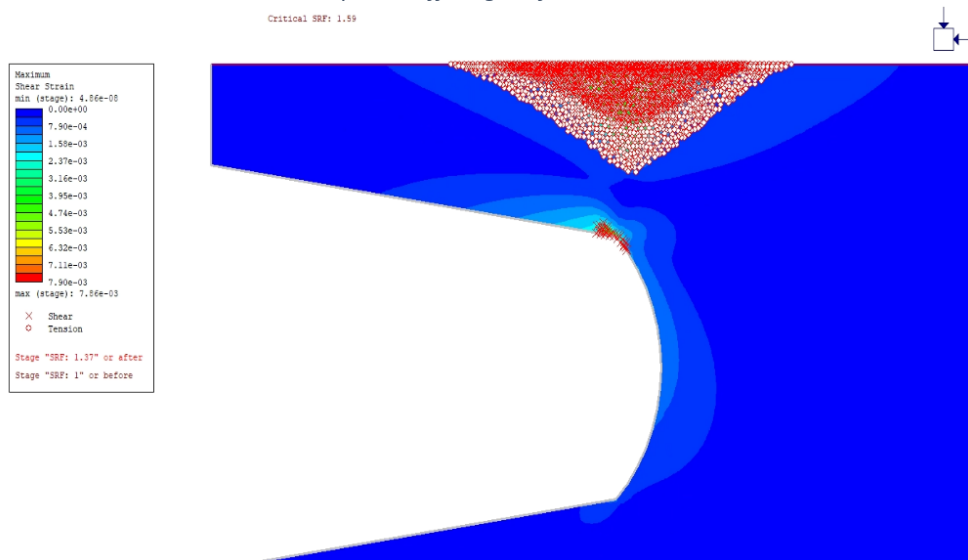


Figure 55 Maximum shear strain and distribution of yielded stresses of homogeneous vertical cliffs with 5 meters notch depth – Cliff height of 3 meters.

## 9.2 Appendix B: Numerical Results of Homogeneous Inclination Cliffs without Joint.

### 9.2.1 B1 : Maximum shear strain of homogeneous inclination cliffs with notch depths of 3m, 5m, 7m, and 10m.

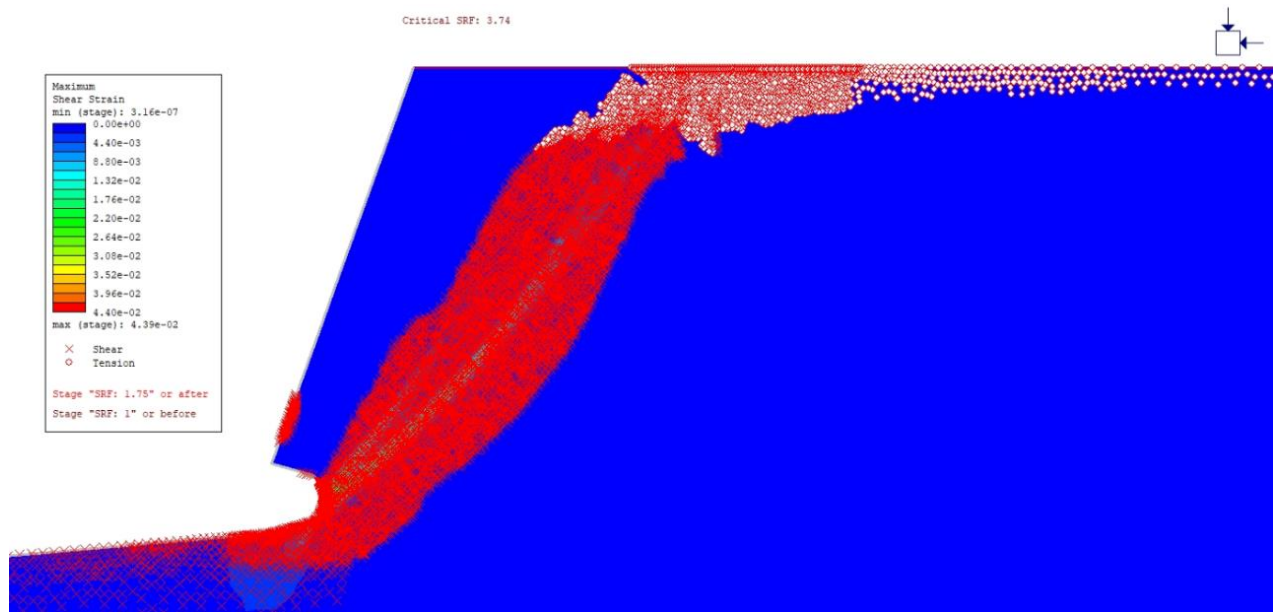


Figure 56 Maximum shear strain and distribution of yielded stresses of homogeneous inclination cliffs with 3 meters notch depth – Cliff height of 25 meters.

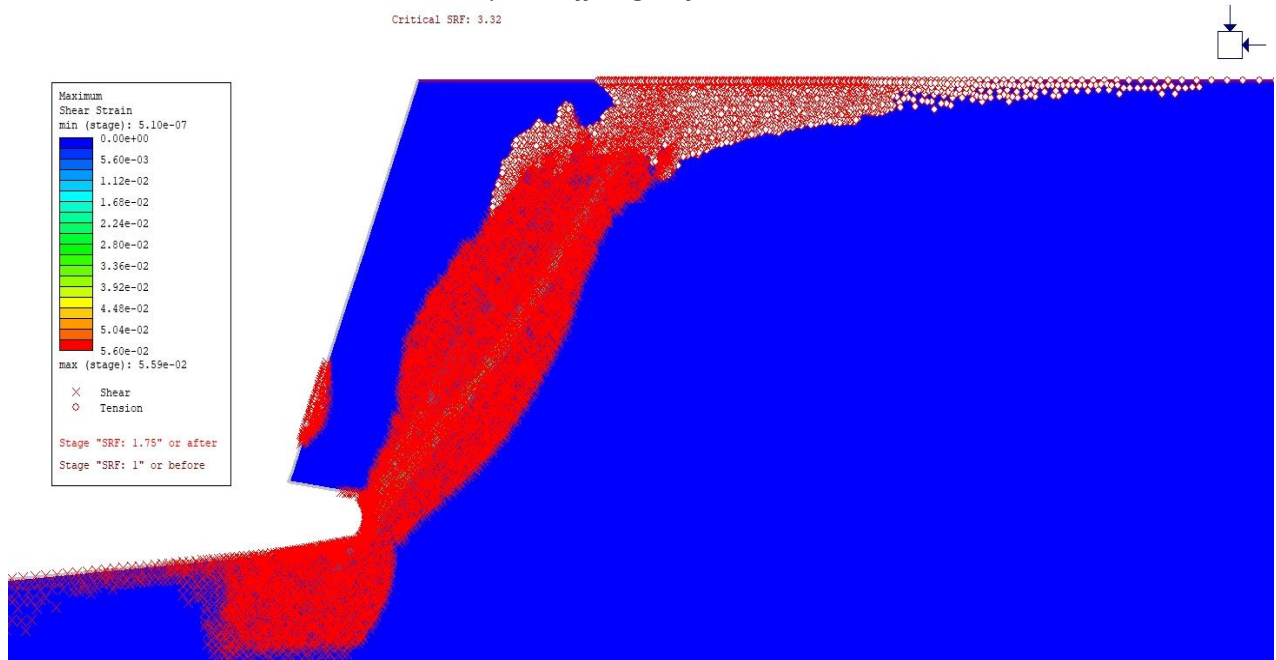


Figure 57 Maximum shear strain and distribution of yielded stresses of homogeneous inclination cliffs with 5 meters notch depth – Cliff height of 25 meters.

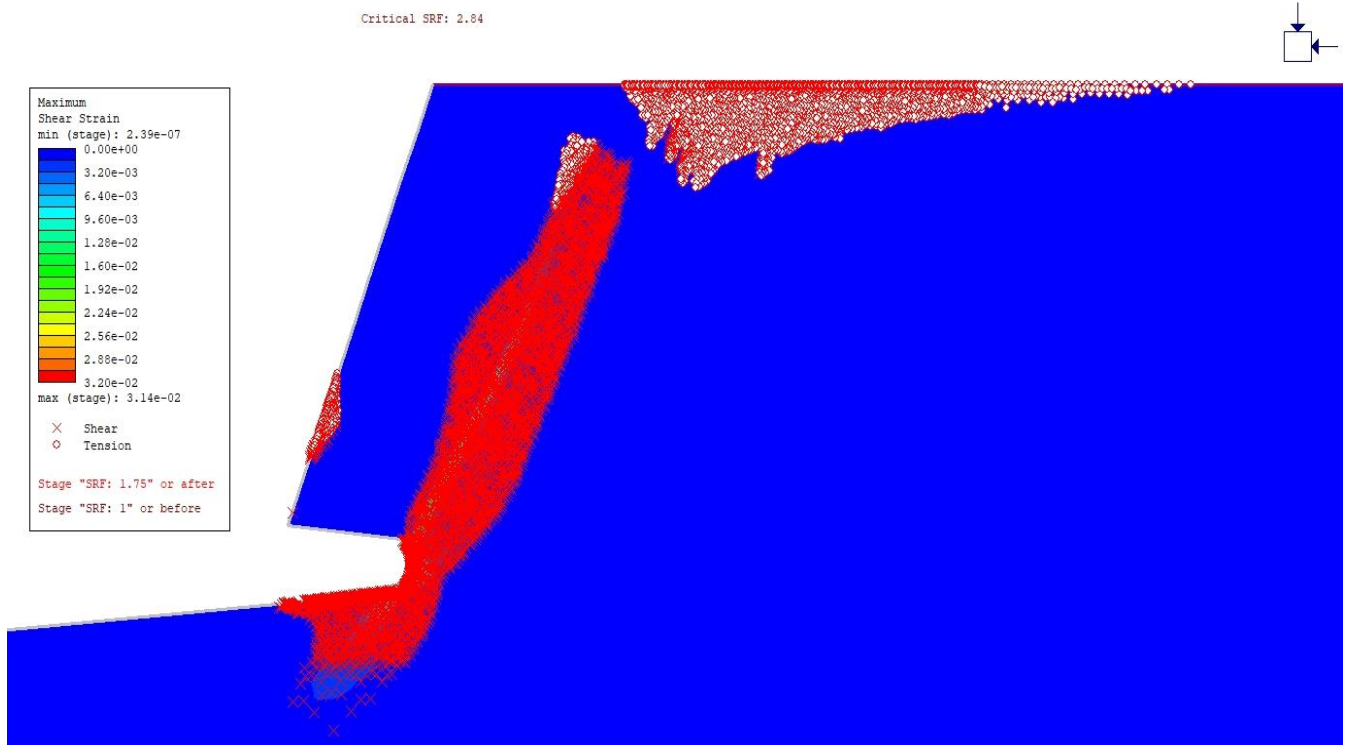


Figure 58 Maximum shear strain and distribution of yielded stresses of homogeneous inclination cliffs with 7 meters notch depth – Cliff height of 25 meters.

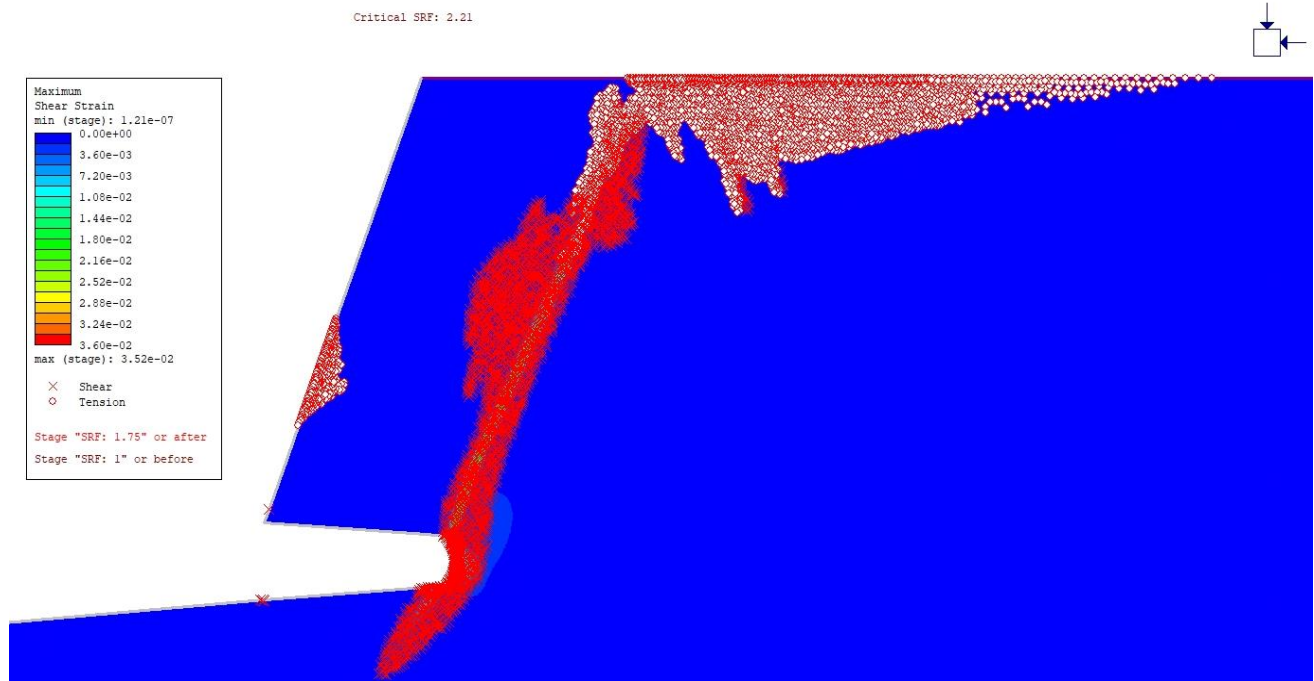


Figure 59 Maximum shear strain and distribution of yielded stresses of homogeneous inclination cliffs with 10 meters notch depth – Cliff height of 25 meters.

## 9.3 Appendix C: Numerical Results of Homogeneous Vertical Cliffs with joint

### 9.3.1 C1 : Maximum shear strain of homogeneous vertical cliffs with notch depth of 5m

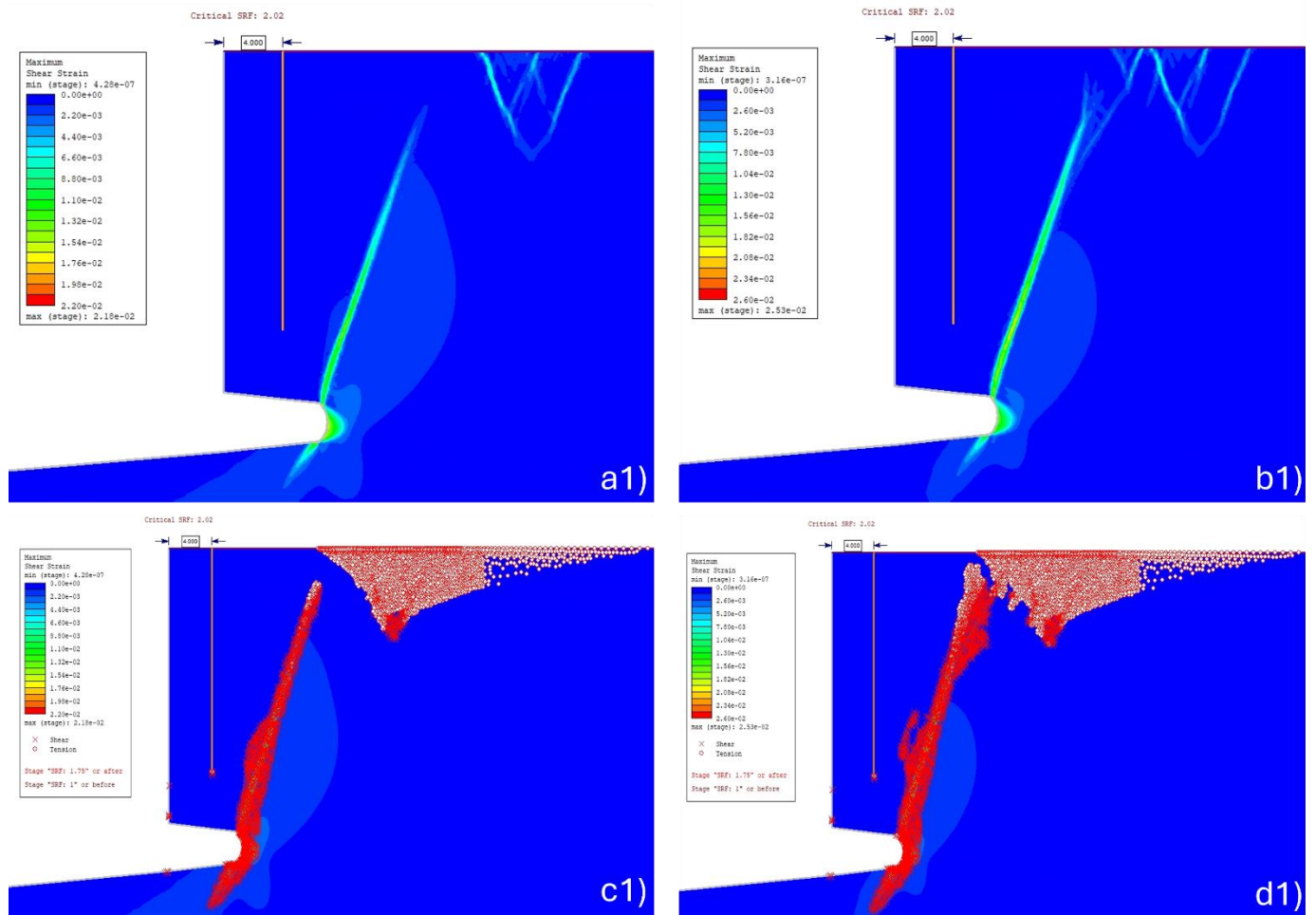


Figure 60 The joints 18.75 meters deep are located at varying horizontal distances from the cliff edge. The height of the cliff is 25 meters and the depth of the notch is 7 meters: a1-b1) maximum shear strain contours of the horizontal distance for the vertical joint at a distance  $d=4$  meters from the cliff face are at SRF 2.02, and 2.03 respectively; c1-d1) distribution of yielded elements for the vertical joint at a distance  $d=4$  meters from the cliff face are at SRF 2.02, and 2.03.



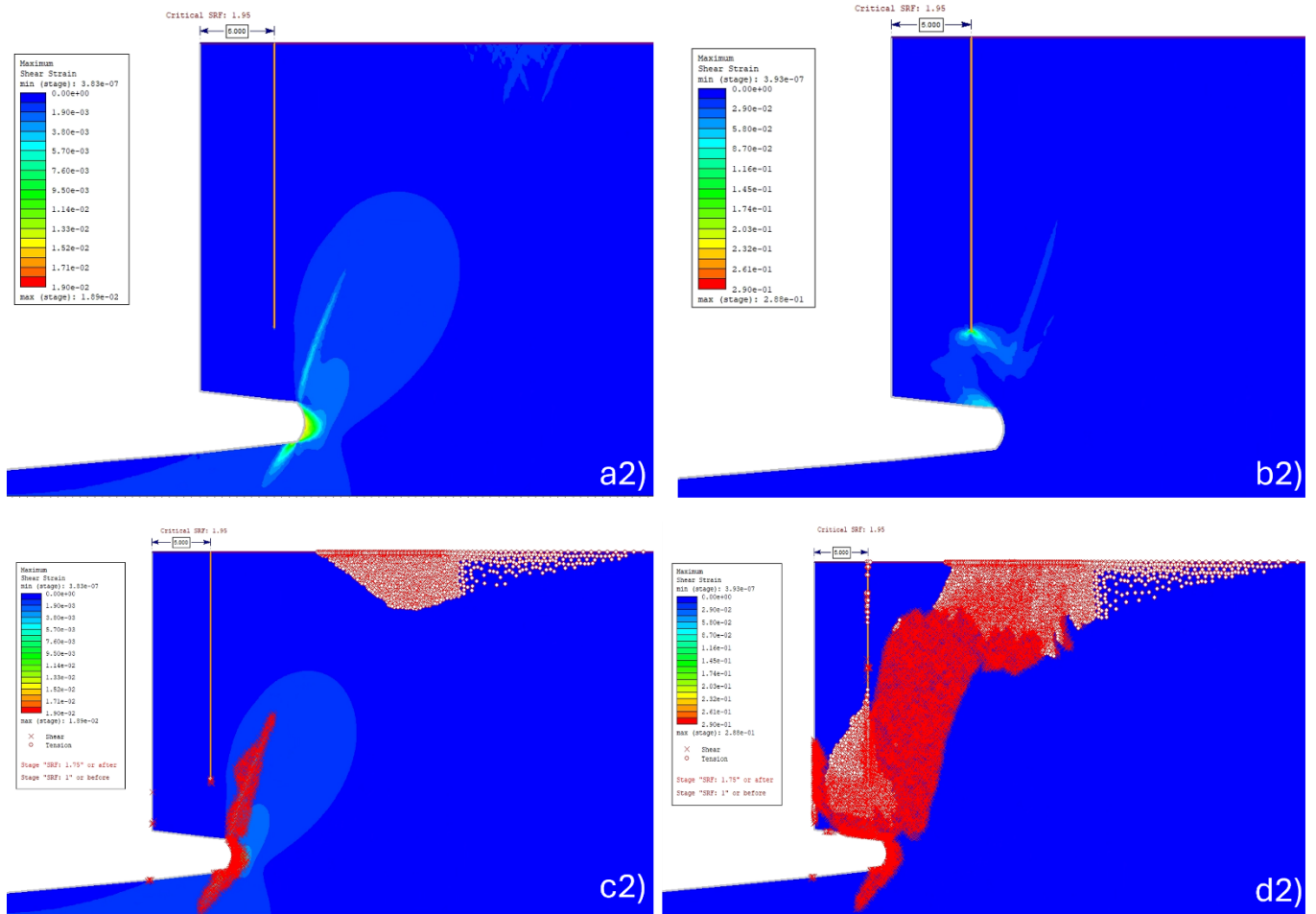


Figure 61 The joints 18.75 meters deep are located at varying horizontal distances from the cliff edge. The height of the cliff is 25 meters and the depth of the notch is 7 meters: a2-b2) maximum shear strain contours of the horizontal distance for the vertical joint at a distance  $d=5$  meters from the cliff face are at SRF 1.95, and 1.96 respectively; c2-d2) distribution of yielded elements for the vertical joint at a distance  $d=5$  meters from the cliff face are at SRF 1.95, and 1.96.

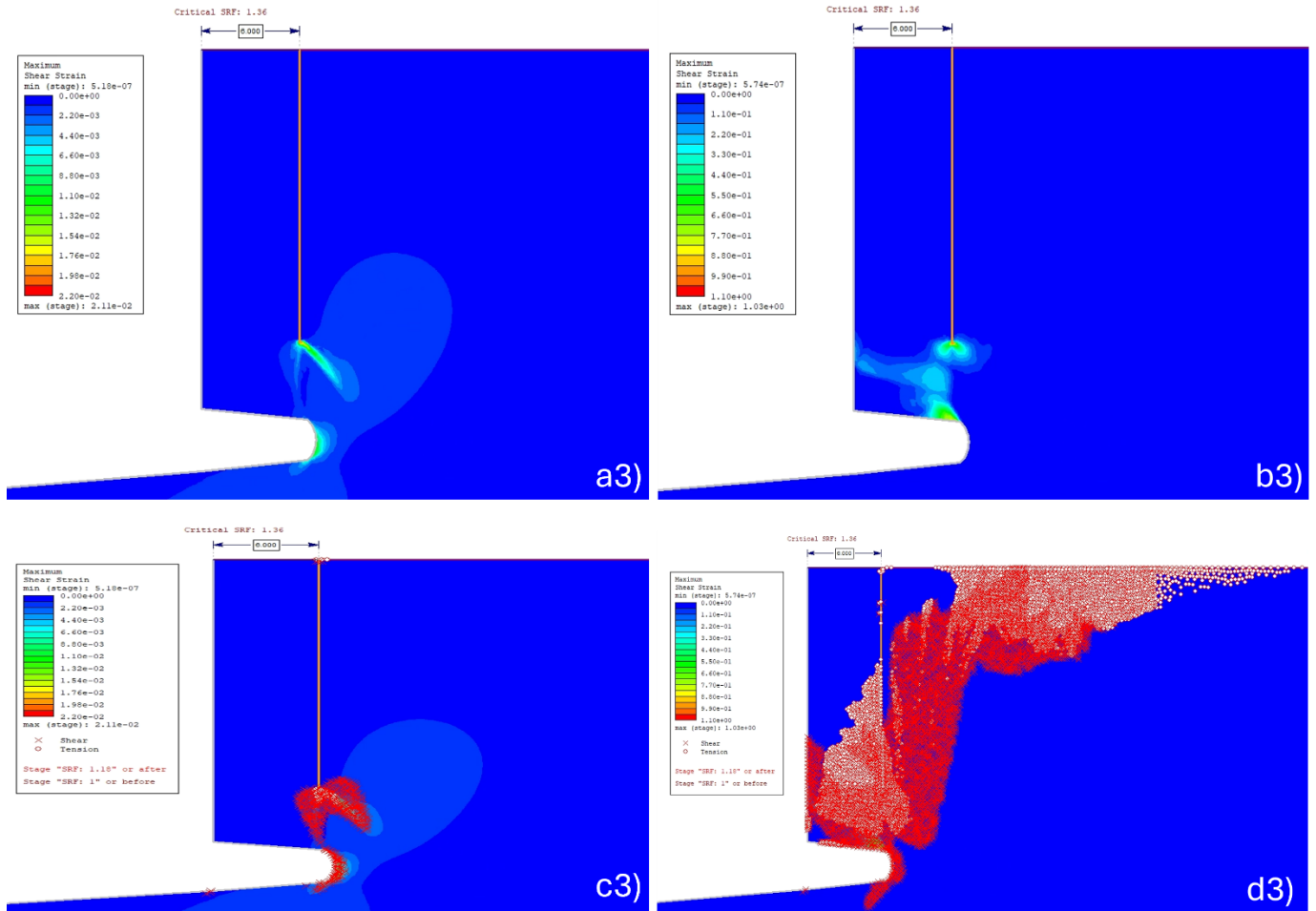


Figure 62 The joints 18.75 meters deep are located at varying horizontal distances from the cliff edge. The height of the cliff is 25 meters and the depth of the notch is 7 meters: a3-b3) maximum shear strain contours of the horizontal distance for the vertical joint at a distance  $d=6$  meters from the cliff face are at SRF 1.36, and 1.75 respectively; c3-d3) distribution of yielded elements for the vertical joint at a distance  $d=6$  meters from the cliff face are at SRF 1.36, and 1.75.

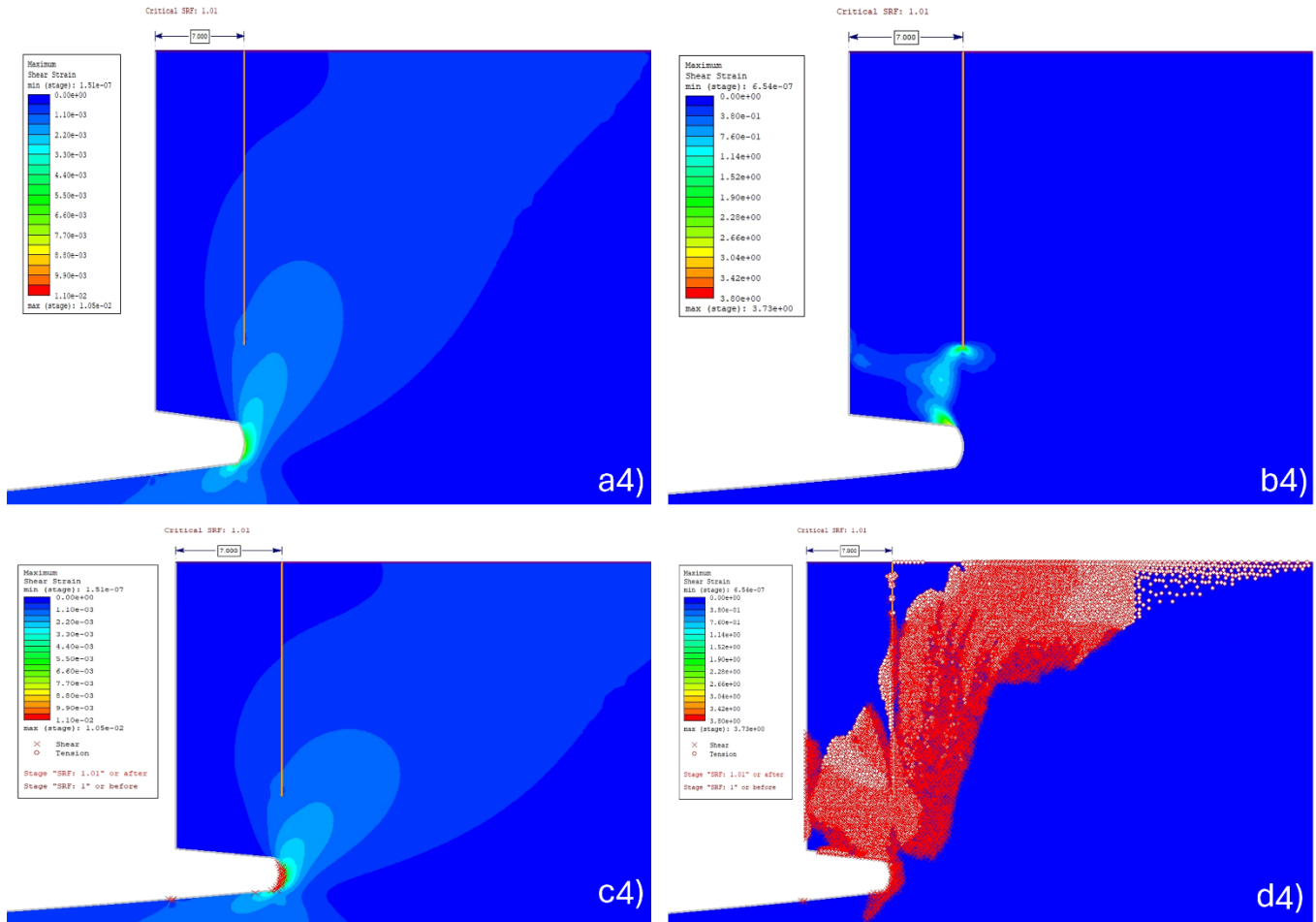


Figure 63 The joints 18.75 meters deep are located at varying horizontal distances from the cliff edge. The height of the cliff is 25 meters and the depth of the notch is 7 meters: a4-b4) maximum shear strain contours of the horizontal distance for the vertical joint at a distance  $d=7$  meters from the cliff face are at SRF 1.01, and 1.75 respectively; c4-d4) distribution of yielded elements for the vertical joint at a distance  $d=7$  meters from the cliff face are at SRF 1.01, and 1.75.

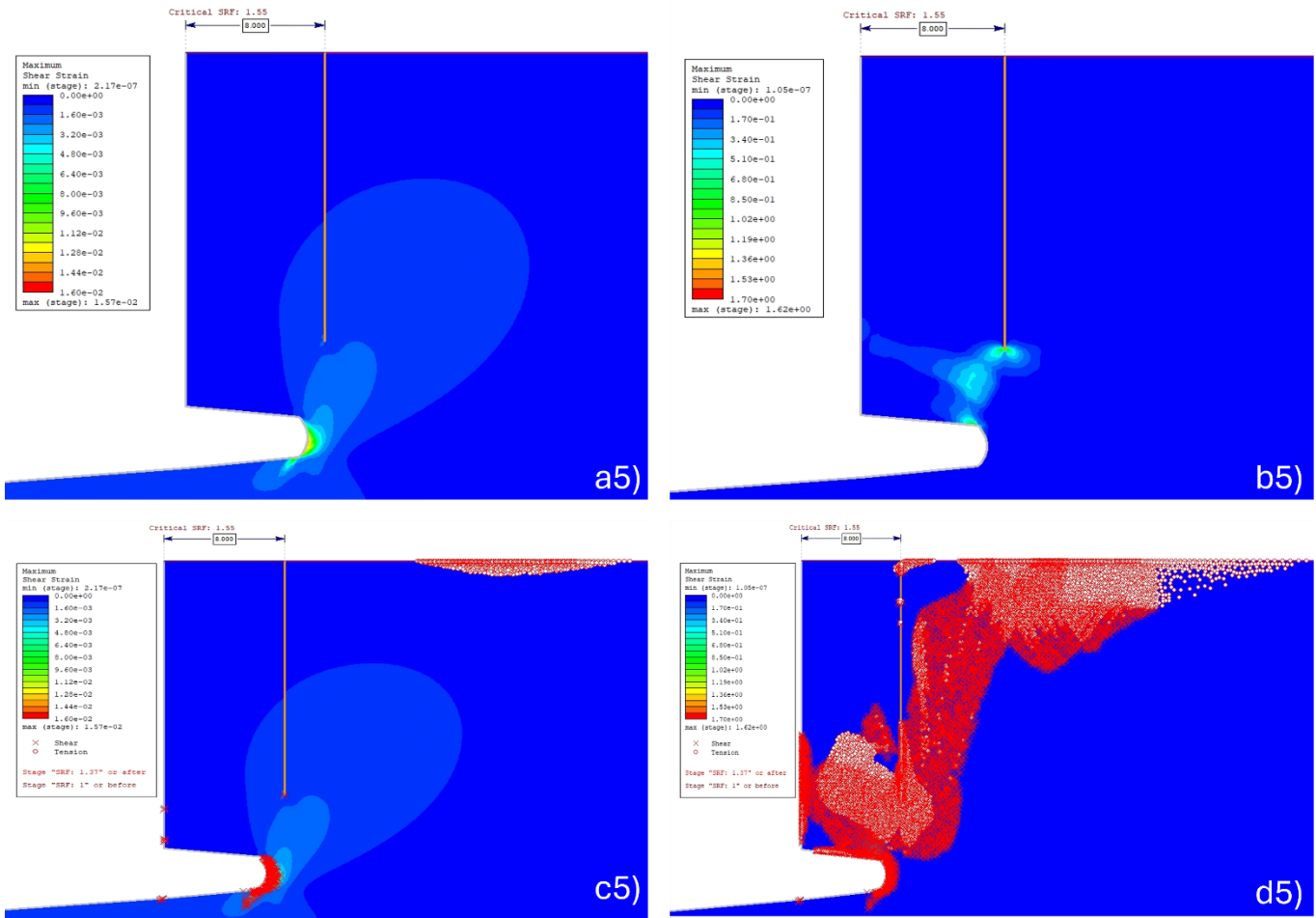


Figure 64 The joints 18.75 meters deep are located at varying horizontal distances from the cliff edge. The height of the cliff is 25 meters and the depth of the notch is 7 meters: a5-b5) maximum shear strain contours of the horizontal distance for the vertical joint at a distance  $d = 8$  meters from the cliff face are at SRP 1.55, and 1.56 respectively; c5-d5) distribution of yielded elements for the vertical joint at a distance  $d = 8$  meters from the cliff face are at SRP 1.55, and 1.56.

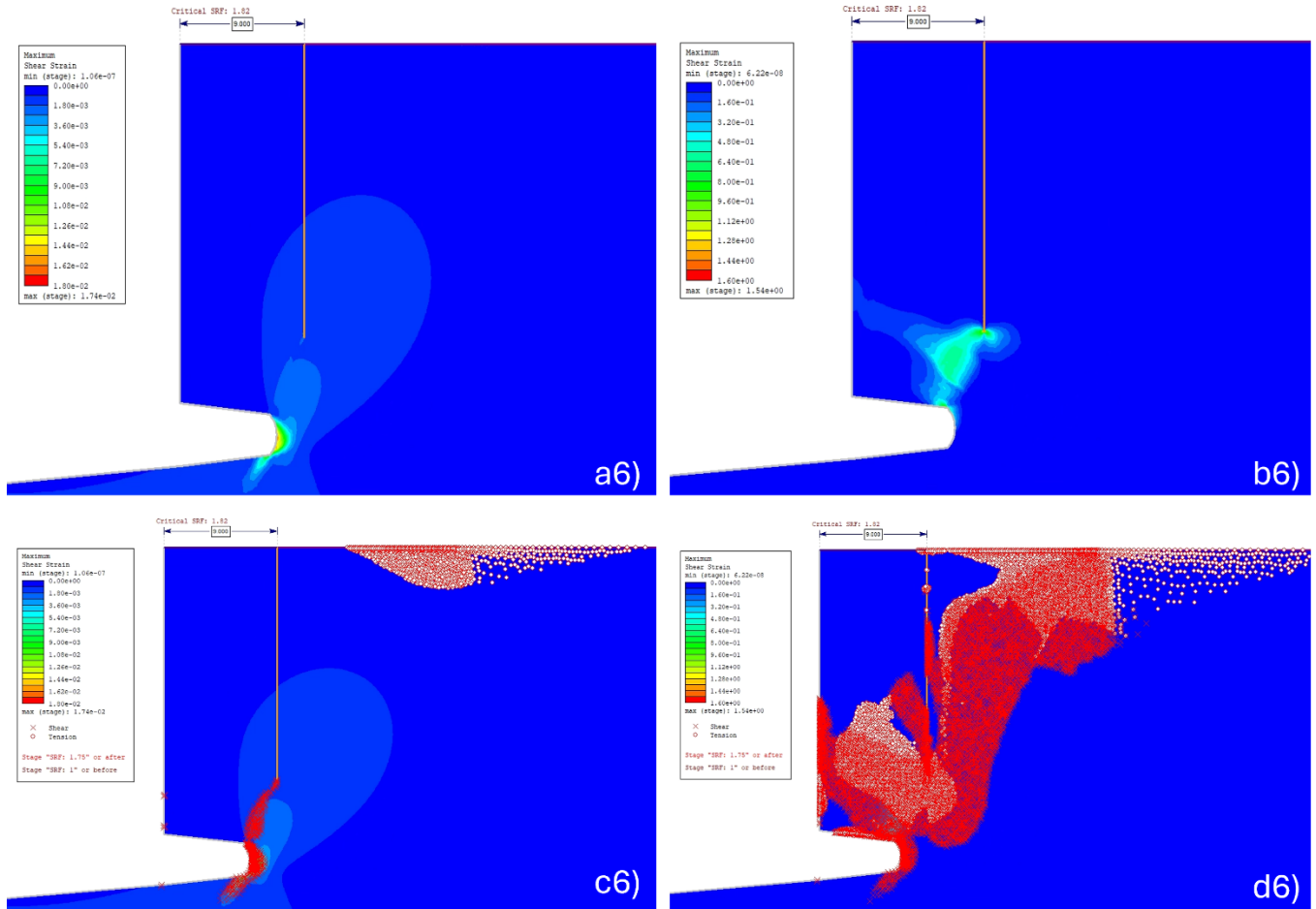


Figure 65 The joints 18.75 meters deep are located at varying horizontal distances from the cliff edge. The height of the cliff is 25 meters and the depth of the notch is 7 meters: a6-b6) maximum shear strain contours of the horizontal distance for the vertical joint at a distance  $d=9$  meters from the cliff face are at SRF 1.82, and 1.83 respectively; c6-d6) distribution of yielded elements for the vertical joint at a distance  $d=9$  meters from the cliff face are at SRF 1.82, and 1.83.

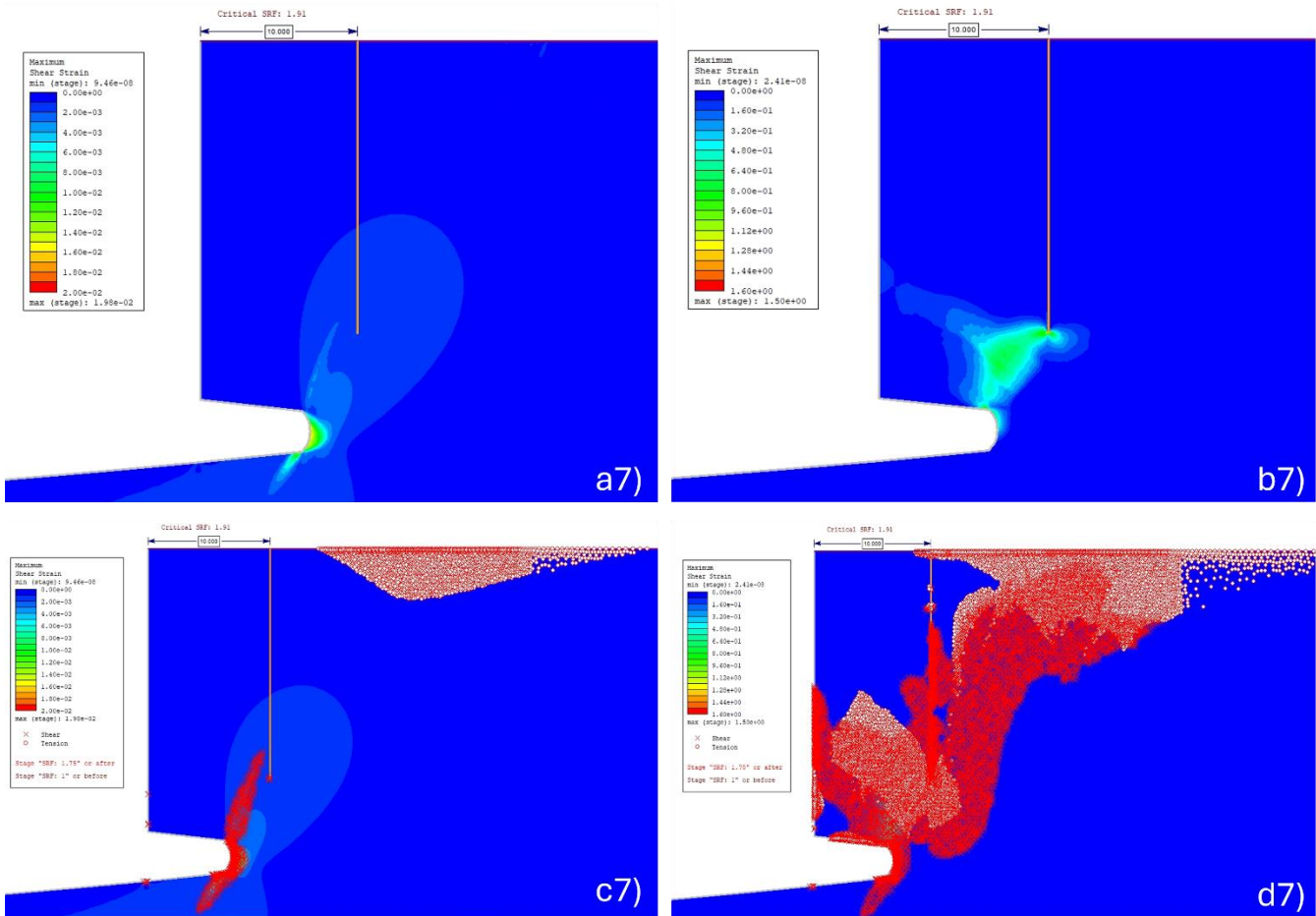


Figure 66 The joints 18.75 meters deep are located at varying horizontal distances from the cliff edge. The height of the cliff is 25 meters and the depth of the notch is 7 meters: a7-b7) maximum shear strain contours of the horizontal distance for the vertical joint at a distance  $d=10$  meters from the cliff face are at SRF 1.91, and 1.92 respectively; c7-d7) distribution of yielded elements for the vertical joint at a distance  $d=10$  meters from the cliff face are at SRF 1.91, and 1.92.

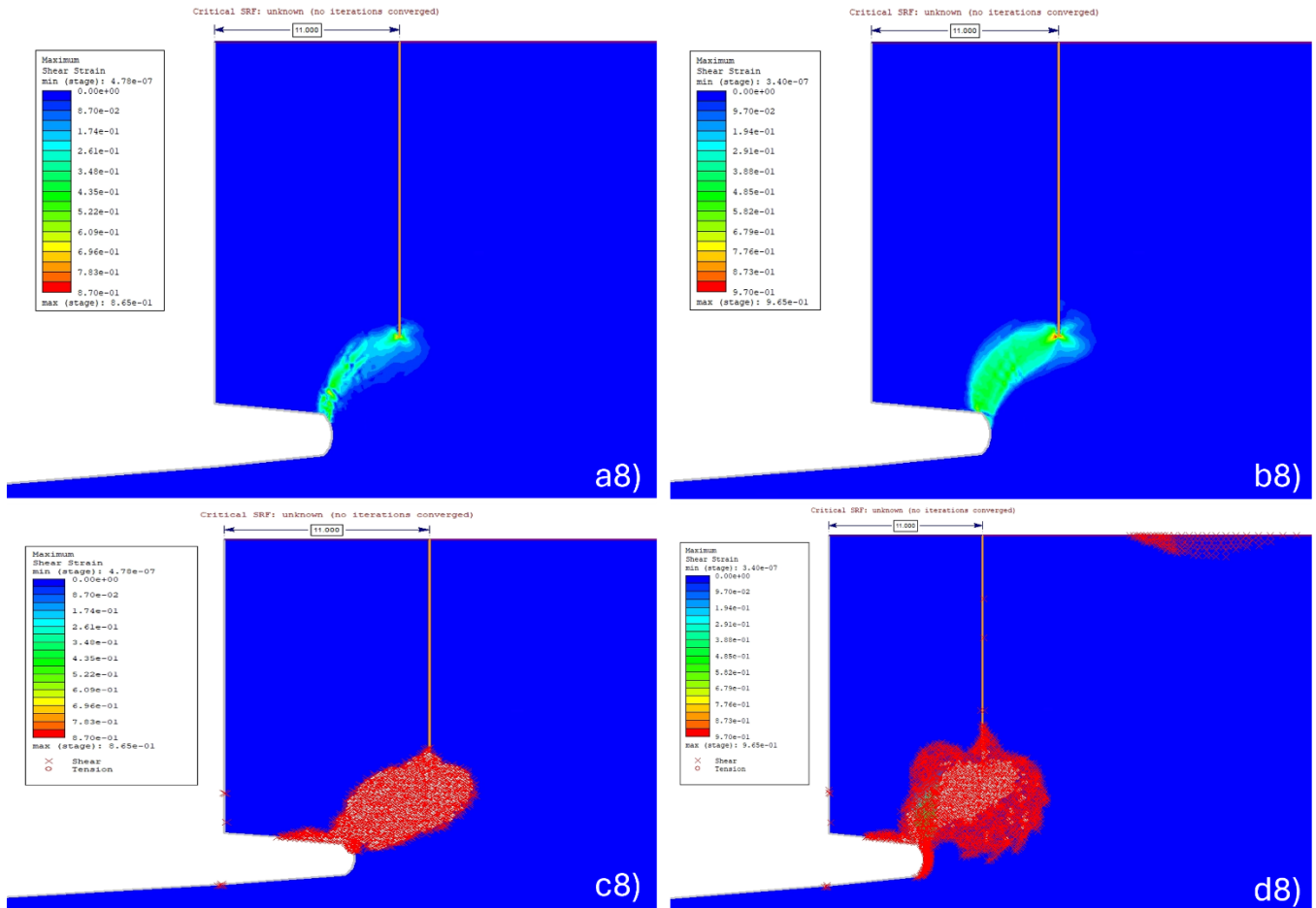


Figure 67 The joints 18.75 meters deep are located at varying horizontal distances from the cliff edge. The height of the cliff is 25 meters and the depth of the notch is 7 meters: a8-b8) maximum shear strain contours of the horizontal distance for the vertical joint at a distance  $d=11$  meters from the cliff face are at SRF 0.01, and 0.99 respectively; c8-d8) distribution of yielded elements for the vertical joint at a distance  $d=11$  meters from the cliff face are at SRF 0.01, and 0.99.

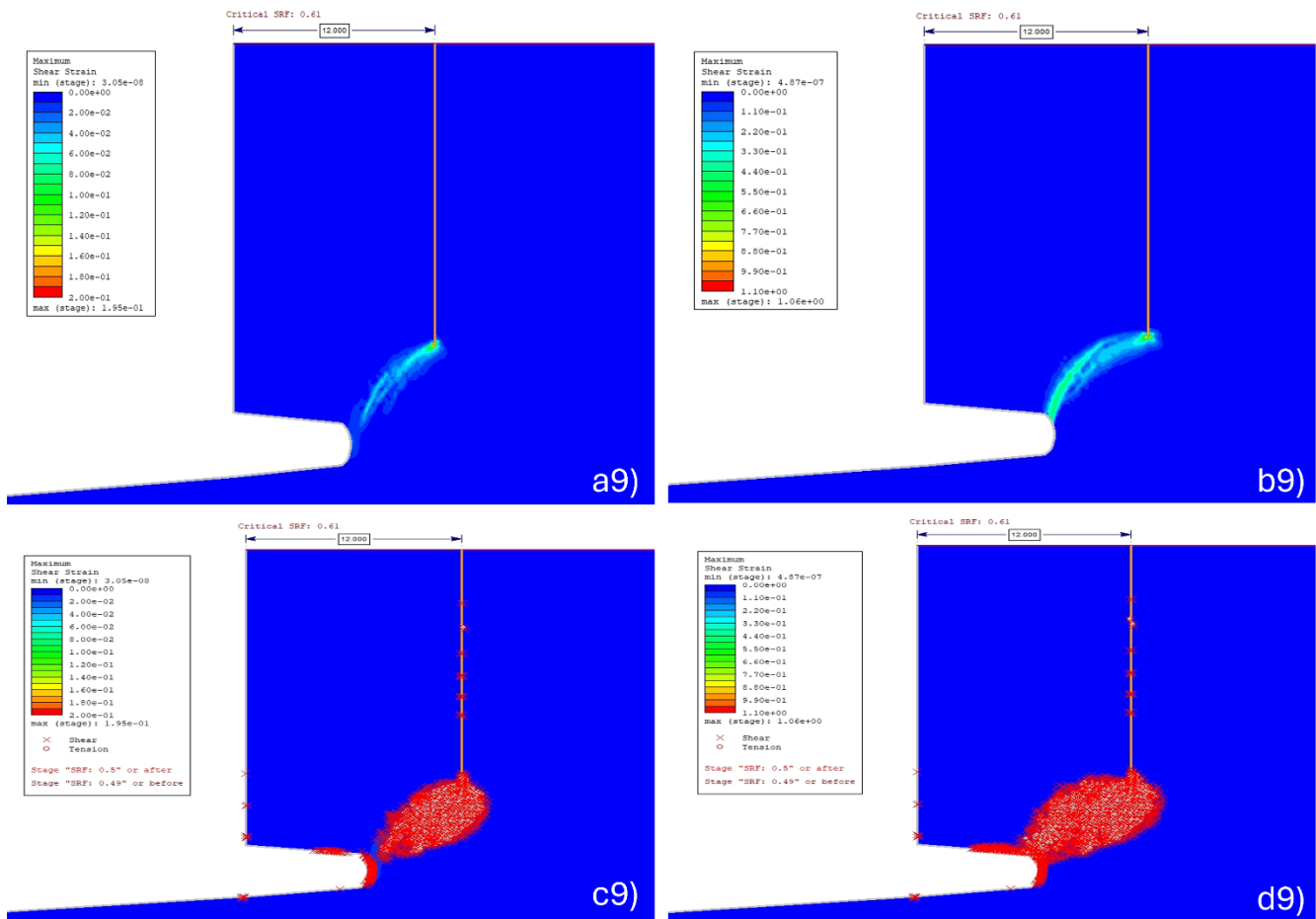


Figure 68 The joints 18.75 meters deep are located at varying horizontal distances from the cliff edge. The height of the cliff is 25 meters and the depth of the notch is 7 meters: a9-b9) maximum shear strain contours of the horizontal distance for the vertical joint at a distance  $d= 12$  meters from the cliff face are at SRF 0.61, and 0.62 respectively; c9-d9) distribution of yielded elements for the vertical joint at a distance  $d= 12$  meters from the cliff face are at SRF 0.61, and 0.62.



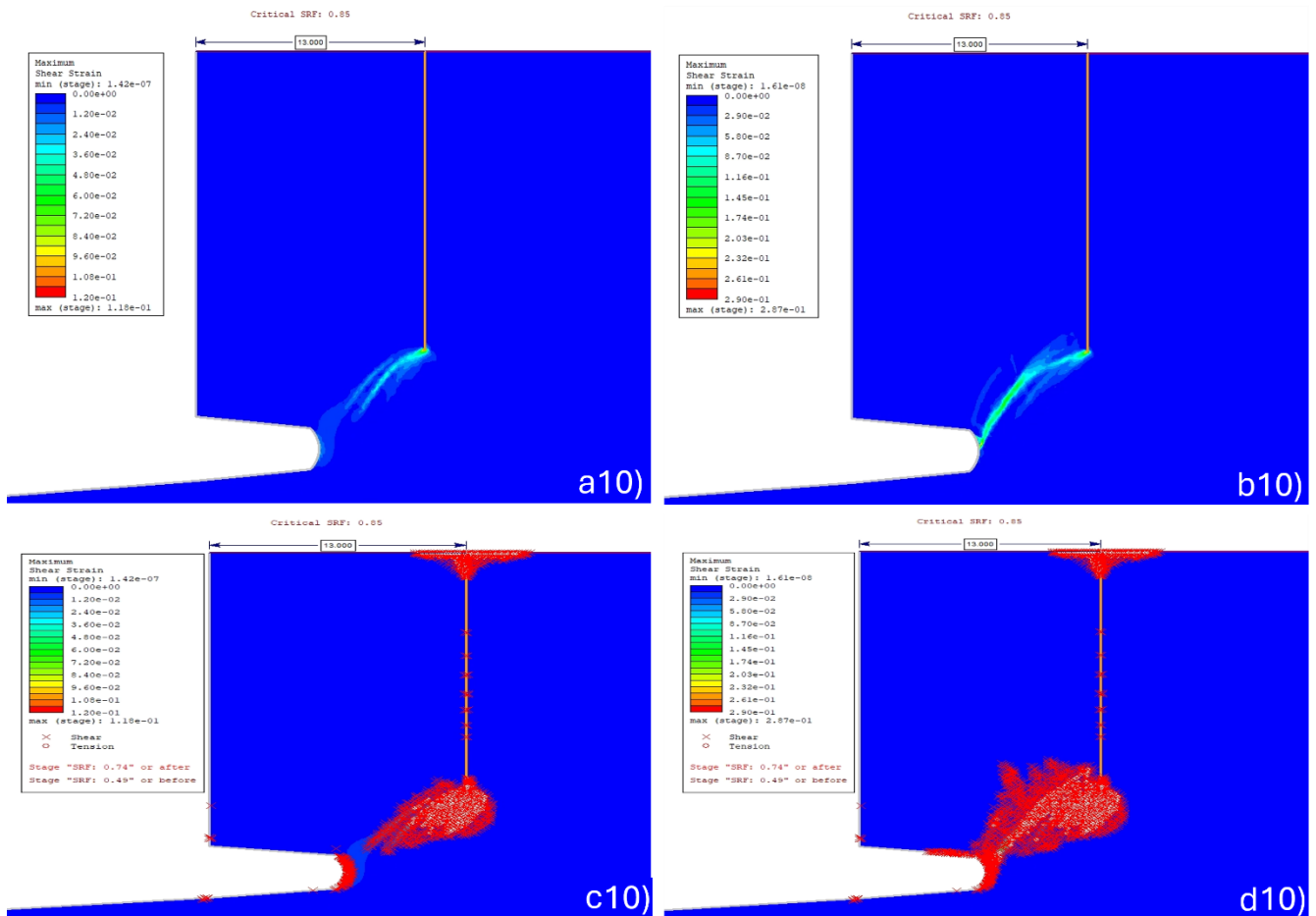


Figure 69 The joints 18.75 meters deep are located at varying horizontal distances from the cliff edge. The height of the cliff is 25 meters and the depth of the notch is 7 meters: a10-b10) maximum shear strain contours of the horizontal distance for the vertical joint at a distance  $d=13$  meters from the cliff face are at SRF 0.85, and 0.86; c10-d10) distribution of yielded elements for the vertical joint at a distance  $d=13$  meters from the cliff face are at SRF 0.85, and 0.86.

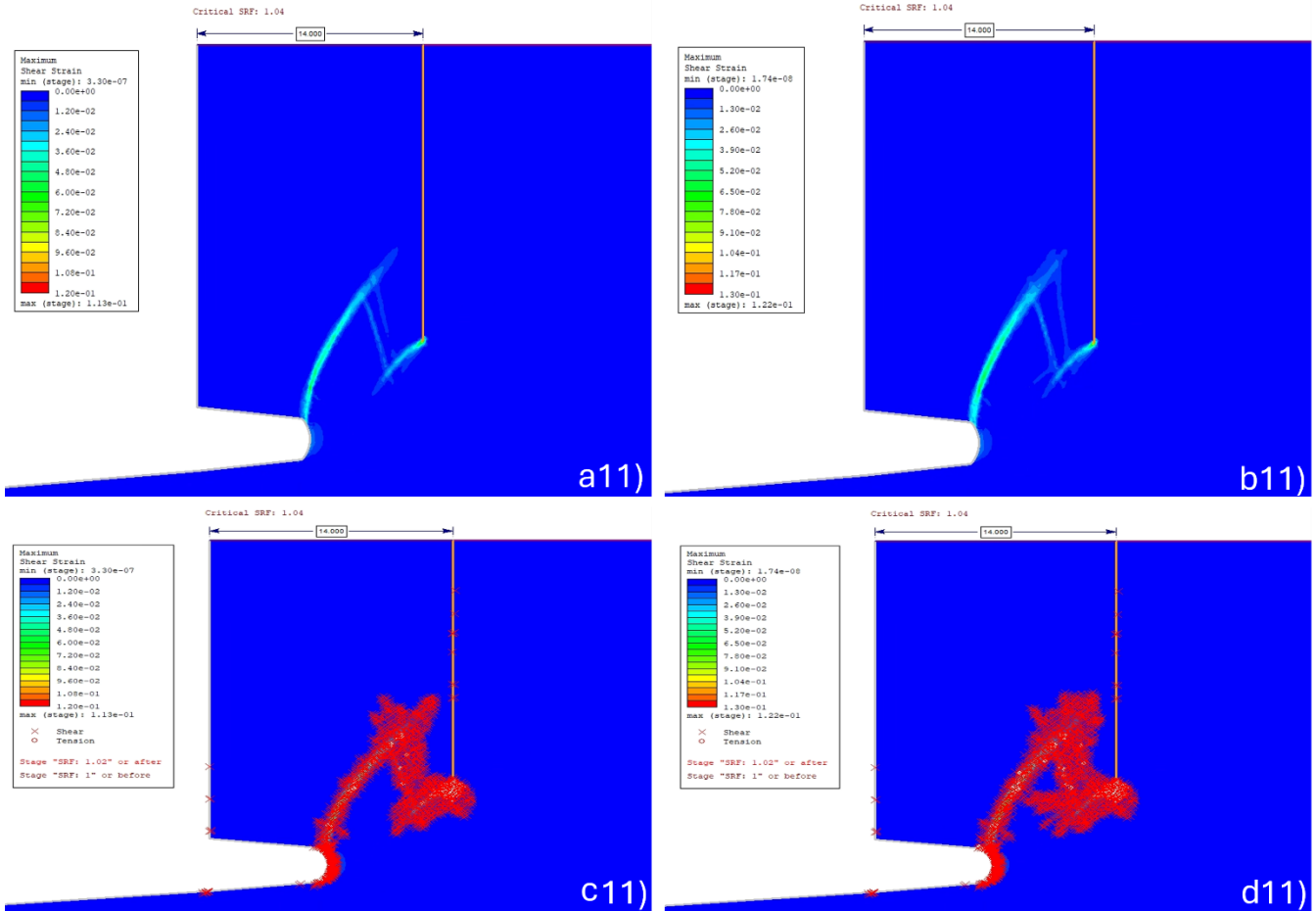


Figure 70 The joints 18.75 meters deep are located at varying horizontal distances from the cliff edge. The height of the cliff is 25 meters and the depth of the notch is 7 meters: a11-b11) maximum shear strain contours of the horizontal distance for the vertical joint at a distance  $d=14$  meters from the cliff face are at SRF 1.04, and 1.05; c11-d11) distribution of yielded elements for the vertical joint at a distance  $d=14$  meters from the cliff face are at SRF 1.04, and 1.05.

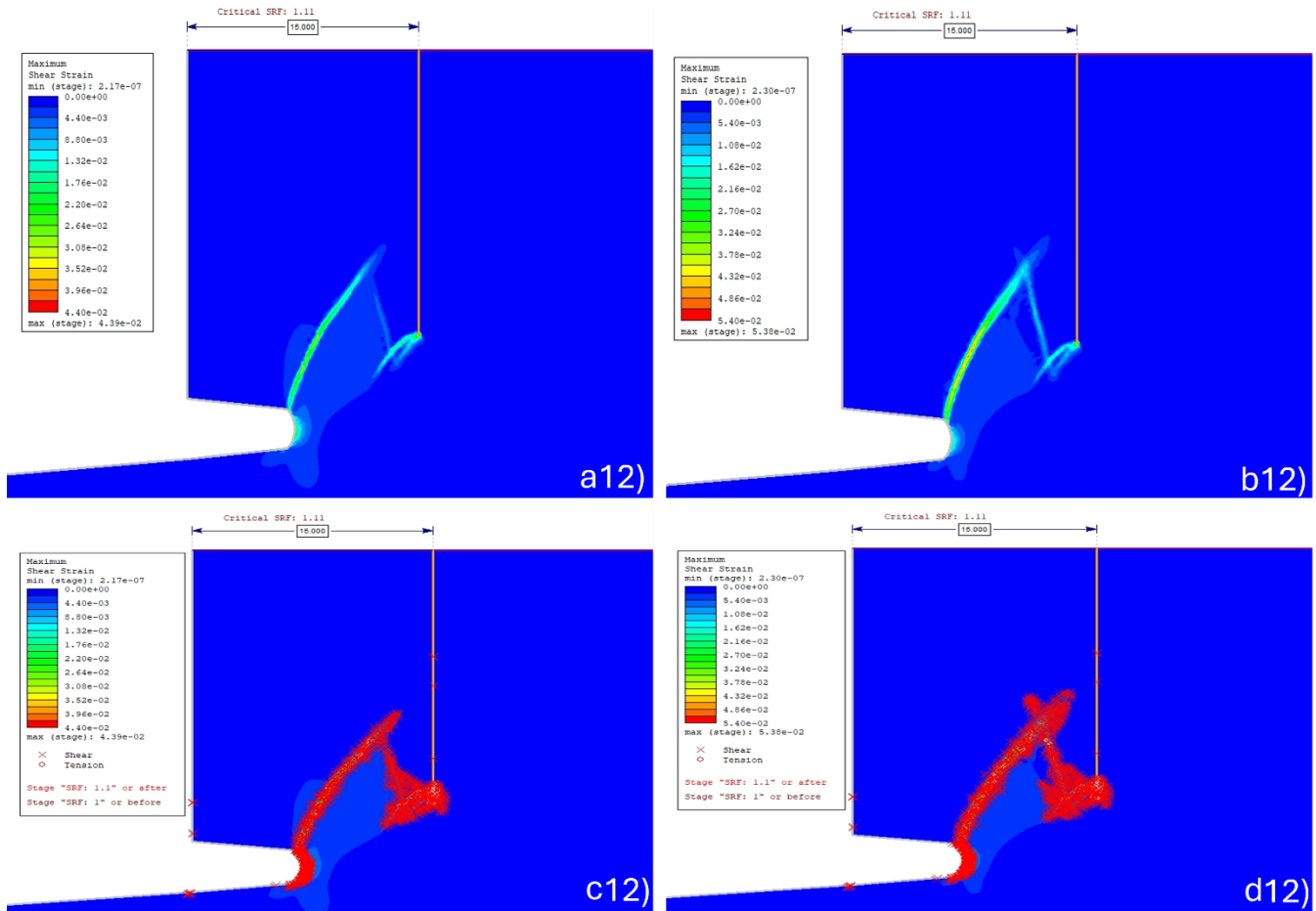


Figure 71 The joints 18.75 meters are located at varying horizontal distances from the cliff edge. The height of the cliff is 25 meters and the depth of the notch is 7 meters: a12-b12) maximum shear strain contours of the horizontal distance for the vertical joint at a distance  $d=15$  meters from the cliff face are at SRF 1.11, and 1.12; c12-d12) distribution of yielded elements for the vertical joint at a distance  $d=15$  meters from the cliff face are at SRF 1.11, and 1.12.

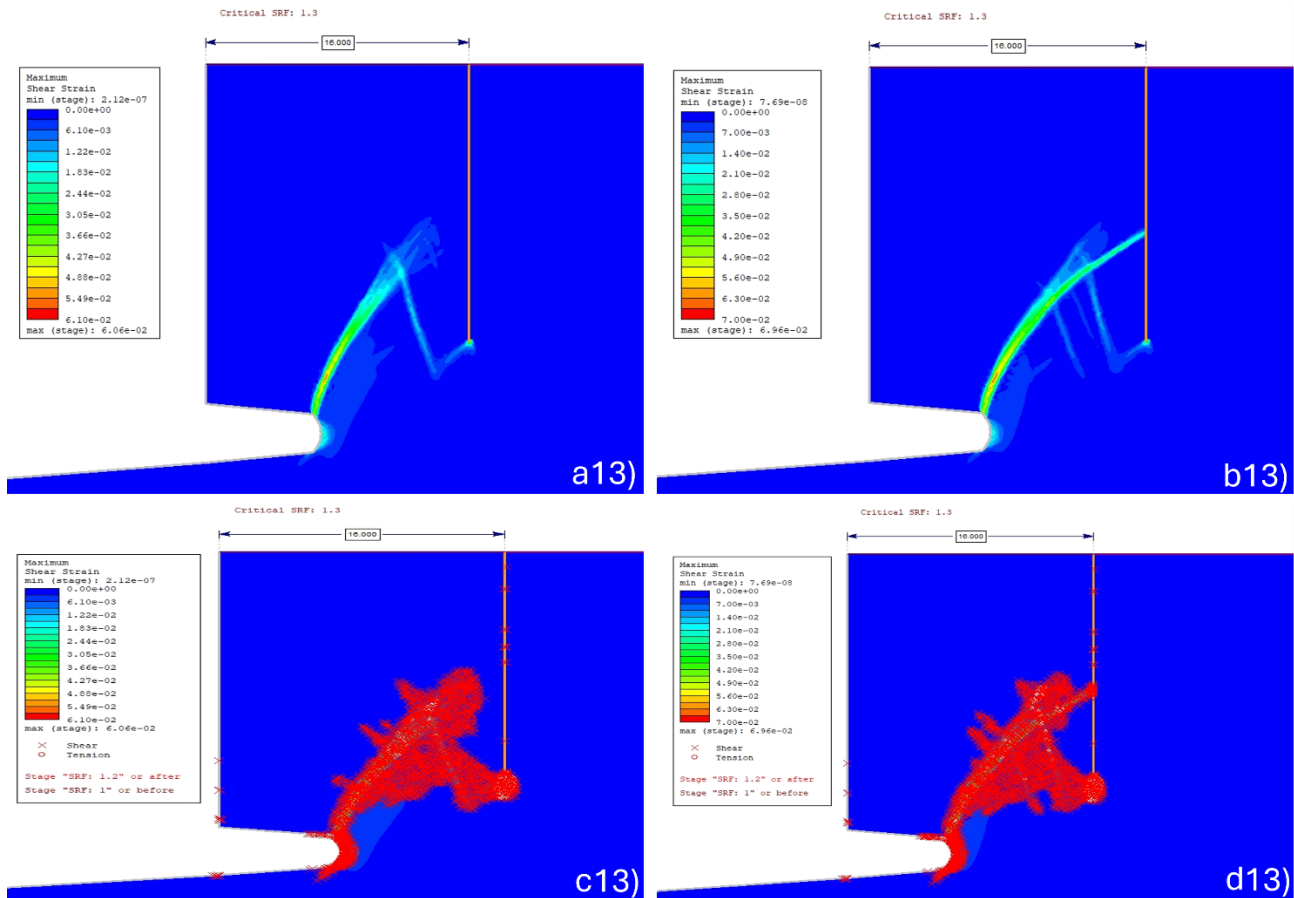


Figure 72 The joints 18.75 meters are located at varying horizontal distances from the cliff edge. The height of the cliff is 25 meters and the depth of the notch is 7 meters: a13-b13) maximum shear strain contours of the horizontal distance for the vertical joint at a distance  $d = 16$  meters from the cliff face are at SRF 1.30, and 1.31; c13-d13) distribution of yielded elements for the vertical joint at a distance  $d = 16$  meters from the cliff face are at SRF 1.30, and 1.31.

## 9.4 Appendix D: The modeling process in the Irazu software

### 9.4.1 Homogeneous vertical cliff without joint

#### 9.4.1.1 Geometry and Mesh Generation

- **Starting a 'New project' and determining the geometry.**

To create a new project, go to the **File** → **New Project** or click the **Create a New Project** button on the welcome screen. In the resulting *Mesh Creation window*, select the *'Import a CAD file(.dxf)'* option to import the DXF file using the AutoCAD 2000/2002 version of the geometry cliff model. Then tick the *'Auto identify and create surface'* option and keep the other default options unchanged in the *DXF Import Options window* (Figure 73). Alternatively, set the *Grid Size* to 10 (Figure 74) and insert the points by using the *Snap to Grid* function.

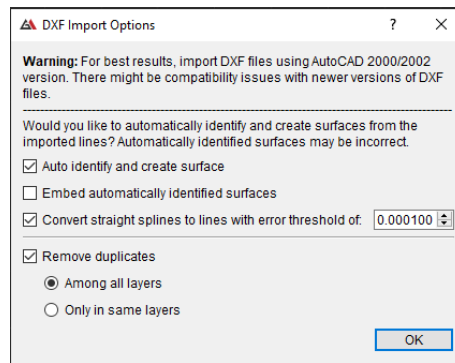


Figure 73 Setting the DXF import Options.

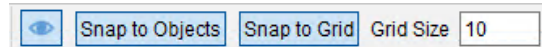


Figure 74 Setting the Grid Size to 10 and enabling the Snap to Grid function.

The geometry of the cliff model after importing the DXF file is shown in [Figure 75](#).

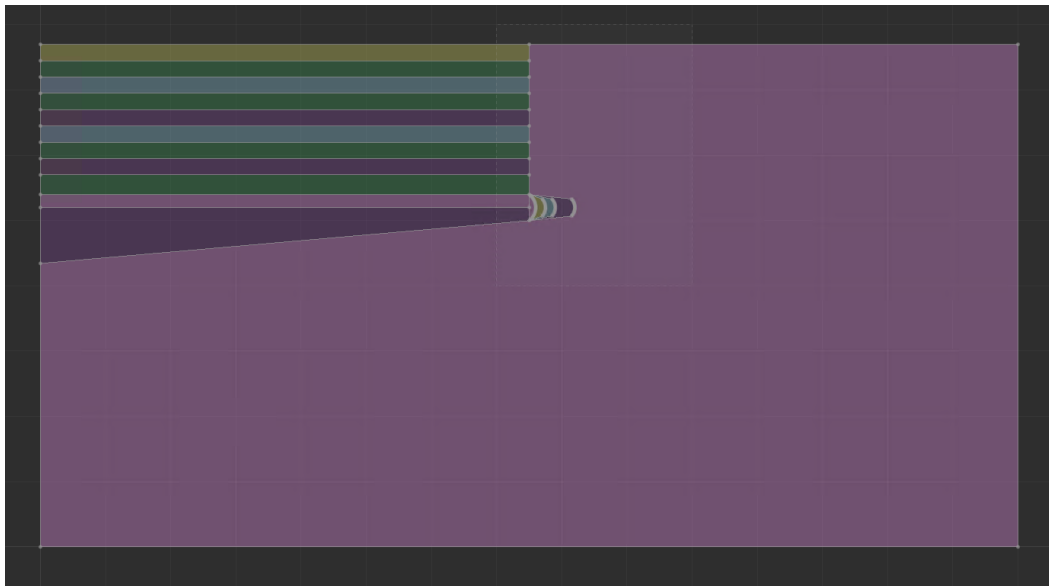


Figure 75 Geometry of the cliff model after importing the DXF file.

Double-click the surface and 'Cliff' as the Physical surface name and Surface element size to 1 in the *Edit surface* window as shown in [Figure 76](#).

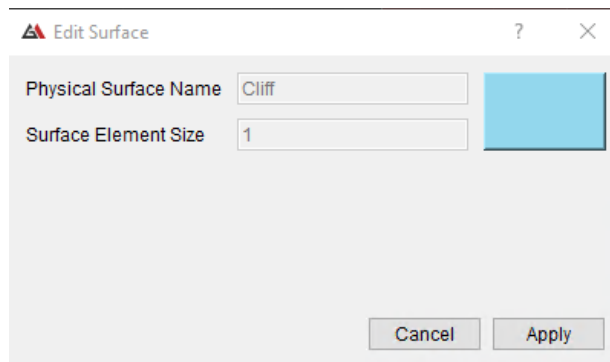




Figure 76 Setting the surface element size.

- **Define mesh refinement and meshing.**

Before meshing the model, it is necessary to specify an area of improved spatial resolution, that is a finer mesh, around the cliff surface where fracturing is expected to occur. This operation can be set in the **Mesh Refinement Fields** option. This option can assign a specific finite element size to a square region inside the model. Go to **Mesh** → **Define Mesh Refinement Fields**. After clicking on the Draw a Rectangle button (  ), draw a 40X30 square with the bottom right corner located at point (100,40). In the 'Edit Mesh Refinement Field' window, assign values equal to 0.4, 10, and 5 to the *Inner Element Size*, *Outer Element Size*, and *Transition Speed*, respectively, as shown in [Figure 77](#).

To create the mesh simply click on the **Mesh** button (  ). After doing so, the geometry will be meshed with triangular elements, as shown in [Figure 78](#).

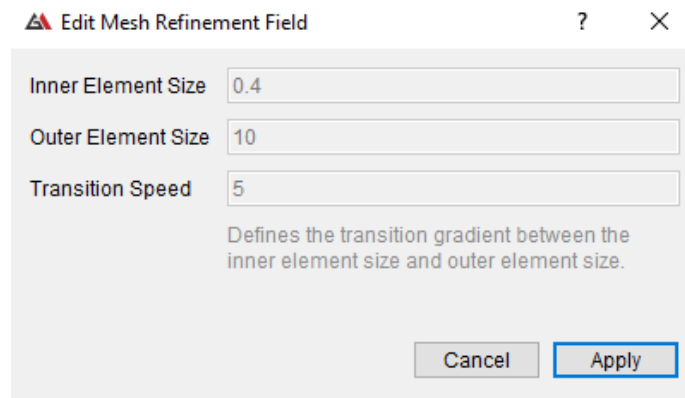


Figure 77 Setting the Mesh Refinement Field.

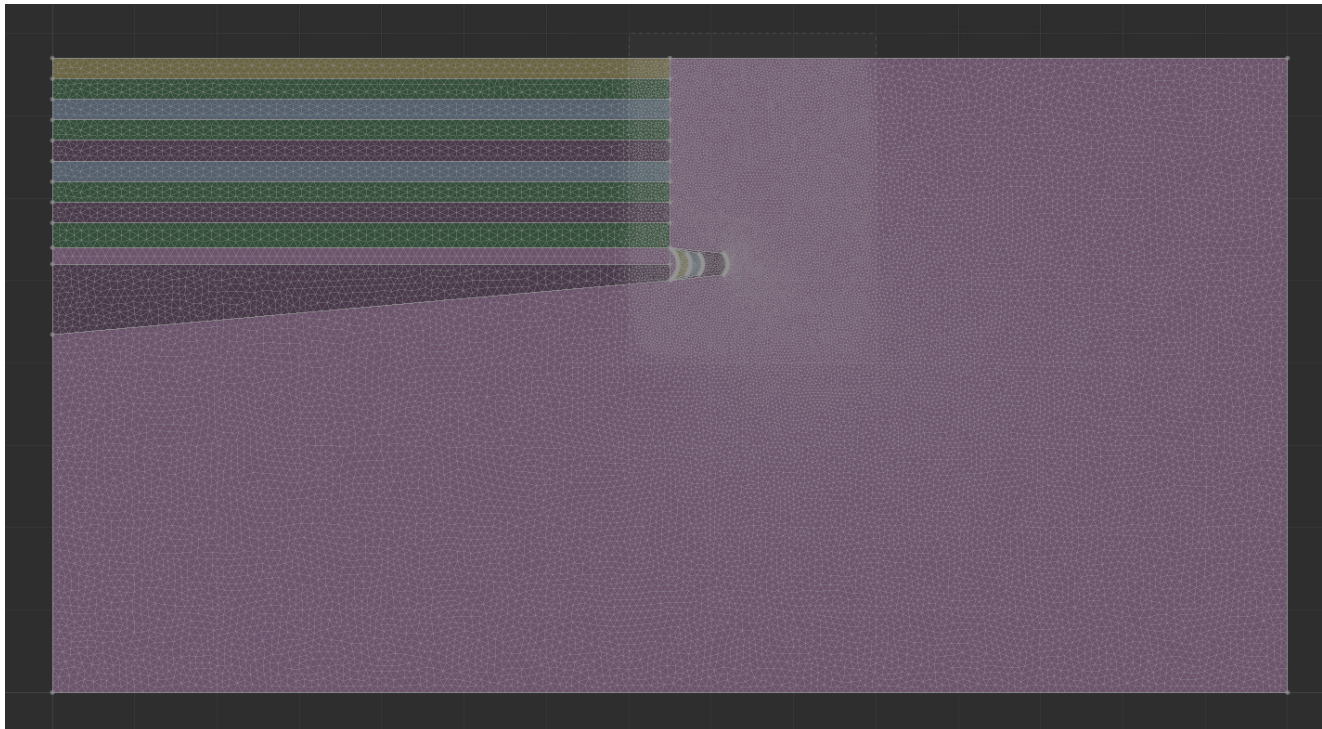



Figure 78 Final finite element mesh generated for the cliff model.

### 9.4.1.2 Model Construction with the Irazu User Interface

- **Using mesh for the project.**

Now click the Project Options (  ) button, specify a project name, and select the length units in which the mesh was created. For this model, the length units of meters (m) were used for the mesh generation. The corresponding mass and time units are kg and s, respectively (Figure 79). Additionally, enable the in-situ stress capability of *Irazu*, by checking the appropriate check box.

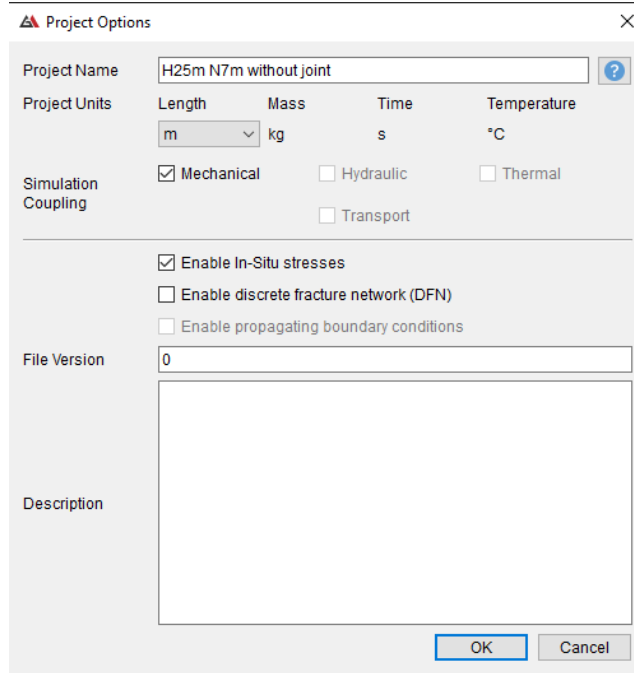


Figure 79 Specification of Project Options.

- **Specifying ‘Run Options’**

For this simulation, on the *Run Options* tab of the *Irazu User Interface*, the *Number of Time Steps* will be 2,500,000, the *Time Step Size* will be 2.1e-6 seconds and the *Output Frequency* will be 10000-time steps. *Gravity acceleration* is assumed equal to -9.81 m/s<sup>2</sup>. Enable the *FEM Run option* to allow the computation of the elastic stress field in the rock mass based on the previously defined in-situ stresses and the actual slope geometry. The *Run Options* tab with the above values specified is provided in Figure 80.

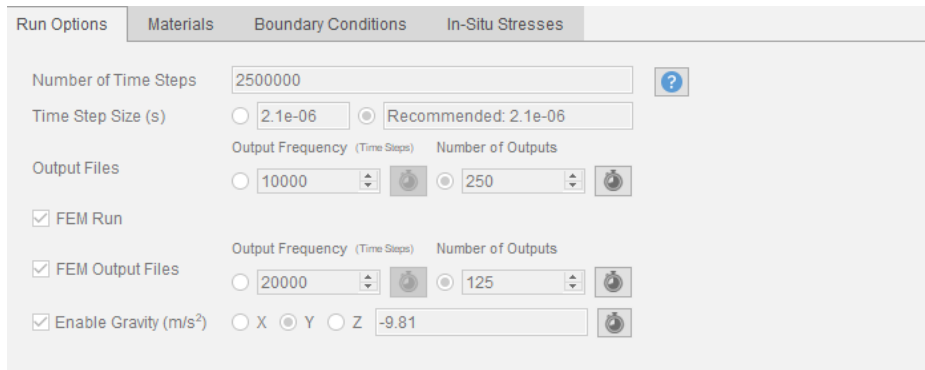

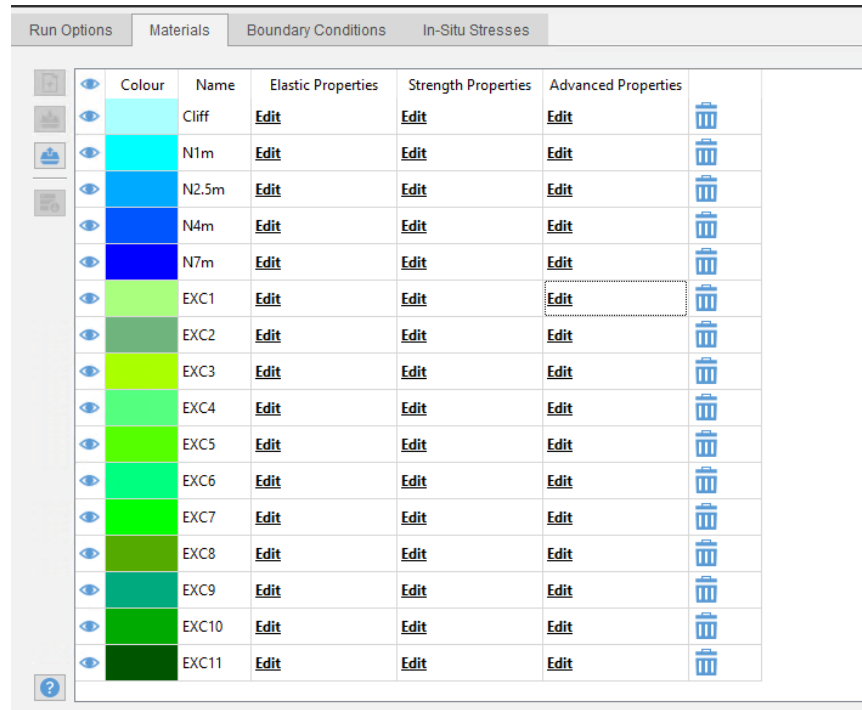


Figure 80 Setting run options in the Irazu User Interface.

- **Specifying and assigning properties for ‘Materials’.**

One material having the rock mass property will be modeled. To add material properties, switch to the *Materials* tab in the *Irazu User Interface* and click the **Plus** button (  ) to create the material. Name the material ‘Rock’ and assign a unique color to it, as shown in [Figure 81](#).

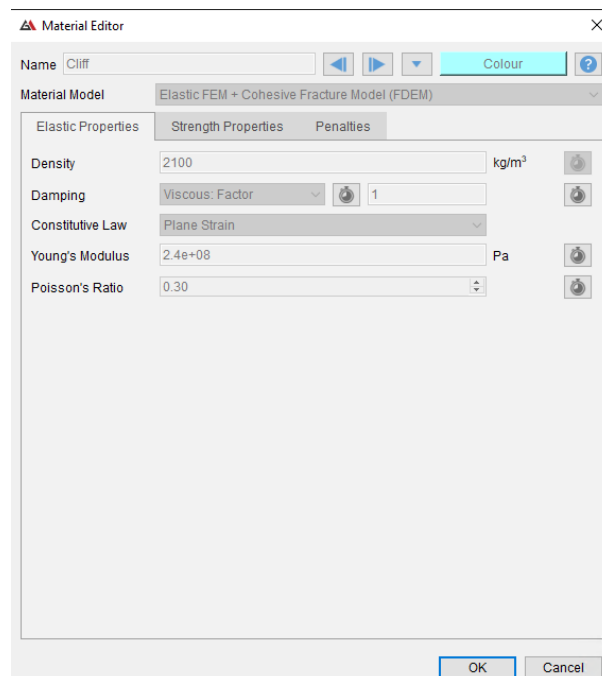


Run Options	Materials	Boundary Conditions	In-Situ Stresses		
Colour	Name	Elastic Properties	Strength Properties	Advanced Properties	
	Cliff	<a href="#">Edit</a>	<a href="#">Edit</a>	<a href="#">Edit</a>	
	N1m	<a href="#">Edit</a>	<a href="#">Edit</a>	<a href="#">Edit</a>	
	N2.5m	<a href="#">Edit</a>	<a href="#">Edit</a>	<a href="#">Edit</a>	
	N4m	<a href="#">Edit</a>	<a href="#">Edit</a>	<a href="#">Edit</a>	
	N7m	<a href="#">Edit</a>	<a href="#">Edit</a>	<a href="#">Edit</a>	
	EXC1	<a href="#">Edit</a>	<a href="#">Edit</a>	<a href="#">Edit</a>	
	EXC2	<a href="#">Edit</a>	<a href="#">Edit</a>	<a href="#">Edit</a>	
	EXC3	<a href="#">Edit</a>	<a href="#">Edit</a>	<a href="#">Edit</a>	
	EXC4	<a href="#">Edit</a>	<a href="#">Edit</a>	<a href="#">Edit</a>	
	EXC5	<a href="#">Edit</a>	<a href="#">Edit</a>	<a href="#">Edit</a>	
	EXC6	<a href="#">Edit</a>	<a href="#">Edit</a>	<a href="#">Edit</a>	
	EXC7	<a href="#">Edit</a>	<a href="#">Edit</a>	<a href="#">Edit</a>	
	EXC8	<a href="#">Edit</a>	<a href="#">Edit</a>	<a href="#">Edit</a>	
	EXC9	<a href="#">Edit</a>	<a href="#">Edit</a>	<a href="#">Edit</a>	
	EXC10	<a href="#">Edit</a>	<a href="#">Edit</a>	<a href="#">Edit</a>	
	EXC11	<a href="#">Edit</a>	<a href="#">Edit</a>	<a href="#">Edit</a>	



Figure 81 Materials tab in the Irazu User Interface.

### Editing ‘Elastic Properties’

To edit the *Elastic Properties* for the material, click on **Edit** under *Elastic Properties* on the Materials tab. In the resulting *Edit Material* window, enter the input parameters, as shown in [Figure 82](#), and click **OK**.





**Material Editor**

Name:   


Material Model:

**Elastic Properties** | Strength Properties | Penalties

Density:  kg/m<sup>3</sup> 

Damping: Viscous: Factor  

Constitutive Law:

Young's Modulus:  Pa 


Poisson's Ratio:  

Figure 82 Elastic properties.



## Editing 'Strength Properties'

To edit the *Strength Properties* for the 'Rock' material, click **Edit** under *Strength Properties* on the Materials tab. In addition, click the Get Estimate button to estimate the Model I and Model II fracture energy values, as shown in Figure 83.

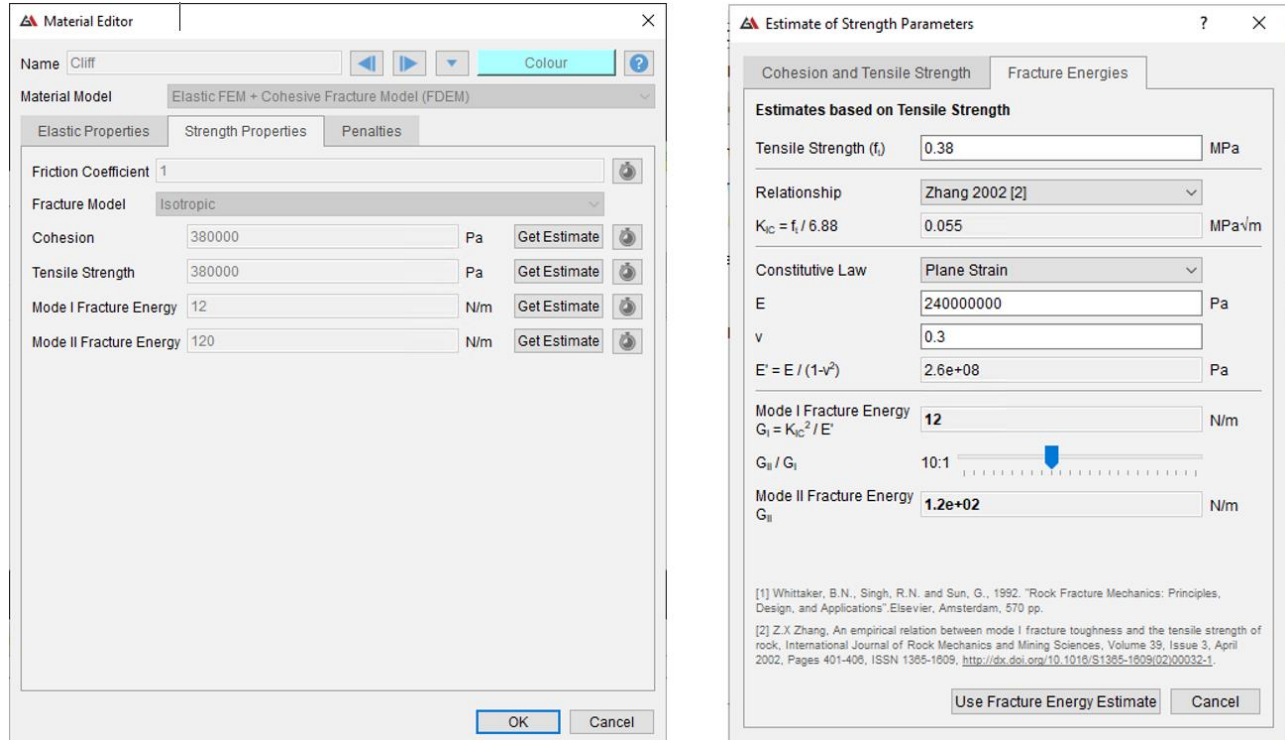


Figure 83 Setting strength properties: (a) Strength properties (b) Estimate of Strength Parameters.


This model applies a strength reduction approach by gradually reducing the initial strength values assigned to the rock over time. The progressive strength reduction is performed by setting a time variation of the Cohesion, Tensile Strength, Mode I Fracture Energy, and Mode II Fracture Energy. The strength properties are reduced by a factor  $F$  which increases over time and represents a measure of the slope's safety factor. Initial parameters are assumed to be associated with  $F = 1$ . The following relationships are adopted:

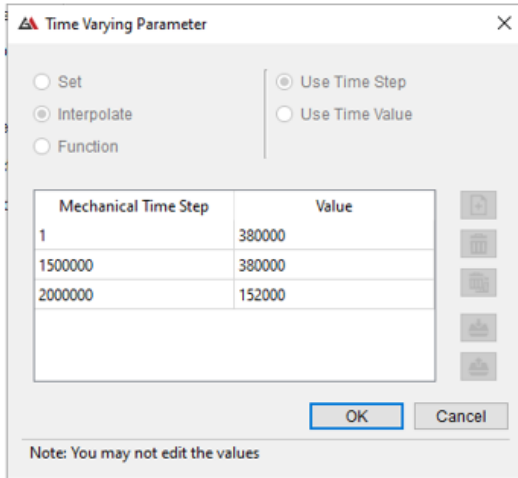
$$c^{new} = \frac{c^{old}}{F}$$

$$f_t^{new} = \frac{f_t^{old}}{F}$$

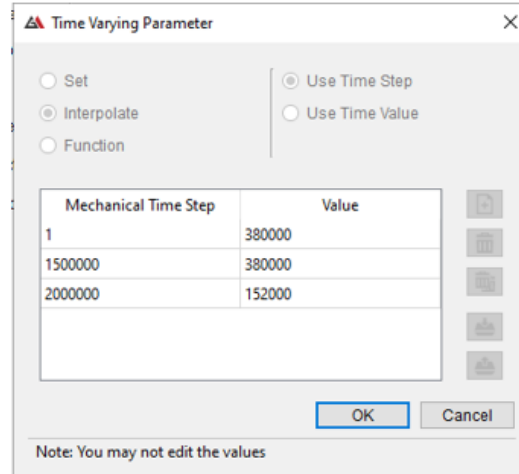
$$G_{Ic}^{new} = \frac{G_{Ic}^{old}}{F}$$

$$G_{IIc}^{new} = \frac{G_{IIc}^{old}}{F}$$

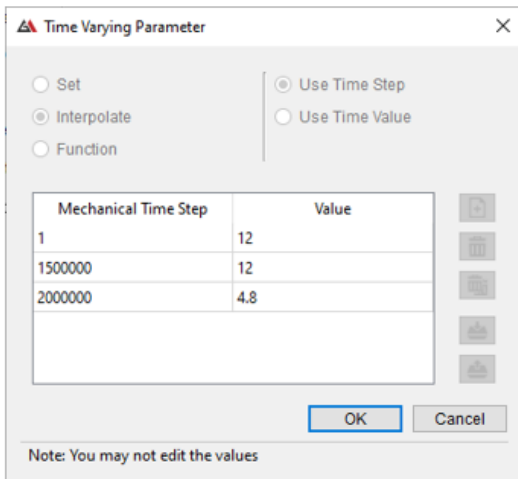
The time variation of each parameter is using the linear interpolation function of Irazu. In this case, each strength parameter is linearly reduced from the initial value at time step = 1,100,000 to 1/2.5 (F = 2.5) of the initial value at time step = 1,700,000. In general, the strength reduction sequence should start only after the model has reached equilibrium under the effect of the in-situ stresses. To specify a time-varying strength parameter value for the slope model, click the Time button (  ) beside each parameter and enter the settings shown in [Figure 84](#).



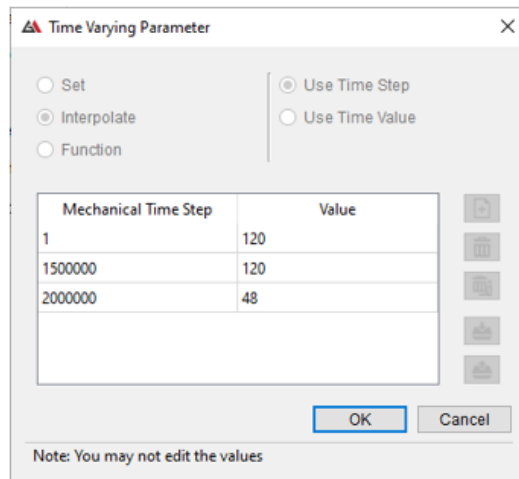
(a) Time variation of cohesion



(b) Time variation of tensile strength



(c) Time variation of Model I fracture energy



(d) Time variation of Model II fracture energy

Figure 84 Setting the time variation of the strength parameters.

### Editing and assigning 'Advanced Properties'

Advanced properties control material excavation, interface behavior between different materials, and stress reset options. In the cliff excavation model, the interface between the excavation and the cliff used the same strength properties and penalties. Complete the excavation part by clicking Enable in the relevant drop-down menu and specifying a mining time of 20,000 simulation time steps ([Figure 85](#)).

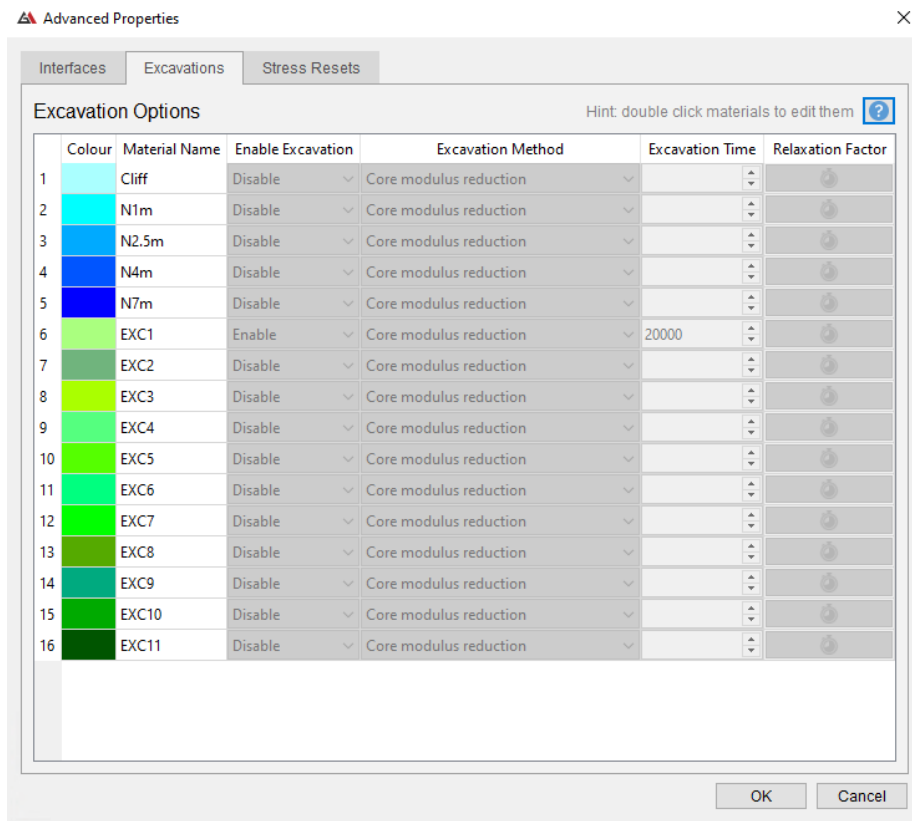


Figure 85 Setting the Advanced Properties.

### Assigning 'Materials'

Select all the elements comprising the model and assign the material 'Rock' to them. To reflect this assignment, the elements of the rock mass will inherit the color defined for this material on the *Materials* tab. When complete, the graphical display should look like [Figure 86](#).

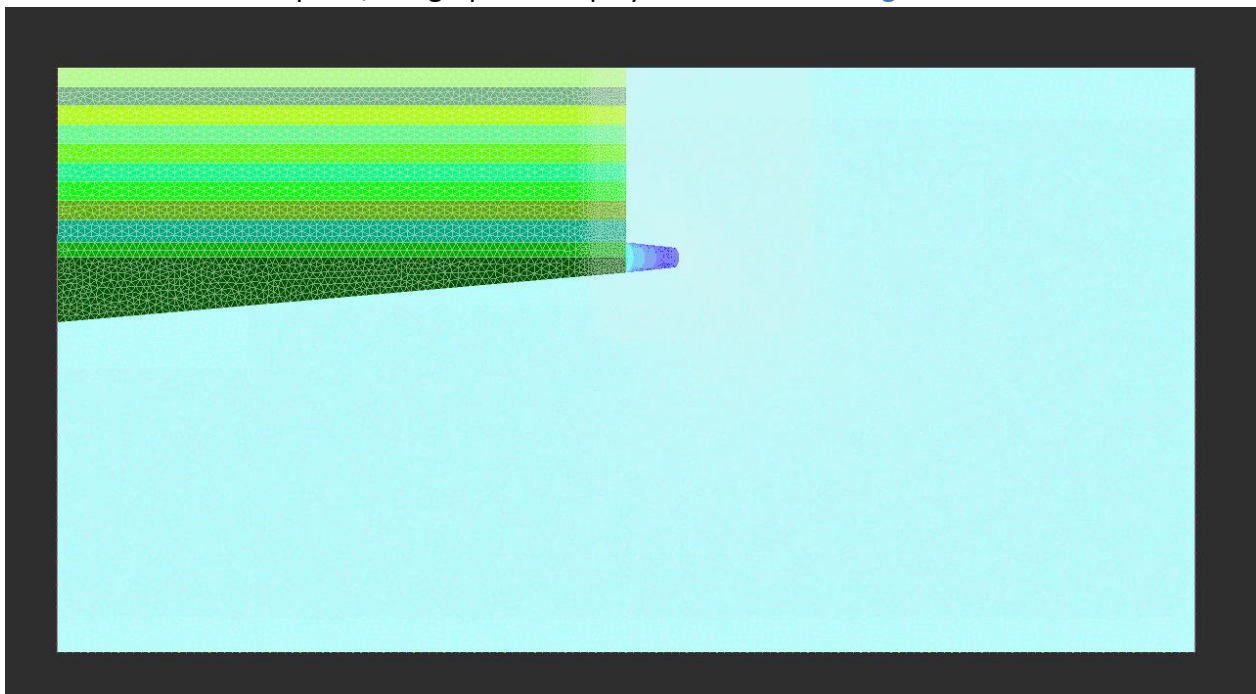



Figure 86 Completed Materials assignment for the rock cliff model.

## • Specifying and Assigning Boundary Conditions

For the slope model, three boundary conditions need to be assigned to the nodes of the mesh. That is, the bottom boundary of the model will be assigned a zero-velocity condition in the y-direction, but two extreme corners of the bottom boundary will be assigned a zero-displacement, while the lateral boundaries will be assigned a y-direction roller. On the *Boundary Conditions* tab of the *Irazu User Interface*, a boundary condition can be created by clicking on the Plus button (  ). The details of the boundary condition will appear in the table and can be edited. The settings to achieve the desired boundary conditions for the cliff model are illustrated in the screen capture shown in [Figure 87](#).

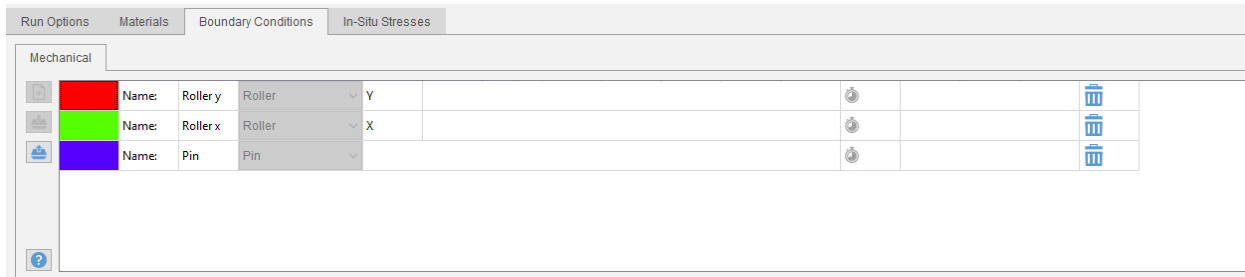


Figure 87 Definition of Boundary Conditions in the Irazu User Interface.

Select the nodes located on the lateral boundaries of the model and assign the 'Roller y' boundary condition to them. Similarly, select the nodes located on the bottom boundary of the model and assign the 'Roller x' boundary condition to them. In addition, two extreme nodes of the bottom boundary assign the 'Pin' boundary condition to them.

To reflect this assignment, the nodes of the lateral and bottom boundaries will inherit the colors defined for these boundary conditions on the *Boundary Conditions* tab. When complete, the graphical display should look like [Figure 88](#).

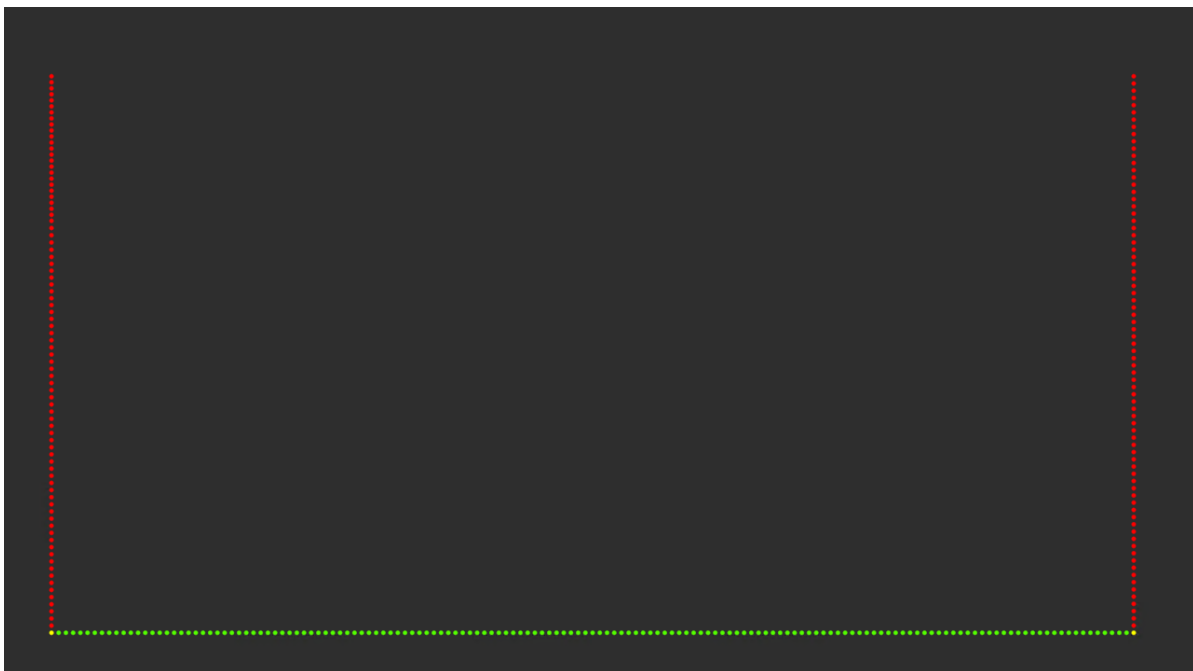


Figure 88 Complete assignment of Boundary Condition for the cliff model.

- **Specifying ‘In-Situ Stresses’**

Since the initialization of the model with the prescribed stress field is performed via explicit integration of the equations of motion for the discretized system, the total number of time steps for this initialization stage needs to be specified as well. Also, enables the absorbing boundary condition option to speed up the convergence of the model to the prescribed stress state. At the end of this initialization stage, each finite element in the model will be subjected to a vertical stress equal to the lithostatic stress computed based on a topographic surface located at  $y = 77$  m, density equal to  $2100 \text{ kg/m}^3$ , and gravitational acceleration equal to  $-9.81 \text{ m/s}^2$ . A stress ratio  $K_0 = \sigma_h / \sigma_v = 1$  is assumed in the specification of the horizontal stress gradient, as shown in [Figure 89](#).

Run Options	Materials	Boundary Conditions	In-Situ Stresses
Termination Criterion		Fixed Number of Time Steps	<input type="checkbox"/> Use Actual Ground Surface
Number of Time Steps		2500000	<input checked="" type="checkbox"/> Enable Absorbing Boundary Conditions
Input Options		X, Y System of Reference	<input type="checkbox"/> Enable Material-based Definition of In-Situ Stresses
Type		Linearly Varying Along Y	Reference Elevation (Y) 77 m
$\sigma_{XX}$		0 Pa	$\Delta\sigma_{XX}/\Delta Y$ : -20601 Pa/m
$\sigma_{YY}$		0 Pa	$\Delta\sigma_{YY}/\Delta Y$ : -20601 Pa/m
$\sigma_{XY}$		0 Pa	$\Delta\sigma_{XY}/\Delta Y$ : 0 Pa/m

Figure 89 Definition of In-situ Stresses in the Irazu User Interface.

### 9.4.1.3 Adding some runnings accounting for liner installation

To create some subsequent runs, click on the Plus button at the end of the run tabs or right-click on Run 1 and select ‘Copy Run’ ([Figure 90](#)).

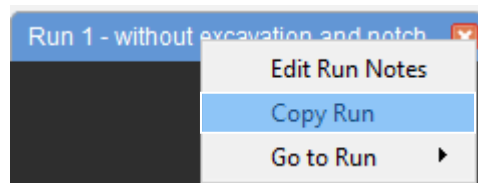


Figure 90 Creating a copy of a Run

Most of the input parameters are identical to those described above for Run 1, except those described below.

- **‘Advanced Properties’**

In some subsequent runs, for the EXC part, the core replacement method is excavated every 20,000-time steps. Afterward, the core replacement method is excavated every 250,000 time steps for the Notch part.

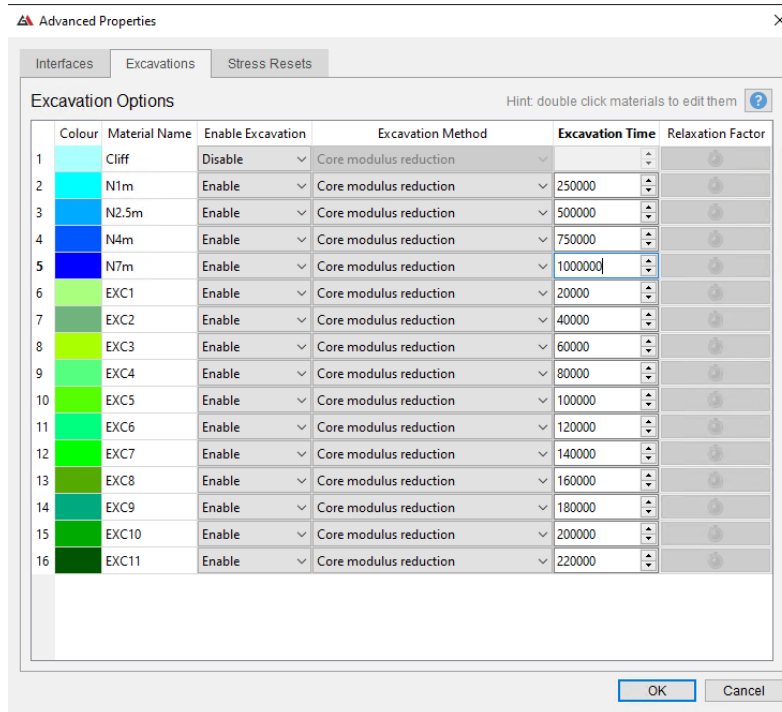


Figure 91 Setting the excavation for subsequent Run.

## 9.4.2 Homogeneous cliff with joint

### 9.4.2.1 Geometry and mesh generation

Follow the steps above to set up the cliff model geometry. In addition, in the *DFN generator* window, set the joint geometry as shown in Figure 92.

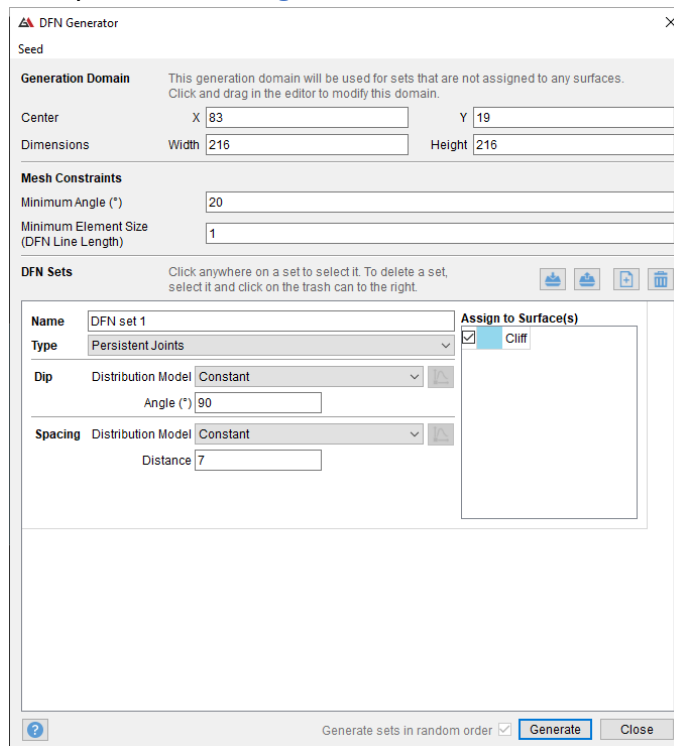


Figure 92 Setting the DFN Generator.

It is necessary to delete the redundant joints, and then modify the coordinates of the two ends of the remaining joint to (82, 77) and (82 58.25). (Figure 93, Figure 94)

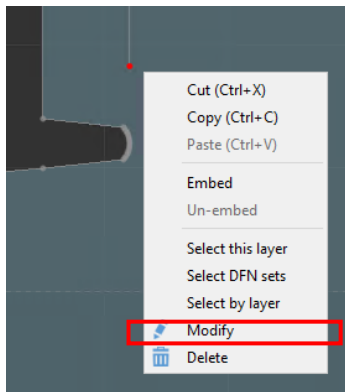
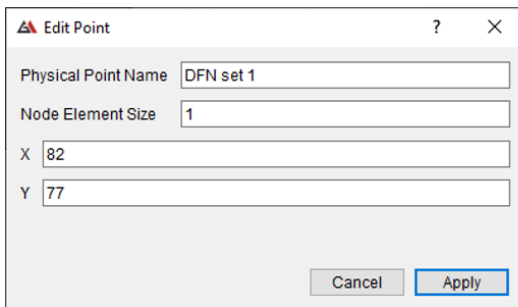
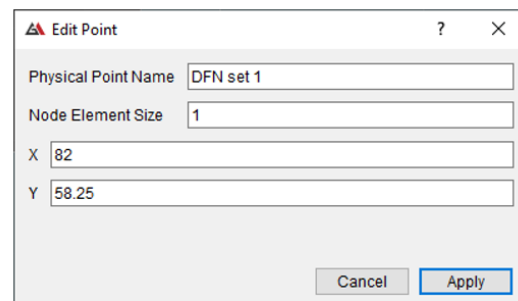


Figure 93 Modifying the properties.



(a) Coordinate the upper node joint



(b) Coordinate the lower node joint

Figure 94 Coordinate the extreme nodes joint.

The final result is shown in Figure 95.

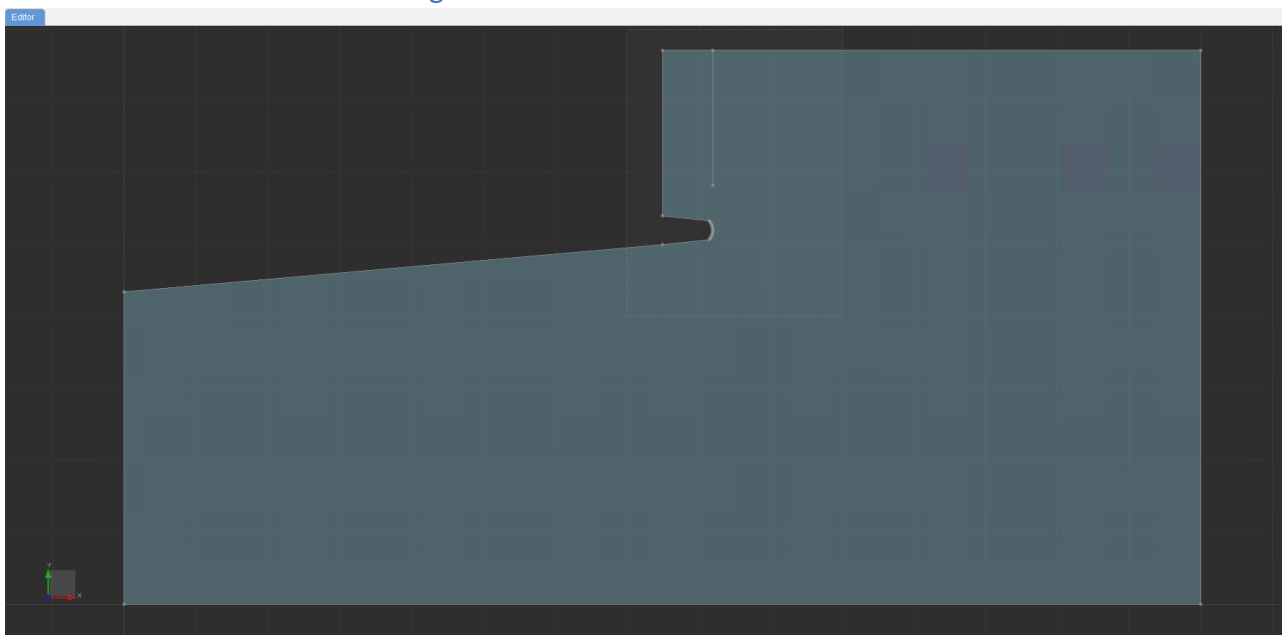


Figure 95 Final geometry of the cliff model.

## 9.4.2.2 Model construction with the Irazu User Interface

- **Using mesh for the project.**

Follow the steps above to set up the *Project Options* window, but don't forget to check 'Enable Discrete Fracture Network'. (Figure 96)

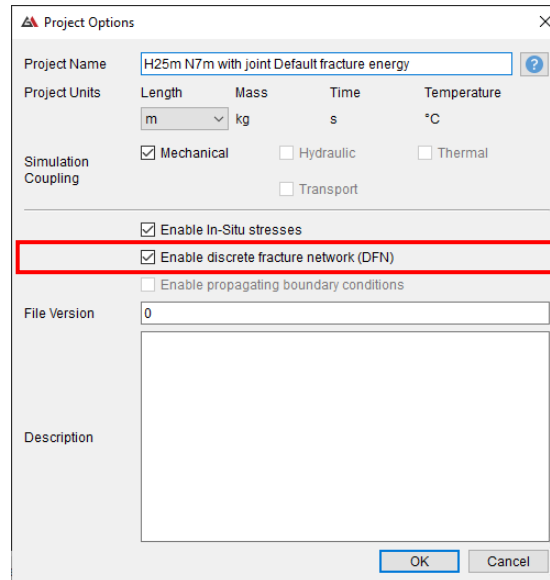


Figure 96 Specification of Project Options.

- **Specifying 'Run Options'**

For this simulation, on the *Run Options* tab of the *Irazu User Interface*, the *Number of Time Steps* will be 300,000, the *Time Step Size* will be 8.2e-6 seconds and the *Output Frequency* will be 1000-time steps. *Gravity acceleration* is assumed equal to -9.81 m/s<sup>2</sup>. Enable the *FEM Run* option to allow the computation of the elastic stress field in the rock mass based on the previously defined in-situ stresses and the actual slope geometry. The Run Options tab with the above values specified is provided in Figure 97.

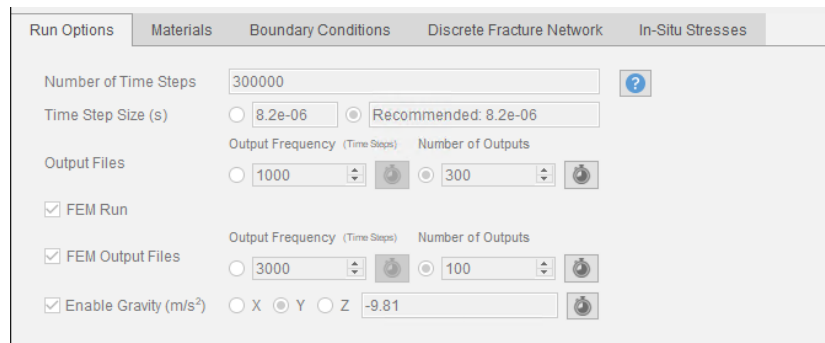



Figure 97 Setting run options in the Irazu User Interface.

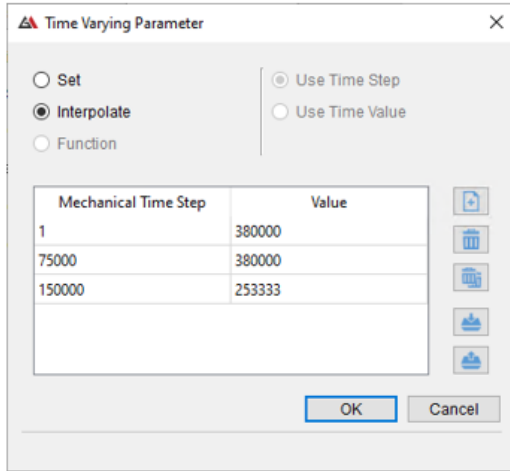
- **Specifying and assigning properties for 'Materials'.**

The process and data of adding *Materials* and defining the *Elastic properties* and *Strength properties* of the materials are the same as in the [above](#) chapter.

But when simulating the shear strength reduction method, some of the data specified are different from the [above](#) chapter. In this case, each strength parameter is linearly reduced from the initial value at time step = 75,000 to 1/1.12 ( $F = 1.5$ ) of the initial value at time step = 150,000. In

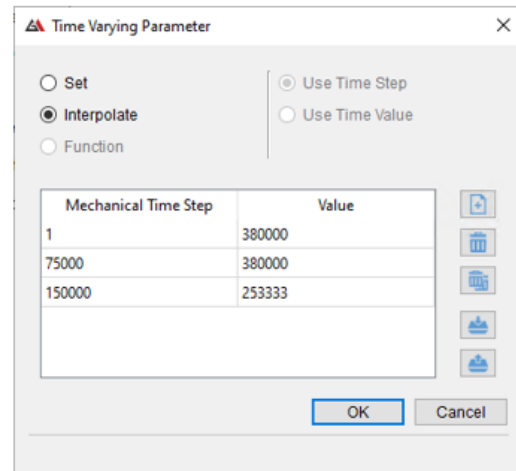


general, the strength reduction sequence should start only after the model has reached equilibrium under the effect of the in-situ stresses. To specify a time-varying strength parameter value for the slope model, click the Time button (  ) beside each parameter and enter the settings shown in Figure 98.



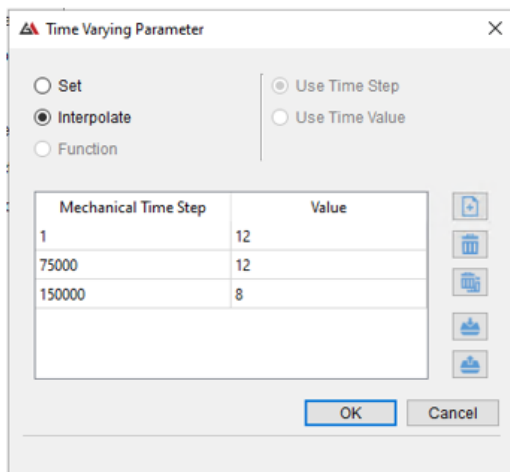
Mechanical Time Step	Value
1	380000
75000	380000
150000	253333

(a) Time variation of cohesion



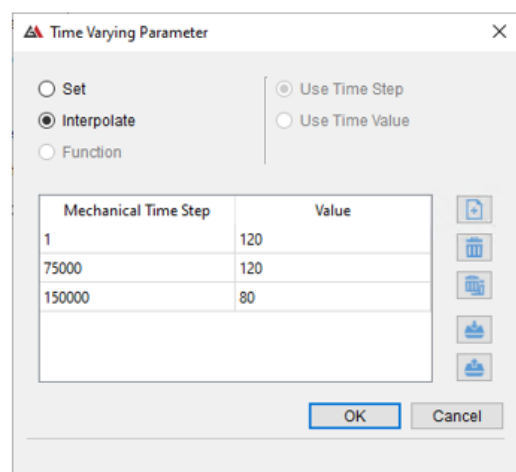
Mechanical Time Step	Value
1	380000
75000	380000
150000	253333

(b) Time variation of tensile strength



Mechanical Time Step	Value
1	12
75000	12
150000	8

(c) Time variation of Model I fracture energy



Mechanical Time Step	Value
1	120
75000	120
150000	80

(d) Time variation of Model II fracture energy

Figure 98 Setting the time variation of the strength parameters.

- **Specifying and Assigning Boundary Conditions.**

The process steps and data setup are the same as in the [above](#) chapter.

- **Specifying 'In-Situ Stresses'.**

In the *Irazu User Interface*, the total number of time steps is specified as 300,000, the other factors are the same as in the [above](#) chapter. (Figure 99)

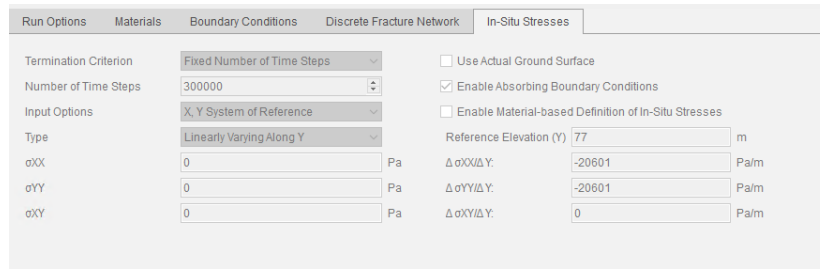


Figure 99 Definition of In-situ stresses in the Irazu User Interface.

- **Specifying and Assigning ‘Discrete Fracture Network’.**

On the *Discrete Fracture Network* tab of the *Irazu User Interface* (Figure 100), a property set for the DFN can be created by clicking on the **Plus** button ( ). The details of the DFN property will appear in the table and can be edited. Choose Cohesive as the type.

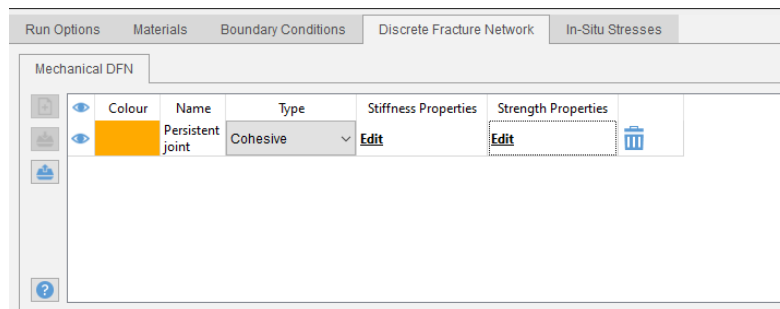
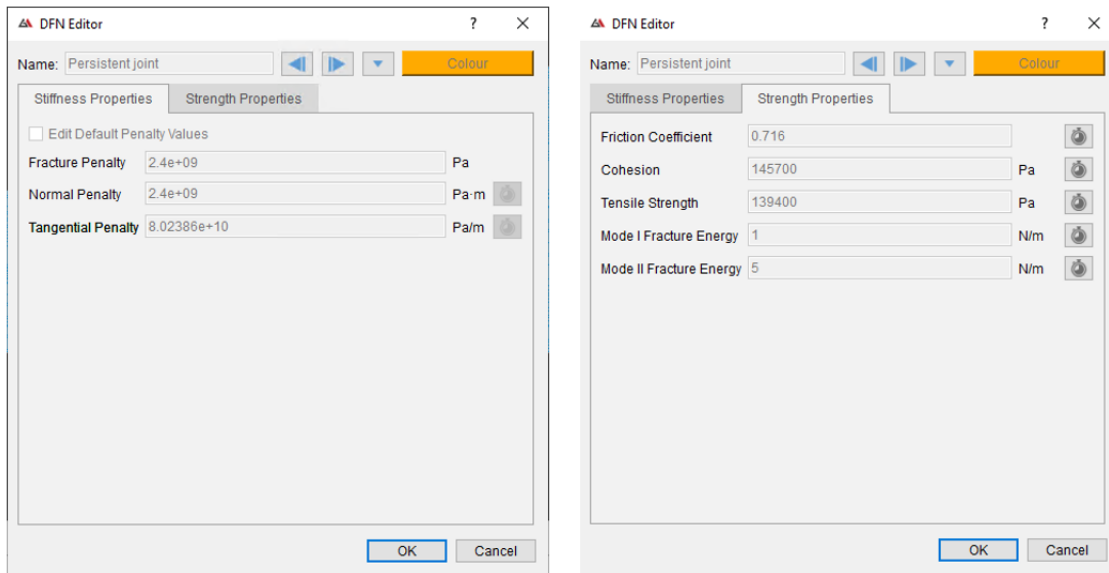


Figure 100 Definition of Discrete Fracture Network in Irazu User Interface.

To edit the *Stiffness Properties* and *Strength Properties* for the joint set, click on **Edit** under *Stiffness Properties* and *Strength Properties*, respectively, on the *Discrete Fracture Network* tab. In the resulting windows, enter the input parameters, as shown in Figure 101.



(a) Stiffness properties of Joint

(b) Strength properties of Joint

Figure 101 Setting the Discrete Fracture Network properties.

Right-click on the graphical display and choose Joints from the list of available entities. These nodes will now be highlighted in the graphical display. By right-clicking once more, one can assign the previously defined Joint Set properties to the selected nodes. To reflect this assignment, the nodes will inherit the color defined for this property on the *Discrete Fracture Network* tab. When complete, the graphical display should look like [Figure 102](#).

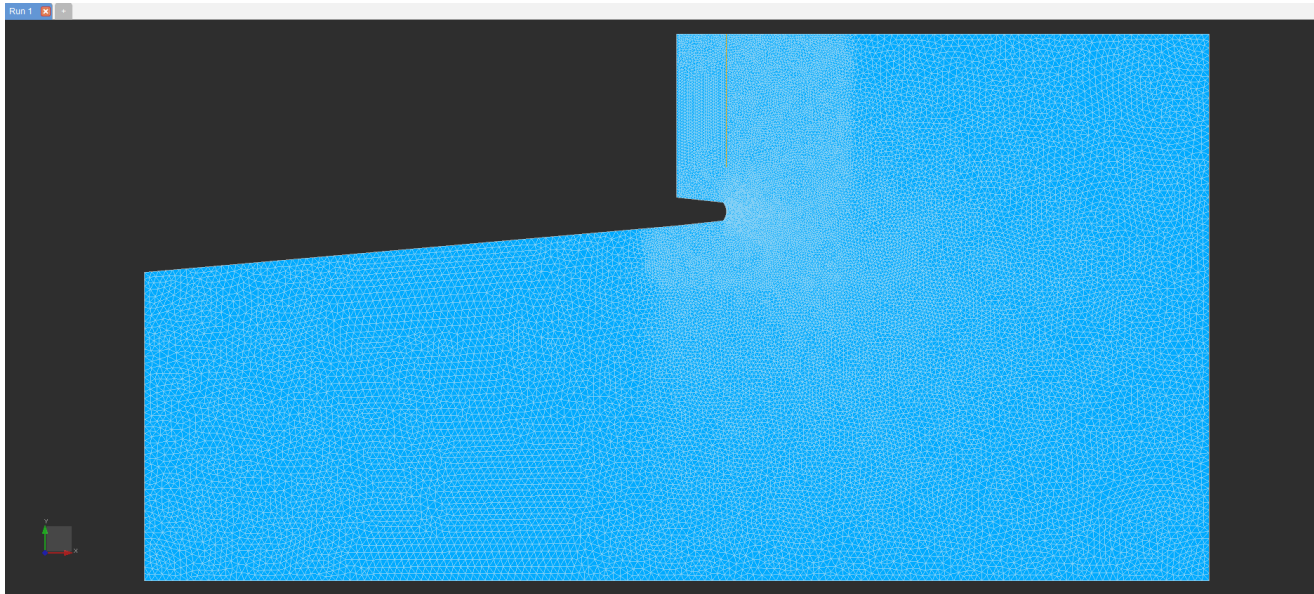


Figure 102 Completed Discrete Fracture Network assignment for the model.